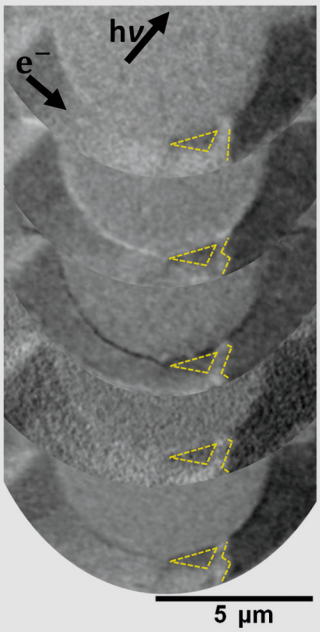

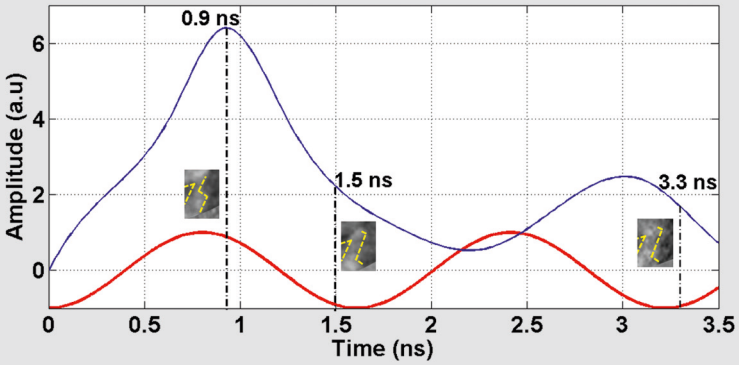

Current-Induced Magnetization Dynamics in Ferromagnetic Nanowires

Muhammad Imtiaz Khan

Schlüsseltechnologien / Key Technologies
Band / Volume 166
ISBN 978-3-95806-308-2

Mitglied der Helmholtz-Gemeinschaft

JÜLICH
Forschungszentrum

Schriften des Forschungszentrums Jülich
Reihe Schlüsseltechnologien / Key Technologies Band / Volume 166

Forschungszentrum Jülich GmbH
Peter Grünberg Institut (PGI)
Elektronische Eigenschaften (PGI-6)

Current-Induced Magnetization Dynamics in Ferromagnetic Nanowires

Muhammad Imtiaz Khan

Schriften des Forschungszentrums Jülich
Reihe Schlüsseltechnologien / Key Technologies Band / Volume 166

ISSN 1866-1807 ISBN 978-3-95806-308-2

Bibliografische Information der Deutschen Nationalbibliothek.
Die Deutsche Nationalbibliothek verzeichnet diese Publikation in der
Deutschen Nationalbibliografie; detaillierte Bibliografische Daten
sind im Internet über http://dnb.d-nb.de abrufbar.

Herausgeber und Vertrieb:	Forschungszentrum Jülich GmbH Zentralbibliothek, Verlag 52425 Jülich Tel.: +49 2461 61-5368 Fax: +49 2461 61-6103 zb-publikation@fz-juelich.de www.fz-juelich.de/zb
Umschlaggestaltung:	Grafische Medien, Forschungszentrum Jülich GmbH
Druck:	Grafische Medien, Forschungszentrum Jülich GmbH
Copyright:	Forschungszentrum Jülich 2018

Schriften des Forschungszentrums Jülich
Reihe Schlüsseltechnologien / Key Technologies, Band / Volume 166

D 464 (Diss., Duisburg, Univ., 2017)

ISSN 1866-1807
ISBN 978-3-95806-308-2

Vollständig frei verfügbar über das Publikationsportal des Forschungszentrums Jülich (JuSER)
unter www.fz-juelich.de/zb/openaccess.

Abstract

This thesis deals with the magnetization dynamics in nanostructures of NiFe alloys ($Ni_{80}Fe_{20}$ and $Ni_{20}Fe_{80}$) induced by an electric current via the spin transfer torque effect (STT). Single-pulse and time-resolved experiments have been carried out, imaging the magnetic domains in a photoemission electron microscope (PEEM), using the circular polarized synchrotron radiation of BESSY-II.
In single-pulse experiments, the reaction of magnetic domains and domain walls (DWs) upon individual current pulses in the nanostructures are studied and the approximate threshold current density for the DW motion was determined to about 7.5×10^{11} A/m^2. We designed three different types of nanostructures, favorable for different types of DWs: a V-shape, a half ring-shape and a notched half ring- shape.
Besides the influence of the current pulses on domain textures, we observed that high current pulses created new multiple domain configurations, like diamond patterns and domain arrays. For those, rather than nucleation due to STT, a temperature rise seems to be the dominant mechanism. We also observed the conversion from a vortex-like flux closure domain into a transverse wall (TW).
In order to enable time-resolved studies of the DW motion in pump-probe experiments with sufficient intensity, several modifications for a time-resolving mode had to be integrated into our energy filtered aberration-corrected PEEM: (1) A new modified sample holder for shorter current pulses ($\sim$ 1 ns). (2) A negative deflection-gating concept to increase the intensity while discriminating the signal from all the multi-bunches (MBs) with no adjacent pump pulse. Finally, we performed a pump-probe experiment and have observed the dynamics of small reversible DW boundary changes on a ns timescale for the first time in a truly current-induced pump-probe experiment.

Zusammenfassung

Die Bewegung von magnetischen Domänen unter dem Einfluß eines Stromes und des dadurch verursachten "Spin Transfer Torque" (STT) wurde in Nanodrähten aus $Ni_{80}Fe_{20}$ und $Ni_{20}Fe_{80}$ untersucht. Sowohl die Verschiebung nach einzelnen Strom-Pulsen als auch das dynamische Verhalten während eines Pulses und bis zu einigen ns danach ("pump probe") wurden in einem Photoemissionsmikroskop (PEEM) bei BESSY-II sichtbar gemacht. In den Einzelpuls-Experimenten wurde die Reaktion der Domänen auf individuelle Strom-Pulse untersucht. Der beobachtete Strom-Schwellwert, ab der eine Bewegung erfolgt, lag bei $\sim 7.5 \times 10^{11}$ A/m^2. Nanodrähte in V-Form, Halb-Ring und Halb-Ring mit Kerbe wurden entwickelt, optimiert für verschiedene Arten von Domänen. Neben der Verschiebung der Domänen wurde zusätzlich bei sehr hoher Stromdichte die Entstehung neuer Vielfach-Domänen beobachtet, z.B. als Diamant-Muster. Die Hauptursache hierfür scheint, eher als der STT, die erhöhte Temperatur zu sein. Dem Temperatur-Anstieg, der mit Strom-Pulsen verbunden ist, wird hier im Gegensatz zu früheren Studien erhöhte Bedeutung zugeordnet. Eine weitere Beobachtung war die Umwandlung einer wirbelartigen "flux-closure"-Domänen-Struktur in eine transversale Domänenwand. Für die zeitaufgelösten "pump probe"-Messungen waren mehrere Modifikationen an dem PEEM notwendig: (1) Ein veränderter Probenhalter, der das Einbringen von schnellen, kurzen Strompulsen (1 ns und kürzer) ermöglicht, obwohl die Probe auf HV liegt. (2) Ein "Gating", bei dem nur das Signal einzelner Röntgen Pulse benutzt wird und die für Zeit-Studien untauglichen Multi-Bunche unterdrückt werden. Die so vorgenommenen "pump probe"-Experimente zeigten erste, zum ersten Mal wirklich Strom-induzierte, wenn auch kleine, reversible Domänenwand-Verschiebungen auf einer Zeitskala von bis unter 1 ns.

Contents

Chapter 1

Introduction

Spintronics refers to the scientific research field where the electron's spin is envisaged to be manipulated for attaining nonvolatile memories, logic devices, and sensors. In 1851, Lord Kelvin discovered the first interdependence of magnetic and electrical properties of a material by changing the electrical resistance of Fe via a magnetic field, known as anisotropic magnetoresistance (AMR) [28]. In 1988, the discovery of giant magnetoresistance (GMR) was an important breakthrough in this field [50]. The GMR is the substantial change of resistance under a magnetic field in magnetic multilayers which are separated by non-magnetic layers. The GMR effect has enabled an improvement in the data storage capacity of hard disk drives (HDD) within the subsequent 10 years [50, 100]. The GMR effect was separately and simultaneously discovered by A. Fert [5] and P. Grünberg [11], for which they were awarded Nobel Prize in 2007. Already in 1975, the tunneling magnetoresistance (TMR) in Fe/GeO/Co junctions had been discovered by M. Julliere [60], but it did not attract much attention at that time due to only 14 % of relative change of resistance at cryogenic temperature. Very recently, Ikeda et al. [54] realized effects up to 604 % in CoFeB/MgO/CoFeB pseudo-spin-valves at room temperature [50, 92].

The idea behind using the spin as a state variable in spintronic devices is that the information storage can be made non-volatile [8] and hence does not need energy to be pertained. The concept of non-volatile magnetoresistive random access memory (MRAM) was proposed in 1990. Different from dynamic

random access memory (DRAM) in which electrical charges are used for storing data bits, MRAM uses magnetic storage elements for this purpose. This avoids the need of refreshing the charge in DRAM's every 20-50 ms, which deposits a lot of energy in the device and hence also limits the storage density. A magnetic storage element typically is a pair of ferromagnetic metal layers separated by a thin insulating layer, known as magnetic tunnel junction (MTJ). In an earlier MRAM generation, the electrical current was used to produce a magnetic field in the MTJ to read or write a memory cell [109]. For this approach, a considerable power was needed to switch between the states. Also, downscaling the unit size of a memory cell is limited in this approach. Here the spin-transfer torque based magnetic random access memory device (STT-MRAM) can be a solution to these problems and can be used to store and read the information electrically with low power in non-volatile memories [126, 141]. In the STT technique, a current flows between two non-collinear magnetic textures to transfer spin momentum from one texture to another. The physical principle of the STT can be demonstrated in two ferromagnetic layers separated by an insulator (magnetic tunnel junction) or a non-magnetic layer (spin valve) and between non-collinear domains in a magnetic nanowire as well [34]. However, even a STT-MRAM requires a high current density for fast switching, which eventually decreases the life-time of the MTJ.

Very recently, a new spin-orbit torque (SOT) technique has been reported to demonstrate the magnetization switching induced by in-plane current injection in heavy metal/ferromagnetic heterostructures [32]. This torque is based on orbital-to-spin momentum transfer [36], where the angular momentum is transferred to the magnetization from the orbital part of the carrier wave function [19]. The spin-orbit torque was first detected in a single domain (Ga, Mn)As by Chernyshov et al. [21]. Recently, the spin-orbit torque based magnetic random access memory (SOT-MRAM) has drawn great attention as it eliminates some flaws of STT-MRAM. For example, since the current is injected in the plane of a layer rather than pass through the tunnel barrier, this technique does not damage the MTJ even by injecting high current density [19]. Different from the STT-MRAM, the read and write paths are decoupled in the SOT-MRAM, which

improves the performance at high speeds [19, 98].

Besides magnetic memories, programmable spintronics logic devices have attracted increasing interest as they show many potential advantages such as high operation speed, non-volatility, low power consumption and logic-in-memory structure [86]. MTJ-based circuits can be used as the main devices for logical computations [127]. In many security applications like banking cards, biometric authentication chips and subscriber identity module cards, the user inputs are usually stored in a recording device and injected into the logic circuit for comparing with a reference code [83].

In this thesis, we concentrate on the study of current-induced domain wall motion (CIDWM), where a current is passed through a nanostructure, containing domains and a domain wall in between and the latter is displaced by the STT. This CIDWM seems the most promising effect for attaining the goal of high-speed, high-density and low-power novel applications. The best example is a racetrack memory the concept of which was presented by Stuart Parkin in 2004 [101]. This system stores digital data using many magnetic domains arranged consecutively in a nanowire. The $Ni_{80}Fe_{20}$ nanowires used in the presently proposed racetrack memory, in which the STT exerted by the spin-polarized current moves the domain pattern across a read head so that information can be retrieved. This racetrack concept requires a relatively high current density to displace the domain walls. But high current density also generates a higher Oersted field in the structure, which affects the domain wall motion and also changes the domains pattern within the structure, increases local heating and overall causes higher power consumption [44, 55]. Hence, for successful applications, further optimization of these data storage systems is needed. For example, a small critical current density would be preferably needed to move the domain patterns, in order to avoid generating thermal effects in a magnetic system. Second, a reliable domain wall motion has to be assured. Next, it is important to control the pinning of domain walls in the system and one has to ensure the maximum domain wall speed in the system [138]. To further study and optimize CIDWM devices, thin in-plane magnetized soft material nanostruc-

tures can be fabricated as it can be expected from these thin systems that they will reduce the effect of the Oersted field on the domain wall textures down to a minimum.

Before the availability of magnetic circular dichroism-photoemission electron microscopy (XMCD-PEEM) as a magnetic imaging technique, besides electrical transport measurements [71], magneto-optical Kerr effect (MOKE) measurements [99] have been used to visualize the domain wall motion. However, MOKE does not provide element specific contrast and has a lower spatial resolution ($\geq$ 300 nm), due to the diffraction limit with visible light. Hence it is very difficult to do magnetic imaging in the submicrometer regime [20]. In the soft x-ray regime, transmission x-ray microscopy (TXM) can be utilized to get element specific contrast and high sensitivity to the entire thickness of the sample. Moreover, it offers the spatial resolution with a current state of the art of 15 nm [61]. However, a big drawback of the TXM is that a sample needs to be grown on special membranes, through which the soft x-ray beam easily passes. These membranes are fragile and may hamper samples from different processing like epitaxial growth and variable measurement temperature etc. Hence, in this work, for the imaging of textures in single-pulse and time-resolved experiments, an aberration-corrected photoemission electron microscope (PEEM) was used, taking full advantage of the spatial resolution, the element specificity of XMCD and its sensitivity to in-plane magnetization.

While performing the single-pulse experiments, the objective of this work was to elucidate several basic aspects for understanding the CIDWM. First, to study the reaction of magnetic domains and domain walls upon individual current pulses in the nanostructures, we have designed three different types of $\mathrm{Ni_{20}Fe_{80}}$ nanostructures, favorable for different types of domain walls: a V-shape, a half ring-shape and a notched half ring- shape. We have chosen a $\mathrm{Ni_{20}Fe_{80}}$ V-shape nanostructure for studying the transverse wall motion, half ring-shape and geometrically notched half ring-shape nanostructures to study flux closure domain patterns. Second, we determined the approximate threshold current density for the domain wall motion of 7.5×10^{11} A/m^2. Next, we

estimated the maximum domain wall velocity up to 33 m/s by injecting 100 ns short current pulses. In these experiments, we have observed that the spin transfer torque-induced domain wall motion is significantly affected by a temperature increase.

The most challenging task of this thesis was to image the time evolution of the domain wall by the pump-probe technique. In such experiments, the synchronization between the excitation pulse (pump) and the x-ray pulse (probe) is used for imaging the time evolution of magnetization. By varying the time delay between pump and probe and recording billions of XMCD images of this cycle, the temporal evolution of the system after the excitation pulses can be mapped [20]. The current pulse can either be injected directly into the magnetic textures to study CIDWM or the Oersted field is induced by current pulses into a stripline, located below the magnetic textures. In the latter, an APD can be integrated at the back part of the sample holder and a laser-diode triggers the APD to generate short current pulses [96]. XMCD-PEEM combined with a coplanar waveguide imaging technique for short magnetic field pulses can be employed in a pump-probe mode for time-resolved measurement of domain wall motion.

As the excitation with a magentic field pulse for applications has disadvantages like limited down scaling, we study here the approach of current-induced domain wall motion, where current pulses are injected directly into a nanostructure. This experiment seems more challenging, as in previous studies, there were no clear successes: Uhlir et al. [138] have employed the XMCD-PEEM imaging technique to map the magnetization dynamics produced by nanosecond current pulses in $Ni_{80}Fe_{20}$/Cu/Co nanowires. They reported that the Oersted field generated by the current pulses produces a tilt of the $Ni_{80}Fe_{20}$ magnetization. In their trilayer system, they have recognized serious pinning origins. One of the most expected pinning sources is the dipolar interaction of the $Ni_{80}Fe_{20}$ layer with Co anisotropy inhomogeneities. To discover the full proficiency of the system, this pinning source should be controlled [138]. Heyne et al. [47] used the x-ray magnetic circular dichroism (XMCD) photo-emission elec-

tron microscopy (PEEM) to demonstrate the pump-probe imaging technique. They synchronized the gating of the channel plate to 25 μsec long current pulses and recorded XMCD images only when the current pulse is injected. They explored the reversible displacement of a vortex core in a 30 nm thick $Ni_{80}Fe_{20}$ disc with a diameter of 6 μm. [47]. Recently, Falk-Ulrich Stein et al. [124] have utilized time-resolved scanning transmission x-ray microscopy (STXM) to study structural transformations of domain walls motion in 8 μm long, 200 nm wide and 20 nm thick $Ni_{80}Fe_{20}$ nanowires with two perpendicular strip lines. Specifically, they have imaged the oscillations of the width of a domain wall and the wall transformation between vortex and transverse textures [124]. Despite their attempts, the study of the current induced domain wall motion in a ferromagnetic layer by utilizing the pump-probe mode still needs to be explored, as a data storage device, such as a racetrack memory, needs a controllable domain wall motion in both directions by inducing current pulses.

Concerning the pump-probe measurements, we developed a negative deflection gating, which suppresses the signal of all "unpumped" bunches in the multi-bunch (MB) mode of the synchrotron and thus makes pump-probe studies possible during the whole year instead of 2 single bunch (SB) weeks. For the first time, we succeeded in mapping the dynamic response of magnetic domain wall in a notched $Ni_{80}Fe_{20}$ half-ring shaped nanostructure by synchronizing laser-diode generated current pulses with synchrotron radiation pulses, though in these first experiments the observed movement was still small.

This Ph.D. thesis is organized as follows:

Chapter 2 starts with the basics of magnetism, theoretical and experimental backgrounds of the CIDWM that are required to understand the experimental results of this Ph.D. work.

Chapter 3 is devoted to the sample fabrication and the experimental methods used in this thesis. We present the XMCD-PEEM, the method of imaging magnetic structures using circularly polarized synchrotron radiation that is

used to study current induced domain wall motion via single current pulse and pump-probe experiments.

The technical development for XMCD-PEEM including the home-made current pulse-generator, modification of a sample-holder and layouts of the single-pulse and pump-probe experiments are presented in chapter 4. Specifically, this chapter presents the negative gating concept, employed in pump-probe studies in the SPECS aberration-corrected FE-LEEM-P90 instrument.

Chapter 5 presents the experimental results of single pulse experiments. Specifically, this chapter discusses the nucleation, propagation and splitting up of magnetic textures in $\mathrm{Ni_{20}Fe_{80}}$ nanostructures via single pulses.

Chapter 6 addresses the study of the magnetization dynamics in nanostructures via time-resolved magnetic imaging in an energy-filtered and aberration-corrected PEEM.

Chapter 7 summarizes this Ph.D. work and presents an outlook on challenges and future experiments.

Chapter 2

Theoretical and Experimental Background

In this chapter, first we discuss the Stoner model of ferromagnetism (see section 2.1). Next, an overview of basics and magnetic energy terms in micromagnetism which are relevant for this work is presented in section 2.2. We focus on the Landau-Lifshitz-Gilbert (LLG) equation of motion in section 2.3. A brief description on different possible domain textures in ferromagnetic nanostructures is presented in section 2.4. We present the theoretical and experimental background required for understanding the spin-transfer torque (STT) induced changes in the ferromagnetic nanostructures in section 2.5, which is followed by a discussion on significant temperature effects on the magnetic textures of a nanostructure by high current pulse (see section 2.6). The final section is devoted to the theory of different possible pinning effects in nanostructures (see section 2.7).

2.1 Stoner Model of Ferromagnetism

For the occurrence of ferromagnetic order in 3d transition metals like iron, nickel, and cobalt, Stoner has developed a criterion which will be discussed in the following paragraphs.

Based on a collective order of magnetic spins, the ferromagnets can be divided into two groups: localized and itinerant ferromagnets. The former is

represented by rare earth elements in which the ferromagnetic order can be understood by a model of localized magnetic moments [41]. This model does not work for calculating the magnetic moments and high Curie temperatures in itinerant ferromagnets like iron, nickel, and cobalt, due to the delocalized structure of the 3d electrons [63]. For this, we need an itinerant model having a magnetization due to spontaneously spin-split bands [12].

Ferromagnetism arises due to the exchange interaction that favors a parallel alignment of magnetic moments in the ferromagnetic materials. Because of the Pauli exclusion principle, two parallel electrons of same quantum numbers occupy different quantum states. Due to this parallel arrangement, the Coulomb repulsion of electrons is decreased and kinetic energy of the system is effectively increased [41].

In order to develop a model for band ferromagnetism, we take the density of states (DOS) of the free electron system, i.e. $D(E) = D^{\uparrow}(E) + D^{\downarrow}(E)$ and assume that some electrons from the spin-down side with energies from $E_F - \Delta E$ to E_F are redistributed into unoccupied spin-up states with energies from E_F up to $E_F + \Delta E$ [15] (see Fig. 2.1). In Fig. 2.1, $D(E_F)$ presents the density of states at Fermi level and ΔE shows the energy of the shifted electrons. The total number of shifted spin-down electrons is $D(E_F)\Delta E/2$, and the kinetic energy in the system is increased by:

$$\Delta E_{KE} = \frac{1}{2} D(E_F)(\Delta E)^2 \tag{2.1}$$

Owing to Pauli exclusion principle, when the kinetic energy of electrons increases, the Coulomb energy is decreased in the ferromagnetic case. Hence, one can write the change in potential energy ΔE_{PE} by the following expression:

$$\Delta E_{PE} = -\frac{1}{2} I D(E_F)^2 (\Delta E)^2 \tag{2.2}$$

where I is the Stoner parameter describing effective exchange interactions between electrons. Now the total change in energy can be written as:

$$\Delta E = \Delta E_{KE} + \Delta E_{PE} = \frac{1}{2} D(E_F)(\Delta E)^2 (1 - I D(E_F)) \tag{2.3}$$

This equation shows occurrence of ferromagnetism if $\Delta E < 0$ which implies that $ID(E_F) \geq 1$ i.e. the Stoner criterion. For all 3d metals, the Stoner exchange integral is of the same order, i.e. I = 1 eV. In such case, the density of states around the Fermi level plays the most important rule for fulfilling the Stoner criterion for ferromagnetism [116].

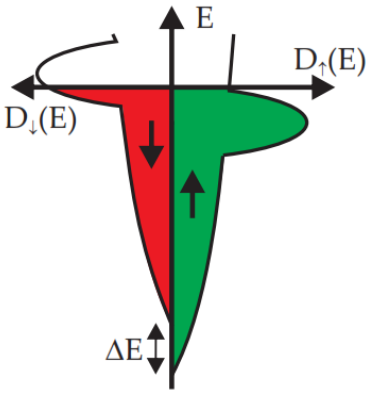

Figure 2.1: Sketch of density of states of a 3d metal with ΔE exchange splitting [63].

2.2 Basics and Magnetic Energy Terms in Micromagnetism

The magnetization **M** is a vector field that presents the total magnetic moments per unit volume in a magnetic system and these magnetic moments define the magnetic properties of a system. The magnetic moment relates to the spin and orbital moment contributions of the valence electrons in the solid. Depending on the collective interaction of magnetic moments, different materials can be distinguished. For example, in materials known as paramagnetic and diamagnetic, the interaction among magnetic moments is too weak. In materials such as ferromagnets, a strong exchange interaction among magnetic moments exists due to which there is a spontaneous long-range magnetic order below a critical temperature, resulting in a remanent magnetization, even in the absence of an

applied magnetic field [93]. The magnetic moments in ferromagnetic materials align themselves into regions of microscopic magnetic order called domains. The region between magnetic domains where the magnetization is not uniform is the magnetic domain wall (DW) [12].

Micromagnetism describes the magnetic system in the framework of a continuum theory. In general, the formation of micromagnetic structures is determined by the interplay of interactions on different length scales. These interactions make specific contributions to the total energy of the system. The formation of a particular micromagnetic structure is a result of the system trying to achieve the lowest energy state. There are different energy terms contributing to the formation of a magnetic structure. Those terms will be briefly explained in the next subsection 2.2.1.

2.2.1 Energies in Micromagnetism

In 1935, Landau and Lifshitz laid the physical foundation of micromagnetics by formulating the free energy equation [76, 142]. This equation contains different energy terms contributing to the formation of magnetic domains and domain walls. Here we briefly explain these energy terms:

Zeeman energy

This energy is due to the interaction between magnetic moments **M** of the material and the applied external magnetic field $\mathbf{H}_{\text{ext}}$. It is given by:

$$E_z = -\mu_0 \int_V \mathbf{M}\mathbf{H}_{\text{ext}} dV \tag{2.4}$$

It is proportional to the cosine of the angle between the local **M** vector and the applied external field $\mathbf{H}_{\text{ext}}$. This means that the Zeeman energy is reduced for the case where **M** is parallel to the $\mathbf{H}_{\text{ext}}$ and increased for the anti-parallel case [55, 78].

Exchange energy

This energy is due to the exchange interaction between the spins of two neighboring atoms, $\mathbf{S}_\mathrm{i}$ and $\mathbf{S}_\mathrm{j}$. In the Heisenberg picture, this interaction for a many particle system can be written as:

$$E_{\mathrm{ex}} = -\sum_{i \neq j} \mathbf{J}_{\mathrm{ij}} \mathbf{S}_\mathrm{i} \mathbf{S}_\mathrm{j} \tag{2.5}$$

where $\mathbf{J}_{\mathrm{ij}}$ is the exchange integral, depending on the distance between the spin neighbors $\mathbf{S}_\mathrm{i}$ and $\mathbf{S}_\mathrm{j}$. Depending on the ordering of the spins, **J** is either positive or negative. Positive **J** means that the spins are parallel, corresponding to ferromagnetic materials. A negative **J** shows that the spins are anti-parallel, favoring anti-ferromagnetic materials [12].

Magneto-crystalline anisotropy energy

Crystalline materials, in general, contain magnetically easy and hard axes. The magnetization is preferred to align along certain crystallographic directions. Magneto-crystalline energy arises from the orientation of magnetization with respect to the crystallographic axes of the material. The energy will be smaller when the magnetization is aligned to these crystal easy axes.

In the case of uni-axial anisotropy and a magnetization **M** which is at some angle θ away from the easy axis, the first term of the magneto-crystalline energy is given as [138]:

$$E_{\mathrm{anis}} = \int_V K_1 \sin^2\theta dV \tag{2.6}$$

where K_1 is first-order anisotropy constant, depending on the crystal symmetry and θ is the angle between the magnetization orientation and the easy axis.

Magneto-static energy/demagnetization energy/dipolar energy

This is a long-range interaction, in contrast to the anisotropy and exchange energy terms. This energy is resulting from the interaction between the mag-

netic dipoles in the material and it favors a magnetic closed flux. Mathematically, it can be written as:

$$E_{\mathrm{dip}} = -\frac{\mu_0}{2}\int_V \mathbf{H}_{\mathrm{d}}\mathbf{M}dV \tag{2.7}$$

where μ_0 is the permeability of vacuum. The $\mathbf{H}_{\mathrm{d}}$ is the demagnetizing field and is given by:

$$\mathbf{H}_{\mathrm{d}} = -\mathrm{N}\mathbf{M} \tag{2.8}$$

where magnetization $\mathbf{M}$ is opposed by the demagnetizing field $\mathbf{H}_{\mathrm{d}}$. The N is a demagnetizing tensor and it is shape-dependent. There is an additional energy term rising from the demagnetizing energy related with the shape of the system, called shape anisotropy. In the case of a thin film shape, an additional energy term comes up with the equation:

$$E_{\mathrm{shape}} = \frac{1}{2}\mu_0\mathbf{M}^2\cos^2\theta \tag{2.9}$$

where θ is the angle between the magnetization and the thin film normal [12]. According to this expression, the in-plane magnetization direction is energetically favorable due to the lower stray field compared to the out-of-plane magnetization in a thin film [48].

In short, demagnetization forces play the main role in the domain formation. The exchange and anisotropy are not enough to generate domain patterns. The anisotropy prefers crystallographic directions and exchange favors the parallel magnetization in any direction. These interactions alone would result in a monodomain structure, but in a high energy state. This high energy state will ultimately reduce by breaking up the magnetic monodomain structure into a multi-domain structure to decrease stray fields [64].

2.3 Magnetization Dynamics and Landau-Lifshitz-Gilbert Equation

The Landau-Lifshitz-Gilbert (LLG) equation describes the magnetization dynamics in a material. In 1935, Landau and Lifshitz proposed the basic equation

of motion for magnetization where the precessional term physically derived and the effect of relativistic interactions considered as a damping term [1]. In 1955, Gilbert modified their equation by reporting a damping term based on Lagrangian methodology [1, 3, 75]. This LLG equation will be discussed here.

According to Newton's law of motion, the rate of change of angular momentum **L** is equal to a torque **T** that is applied on a system. This can be written mathematically as:

$$\frac{d\mathbf{L}}{dt} = \mathbf{T} \tag{2.10}$$

This equation 2.10 helps to understand a free precession of the magnetization around an effective magnetic field by considering that: $\mathbf{T} = \mathbf{M} \times \mathbf{H}_{\text{eff}}$, where the torque **T** is due to an influence of the effective field on the magnetization. Further, quantum theory shows that the magnetization **M** is proportional to the angular momentum **L** of an atom by the following equation: $\mathbf{M}{=}{-}\gamma\mathbf{L}$, where the γ is the gyromagnetic ratio. Now the above equation of motion in terms of the magnetization **M** can be expressed as:

$$\frac{d\mathbf{M}}{dt} = -\gamma\mathbf{M}\times\mathbf{H}_{\text{eff}} \tag{2.11}$$

This is the Landau-Lifshitz equation of motion, showing that the torque **T** forces the magnetization **M** to precess around the effective field $\mathbf{H}_{\text{eff}}$ for an unlimited time with a constant angular velocity, $\omega = |\gamma\mathbf{H}_{\text{eff}}|$. The gyromagnetic ratio γ for ferromagnetic materials is 17.6 MHz/Oe [64]. This equation is schematically presented in Fig. 2.2a.

Landau and Lifshitz added an additional term to the equation, taking into account a damping of the precession towards the effective magnetic field [76]. The new form of the equation is written as:

$$\frac{d\mathbf{M}}{dt} = -\gamma\mathbf{M} \times \mathbf{H}_{\text{eff}} - \lambda\mathbf{M} \times (\mathbf{M} \times \mathbf{H}_{\text{eff}}) \tag{2.12}$$

where λ is the damping constant. The damping term on the most right side indicates that the precession will stop eventually. In 1955, Gilbert reported that

the Landau-Lifshitz damping term is only applicable in the case of small damping [38, 39]. Hence, he introduced a term for large damping cases [48, 65, 88] and modified the equation 2.12 as:

$$\frac{d\mathbf{M}}{dt} = -\gamma \mathbf{M} \times \mathbf{H}_{\text{eff}} + \frac{\alpha}{\mathbf{M}_{\text{s}}} \mathbf{M} \times \frac{d\mathbf{M}}{dt} \tag{2.13}$$

where α is the Gilbert constant and $\mathbf{M}_{\text{s}}$ shows the saturation magnetization. The damping effect is represented in Fig. 2.2b. The equation 2.12 and equation 2.13 conserve the norm of magnetization as both damping terms are perpendicular to magnetization $\mathbf{M}$ [48, 78].

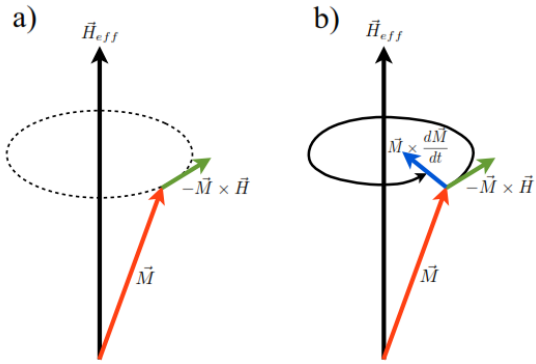

Figure 2.2: (a) Illustration of the Landau-Lifshitz equation without damping. $\mathbf{M}$ is precessing at a constant angular velocity around $\mathbf{H}_{\text{eff}}$ (dotted circle). (b) $\mathbf{M}$ is gyrating with the Gilbert damping term around $\mathbf{H}_{\text{eff}}$ on a spiral path [97].

2.4 Domains/Domain Wall Configurations

In the framework of this thesis, we study domain formation, propagation, and modification via a spin-polarized current in NiFe nanostructures. We deal with domains, having different spin patterns, like transverse walls, vortices, Landau patterns. Therefore, we first explain the spin configuration of the most common domains in nanostructures in the following paragraphs.

The free energy associated with the ferromagnetic system is described as:

$$E_{\text{free}} = E_{\text{z}} + E_{\text{anis}} + E_{\text{ex}} + E_{\text{dip}} \tag{2.14}$$

and with the energy terms explicitly written according to subsection 2.1:

$$E_{\text{free}} = \int_V K_1 \sin^2\theta dV - \mu_0 \int_V \mathbf{M}\mathbf{H}_{\text{ext}} dV - \sum_{i \neq j} \mathbf{J}_{ij}\mathbf{S}_i\mathbf{S}_j - \frac{\mu_0}{2}\int_V \mathbf{H}_{\text{d}}\mathbf{M} dV \tag{2.15}$$

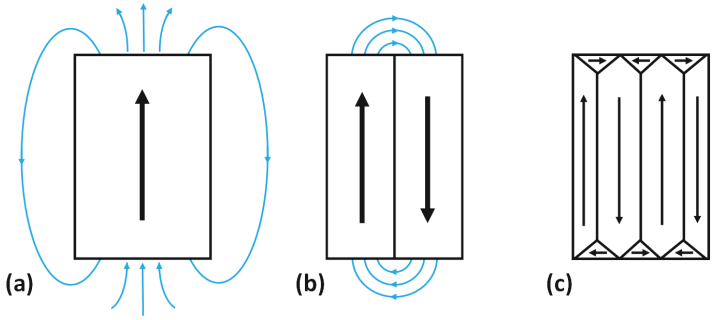

Figure 2.3: (a) Sketch of the uniformly magnetized ferromagnetic structure and the blue lines show the stray field. (b) Two anti-parallel aligned domains having a domain wall. (c) A flux closure pattern while eliminating the stray field.

It is necessary for the stability of the magnetic system that the free energy (2.15) is minimized. This equation favors a homogeneous alignment of magnetic moments in the system. The demagnetization energy has the main role in the splitting up of the mono-domain into multi-domains. The exchange interaction and the shape anisotropy favor the mono-domain structure but this structure has a large magnetic stray field near its edges, which eventually is increasing the demagnetization energy. Hence, the mono-domain structure will split up into multi-domains to minimize its energy [64]. There is a separation region between domains called domain wall, DW.

Fig. 2.3 presents three different domain patterns in the ferromagnetic structure. Fig. 2.3a shows a single homogeneous magnetized domain having a large

demagnetization energy. This energy is high, because of the magnetic charges on the edges of the structure. The structure needs to reduce this energy by simply distributing the single domain into two domains having different magnetization orientation with respect to each other (Fig. 2.3b). Further, the structure divides into multi-domains by minimizing its own energy. The whole structure appears in a single flux closure pattern by introducing domain walls [12].

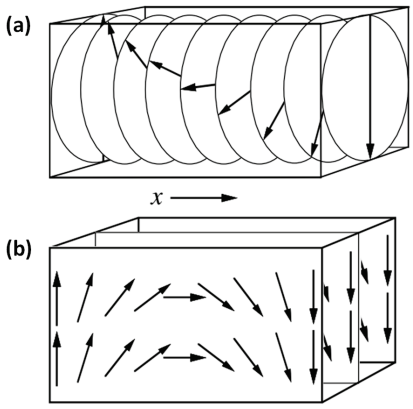

Figure 2.4: Schematic of Bloch wall (a) and Néel wall (b). Taken from [12]

We can define the domain walls based on the angle between the magnetization in the two domains. If there is a perpendicular angle between them then we call it 90° domain wall and the 180° domain wall separates the anti-parallel aligned domains. The Bloch wall is the best example of a 180° domain wall, in which the rotation direction of the magnetic moments lies in the plane of the wall, as shown in the Fig. 2.4a. The rotation direction of the magnetic moments for Néel wall lies perpendicular to the wall (Fig. 2.4).

The width of the domain wall Δ depends on the exchange stiffness A and the effective anisotropy K. This leads to,

$$\Delta = \sqrt{\frac{A}{K}} \tag{2.16}$$

Both the anisotropic term and exchange stiffness define the width of the domain wall. In the case of bulk structures, the wall width Δ is dominated by the magnetocrystalline anisotropy that favors the Bloch wall [12, 63].

However, in a thin film, the magnetization prefers to be in the plane of the structure to minimize the dipolar energy at the film surfaces. This brings up the Néel wall shape (see Fig.2.4a and b). Simply, in the case if the film thickness is bigger than the wall width, the wall tends to be a Bloch wall, otherwise it is a Néel wall [63].

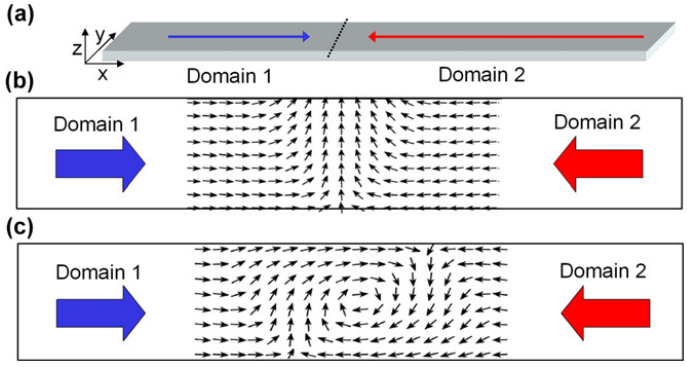

Figure 2.5: (a) Magnetic nanowire, having two opposite domains and a dotted domain wall in the middle of both. The geometry of the nanowire is presented with co-ordinated systems x, y, and z-axes. (b) and (c) present the spin configuration of the head-to-head transverse wall and vortex wall. Taken from [68]

Magnetically soft materials for nanostructures were used in this thesis, in which the anisotropy is dominantly caused by the shape. Consider a two domains nanostructure, having a head to head domain wall at the center, as shown by red and blue arrows in the Fig. 2.5a. The x-axis, y-axis, and z-axis show the length, width, and thickness of the nanostructure respectively. We can get different domain walls in such a nanostructure by simply choosing a different ratio between the thickness and the width. Fig. 2.5b and c show the simulated transverse wall and the vortex wall at the center of the nanostructure. The thin and narrow geometry favors the transverse wall and a vortex wall can occur in the

thick and wide nanostructure. The spins rotate in the plane of the nanostructure in transverse wall case, and in the case of vortex wall, the spins curl around the vortex core, pointing either upward or downward. Both have different energies because of having different geometry [68]. The stray field energy is dominating in the case of a transverse wall because it prefers thinner and narrower structure where it forces the spins to reside parallel to the edges. The exchange energy favors energetically the thick and wide nanostructure. Fig. 2.6 shows the phase boundary between vortex wall and transverse wall depending on the geometry of $Ni_{80}Fe_{20}$ nanostructures with widths ranging from 75 to 600 nm and thicknesses varying from 1 to 20 nm. [121, 144].

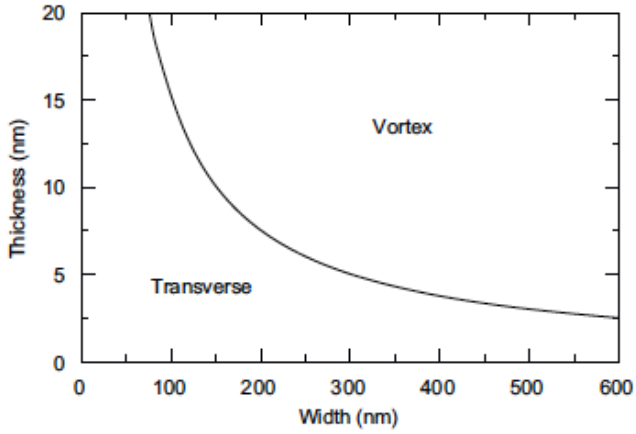

Figure 2.6: Phase boundary between the vortex and transverse walls in nanostructures of $Ni_{80}Fe_{20}$ with widths ranging from 75 to 600 nm and thicknesses from 1 to 20 nm, solely depending on their geometry. Adapted from [144].

It is now possible both experimentally [53, 67] and numerically [74, 104] to observe different magnetic ground states in a thin film. Each magnetic configuration depends on the geometry and the material used. The magnetic history of the structure has also an important role on the domain pattern [45]. Fig. 2.7 shows some of the magnetic ground states in the rectangular $Ni_{80}Fe_{20}$ nanostructures. These magnetic configurations in a soft material (like $Ni_{80}Fe_{20}$) nanostruc-

ture appear when the stray field energy and exchange energy are competing to each other. After applying an external field on the structure, it is difficult to confirm the configuration and the route of the magnetization that it will take from the saturated state to a demagnetized state. Nevertheless, it results in any one type e.g. Landau, diamond, C- or S-state. The magnetizations in the C- and S-state are parallel to the long edge and are high remanence states. The C-state looks more like an inclined Landau-structure, while the S-state is more similar to a diamond structure [45]. Both Landau and diamond states have singularity regions where the magnetization is rotating around them. Those regions are named vortices or anti vortices core, depending on the direction of magnetizations rotation [63].

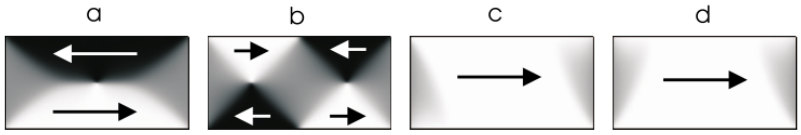

Figure 2.7: The simulated different ground-state configurations of a $Ni_{80}Fe_{20}$ rectangular structure. (a) Landau, (b) diamond state, (c) and (d) present the C- and S-state, respectively. The arrows present the orientation of the magnetization in each domain. Adapted from [45]

2.5 Spin-transfer Torque Basics

In the spin-transfer torque phenomenon, when a spin-polarized current enters a small magnetic microstructure, the angular momentum of spin polarized current transfers to the magnetization. This phenomenon was first proposed in 1996 by Slonczewski [122] and Berger [10]. For sufficiently large currents this torque will cause a magnetization precession or reversal and also propagate a domain wall in the direction of electron flow. This thesis is dedicated to the study of current induced domain wall motion in ferromagnetic nanostructures, which will be discussed here in detail.

2.5.1 STT in a Tri-layer Structure

Fig. 2.8a shows a typical spin-torque system. It has a non-magnetic layer (NM) sandwiched between two ferromagnetic layers, a thick F_1 layer and a thin F_2 layer. Initially, F_1 and F_2 are magnetized in different directions as shown in Fig. 2.8a [17].

After injecting a current through the system, the conduction electrons become spin-polarized while passing through the ferromagnetic layers. In the beginning, the injected spins are not aligned with the magnetization of the layer F_2, as shown in Fig. 2.8a, because the magnetizations of F_1 and F_2 are not collinear. Once they interact with the layer F_2 due to the spin-dependent scattering, they are aligned with local magnetic moments of F_2. In this event, the polarized spins lose their component transverse to the magnetization of the layer F_2. This transverse spin component is absorbed into the layer F_2 as a torque, so-called the spin-transfer torque [17, 85].

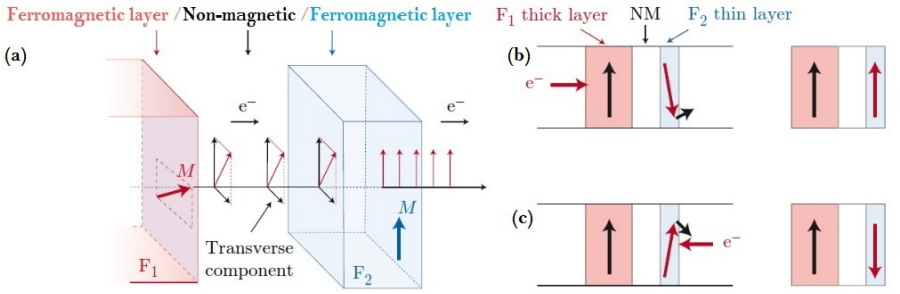

Figure 2.8: (a) Spin-torque system consists of a non-magnetic layer (NM) sandwiched between two ferromagnetic layers, F_1 and F_2. The transverse spin component of polarized spins (black) is absorbed into the thin layer F_2 in the form of a torque. (b) Back and forth switching of a layer F_2 by opposite polarity currents. Adapted from [17, 138]

Figs. 2.8b and c illustrate special switching cases into the spin-torque system by applying a current of opposite polarity. In the case of switching from the anti-parallel to parallel state as shown in Fig. 2.8b, a current is passed through

the system from a pinned layer F_1 to a layer F_2. The current is spin-polarized after passing through the pinned layer F_1 and exerts the spin-transfer torque on the F_2 layer's magnetization. Due to this, the magnetization of the layer F_2 is switched.

Now, in the case of switching from the parallel to anti-parallel state as shown in Fig. 2.8c, a current is passed through the system from a layer F_2 to a pinned layer F_1. Here, those electrons, having same spin direction as that of the pinned layer, pass through the pinned layer and some electrons, having an opposite spin direction, are reflected at the F_1/NM boundary and injected into the layer F_2 afterward. This reflected current exerts the effective torque on the magnetization of the layer F_2, establishing the anti-parallel state, as shown in Fig. 2.8c [95, 138].

Since having been observed on Co/Cu/Co trilayers [17], STT writing has been accomplished on many different systems, for example, exchange bias pinned layers, synthetic antiferromagnets (SAF) layers [103]. Also, it has been achieved in magnetic tunnel junction (MTJ) [52], in particular with MgO tunnel barriers [43]. Scientists have already exploited the STT-switching in many applications, including the spin-torque-transfer magnetoresistive random-access memory (STT-MRAM) [51] and racetrack memory [101].

In order to introduce a modified LLG equation with spin torque terms for magnetization dynamics, we will discuss the influence of an injected current on the local magnetization via the STT effect in a thin ferromagnetic nanostructure in the following subsections.

2.5.2 STT in a Thin Ferromagnetic Nanostructure

Fig. 2.9 illustrates the case of a simple thin ferromagnetic nanostructure having two non-collinear domains A and B. When a current is injected into it, the magnetic moments of the conduction electrons align themselves with the local magnetization of the domain A, as seen in Fig. 2.9. Once entering the region

of domain B, they are forced to turn their directions with respect to the localized moments of domain B. During this process, two events can happen. First, the boundary region, a domain wall, between two domains moves towards the right direction and secondly the angular momentum is transferred from the conduction electrons to the moments within the domain wall.

2.5.3 The Adiabatic STT Term

The magnetization of the local domain has major effect on the spins of conduction electrons during motion. The electron spins adiabatically follow the directions of the local magnetization when the magnetization of the local domain is small, so-called adiabatic STT effect. The action of the adiabatic torque on the domain wall is shown by white arrows in Fig. 2.9. This effect can be expressed as [7, 81, 82]:

$$\mathbf{T}_{adia} = (u \cdot \nabla)\,\mathbf{M} \tag{2.17}$$

where **u** is an effective spin current drift velocity, depending on current density j and its spin polarization **P**. This can be written as [7, 81]:

$$\mathbf{u} = \frac{jg\mu_B \mathbf{P}}{2\,|e|\,\mathbf{M}_s} \tag{2.18}$$

Later, it was realized that besides the adiabatic term, a non-adiabatic term is also contributing to the magnetization dynamics under certain conditions. This non-adiabatic term will be discussed in the next subsection.

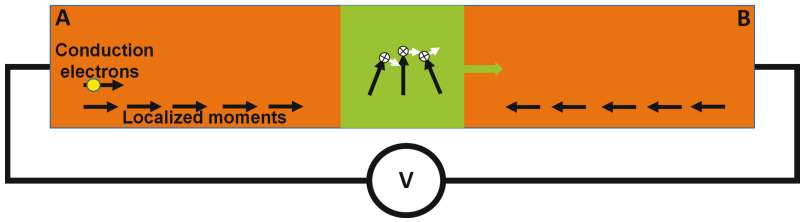

Figure 2.9: Sketch of the spin-torque in a thin ferromagnetic nanostructure, along with the schematic presentation of the action of adiabatic and nonadiabatic torques on the magnetic moments of a domain wall.

2.5.4 The Non-adiabatic STT Term

When the magnetization is large, a spatial mistracking arises between the conduction electron spins and the local magnetic moments. This happens because the local magnetization changes so quickly that the conduction electron spins cannot follow it. As a result, an additional torque, so-called the non-adiabatic torque, acts on the magnetization, as it is presented by black crossed-circles in Fig. 2.9. This non-adiabatic term acts on the local magnetic moments, like an applied magnetic field, which tilts the magnetic moments out-of-plane and as a result, the domain wall is moved forward by the torque of the demagnetizing field [138]. This term, included into the LLG equation [129, 151], gives:

$$\frac{\mathbf{dM}}{dt} = -\gamma \mathbf{M} \times H_{\text{eff}} + \frac{\alpha}{\mathbf{M}_{\text{s}}} \mathbf{M} \times \frac{\mathbf{dM}}{dt} - (u.\nabla)\,\mathbf{M} + \beta \mathbf{M} \times (u.\nabla)\,\mathbf{M} \tag{2.19}$$

where β is a non-adiabatic parameter that shows the mistracking of the electron spin. In the case of β=0, only the adiabatic torque exists, which means that there is no mistracking between the electron spin and the local magnetization. Though the non-adiabatic term is much discussed in the literature, it is still under debate [48].

Now, physicists passionately discuss the origin of non-adiabatic term β and further its relation with the damping factor, α [48]. Barnes and Maekawa [6] predicted that β and α are equal, but Kohno et al. [73] estimated the non-adiabatic parameter and claimed that both are not equal. Xiao et al. even questioned the existence of β by presenting the spin-flip scattering phenomenon. However, they claimed an oscillating non-adiabatic term for high magnetization gradients [145]. Garate et al. [35] have proposed the dependency of β and α on the temperature and disorder. They also related both constants to the band structure and intrinsic spin-orbit interaction [35]. Thiaville et al. simulated the domain wall motions for perfect nano-stripes and concluded that β affects the domain wall motion [87, 129].

Still, β and α are not easy to determine, but the recent study of M. Eltschka et al. [30] and T. Taniguchi et al. [128] revealed that the magnetization gradient is

strongly influenced by β. A. Vanhaverbeke and M. Viret came to the conclusion [140] that β depends on the domain wall width, too [28, 48, 87, 138].

2.6 Temperature Effects on the Nanostructure by Current Densities

Experimentally, the current induced domain wall motion in nanostructure needs a large current density up to 10^{12} A/m^2 [149]. However, such huge current density increases the temperature of the system and sometimes raises it near to or above the Curie temperature of the material used. Due to this, the spin configuration of the system can completely change or even the single domain structure splits into multi-domains [148]. We will discuss the effect of temperature on the domain patterns in this section and will present our results based on temperature effects on the spin structures in chapter 5 of this thesis.

In 2005, Yamaguchi et al. observed that the temperature of the $Ni_{81}Fe_{19}$ nanostructure (on thermally oxidized Si substrate, having a 10 nm thickness and 240 nm width),when the current-driven domain wall motion occurred, raised up to the Curie temperature of the material $Ni_{81}Fe_{19}$ used (830 K), while applying a current density of 7.5×10^{11} A/m^2. By further increasing the current density, they found multi-domains in the sample via magnetic force microscopy after cooling down. They also measured the standard temperature dependence of the sample resistance during the pulse injection and found that the sample resistance increased with the current density, suggesting Joule heating of the sample. Hence, they suggested to take into account thermal effects like decrease in magnetic moment, spin wave excitation, and the depinning of a domain wall while studying the current-induced domain wall motion [146].

Chun-Yeol You et al. [149] presented an analytical expression to approximate the increase in temperature of the heated nanostructure as a function of current density [33] (Eq. 2.20), which is important in the study of current induced domain wall motion. They have made the following main assumptions for the model. (i) the substrate thickness is larger than the nanostructure length,

(ii) the whole nanostructure is at same temperature, (iii) the temperature of both the nanostructure and the interface are same, (iv) the heat source is at the interface from the substrate point of view, (iv) because of the small surface area of the nanostructure, the effect of convection is ignored for the model, (v) the heat capacity of the nanostructure is neglected, (vi) assume heat dissipation into the substrate only. With the above assumptions, they derived the following analytical expression [33, 147, 148, 149]:

$$\Delta T = \frac{whJ^2}{\pi k\sigma} \operatorname{arc\,sinh}\left(\frac{2\sqrt{tk/\rho C}}{0.5w}\right) \tag{2.20}$$

where w, h and σ are width, height and conductivity of a structure respectively. J is the current density applied to the structure. k, ρ, and C are the thermal conductivity, mass density, and specific heat capacity of the substrate used [33].

J. Yoon et al. [147] performed experiments in 2008 on two different nanowire types, 600 nm wide L- and 300 nm wide C- shaped. They observed a significant Joule heating effect on the samples when the applied current density exceeded the critical current density of $5.5\times\ 10^{11}$ A/m^2. After heating and cooling, they detected multi-domain structures in the sample. The splitting up of a single domain into multi-domains was considered a signature of the Joule heating in the sample. The energy barrier decreases due to temperature increase and the single domain transforms into multiple domains. Also, the system needs to reduce the magnetostatic energy, therefore the multi domain state occurs. This shows that the temperature increase is strongly depending on the current density. They estimated an increase in the temperature of the sample up to Curie temperature of $\mathrm{Ni_{80}Fe_{20}}$ [147] by following the equation 2.20. Their results show that the temperature effect is very important to discuss while driving the domain wall via current pulses.

H. Fungohr et al. theoretically discussed the Joule heating effect on the ferromagnetic nanowires via electric currents [33]. In one of their proposed cases, they estimated the temperature increase in a nanowire without a substrate. Having an uniform current density J through a nanowire, they proposed the

equation for the time evolution of T:

$$\frac{dT}{dt} = \frac{J^2}{\rho C \sigma} \tag{2.21}$$

where σ is the uniform conductivity, C is the specific heat capacity and ρ is the density of the material used. The change in temperature will be at constant rate as all the parameters on the right hand side are constant. They estimated the temperature increase for the case of $Ni_{80}Fe_{20}$, having C= 430 J/(kg K), ρ = 8700 kg/m^3, σ= 4 $\times$ 10^6 $(\Omega m)^{-1}$ and a current density of J=10^{12} A/m^2. The equation 2.21 leads to [33]:

$$\frac{dT}{dt} = 66.83 \text{ K/ns} \tag{2.22}$$

This is the amount of temperature increase for the uniform current density and for the chosen material parameters. This will change if one changes the current density. In our case, we have a maximum current density of J=8.7 $\times$ 10^{11} A/m^2 and the pulse width is of 100 ns (for some cases) while applying it through the nanostructure in single pulse experiments (detailed in the final chapter). This means that the temperature increase of our structure goes up to 6000 K if we exclude the heat dissipation into the substrate.

In conclusion, a higher current density for current induced domain wall motion rises the temperature of the sample up to Curie temperature. One can decrease the effect of temperature, which can be done by choosing a substrate having good electrical insulation and the improved heat dissipation [78, 138].

2.7 Possible Pinning Effects in Nanostructures

There are different types of defects that affect the domain wall motion like edge roughness, material defects, and structure imperfections. These defects can be reduced by the latest lithography facilities up to some extent but still, the controlled motion of a domain wall is a challenging task. On the other hand, reliable pinning sites can be important features for attaining high data stability [37]. The domain wall motion depends on the local energy landscape of the place where it is residing. It is possible to generate artificial pinning sites to have a desirable energy landscape for the domain wall motion [37].

If there is a variation of the width of a nanostructure, in the first approximation it can be predicted that the energy is minimized when the domain wall settles at a place with a narrow width. This offers the possibility to force a domain wall to a certain place by preparing a geometrical constriction, like a notch in the nanowire [68]. In our case, we mostly used a triangular-shaped notch of a length of 200 nm within a nanostructure of width 1000 nm (see scanning electron microscope (SEM) image in Fig.2.10c).

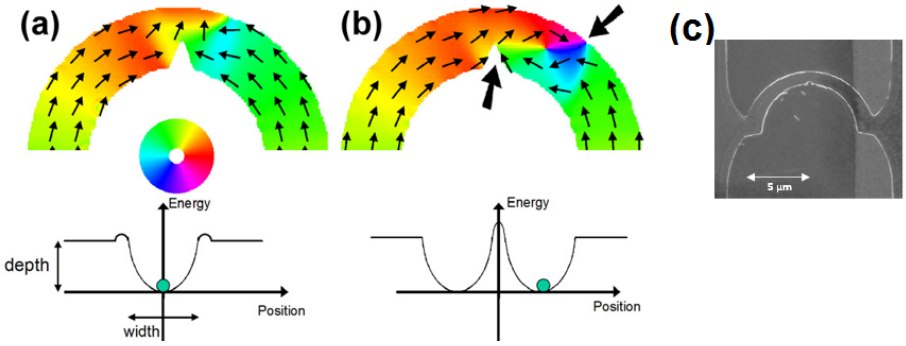

Figure 2.10: (a) Transverse wall inside the constriction along with the schematic of the potential landscape. (b) Vortex wall accompanied by the potential landscape. The vortex wall is pinned next to the constriction and the potential landscape has a double well. The black arrows are showing the positions where the stray field enters and leaves. (c) Scanning electron microscopy image of our own sample. (a) and (b) are adapted from [68]

Fig.2.10a depicts a transverse wall around the constriction along with the schematic of the relevant potential landscape and 2.10(b) shows a vortex wall accompanied by its equivalent potential landscape. The vortex wall is pinned next to the constriction and the potential landscape has a double well. The wall initial position and its spin configuration vary with the changing geometry or applying external sources like current pulses or external field. This automatically modifies the potential landscape. Both transverse wall and vortex wall have a very different response to the constriction. The transverse wall seems to be attracted towards the constriction, but the vortex wall appears either on the left or on the right side of constriction, like a repulsive force from the constric-

tion. By decreasing the width of the constriction, we can increase the depth of the potential well. This means that walls will be strongly pinned in the narrower constriction [68, 69, 71, 72].

Kläui et al. applied an external magnetic field to probe the pinning strength of the wall from the constriction. They found that the magnetic field needed for depinning the wall from the geometrically induced pinning constriction is six times (335 Oe) larger than the field needed to move a wall in a ring without a constriction (60 Oe) [68, 69]. Of course, the magnitude of magnetic field needed for depinning the domain wall in different geometrical samples would be different.

Chapter 3

Sample Fabrication and Magnetic Imaging with XMCD-PEEM

This chapter covers two major aspects, the first concerning the fabricated ferromagnetic nanostructures and the second belongs to the measurement imaging techniques. In the first part of this chapter, we present the procedure of the sample fabrication (see section 3.1). This was the most challenging task towards successful experiments. The second part covers the magnetic circular dichroism-photoemission electron microscopy (XMCD-PEEM) based magnetic imaging technique (see section 3.3), that is used to visualize current induced domain wall motion (CIDWM) with single current pulses and in pump-probe experiments. At the end of the chapter, we discuss the principle of the aberration corrected LEEM/PEEM microscope (see subsection 3.3.2), which is installed at the Jülich beamline BESSY II Berlin.

3.1 Sample Fabrication

The requirements for the samples for CIDWM studies in our PEEM are quite special and we had to adapt our fabrication method to meet them. The spin-transfer torque (STT) induced magnetization dynamics can only be studied in soft magnetic materials, such as $\mathrm{Ni_{80}Fe_{20}}$ alloy, having low anisotropy, low coercivity, high magnetic permeability, and small saturation magnetization (see details on used soft materials in this work in section 3.2).

3.1.1 Sample Design and Fabrication Process

Well-known lithographic techniques that are capable of patterning nanoscale features are electron beam lithography and photolithography. In the electron beam lithography, a focused beam of electrons is scanned across the surface of sample having a resist on top of it. In the photolithography, UV light is used to expose a layer of photoresist through a glass mask. The electron beam lithography is good for making very refined nanostructure and photolithography is used for patterning bulk structures. For obtaining our nanostructures, we used both electron beam lithography for writing the nanostructure and photolithography for making the contact pads along with the ground fields. The complete process of fabricating a sample will be explained in the next paragraphs.

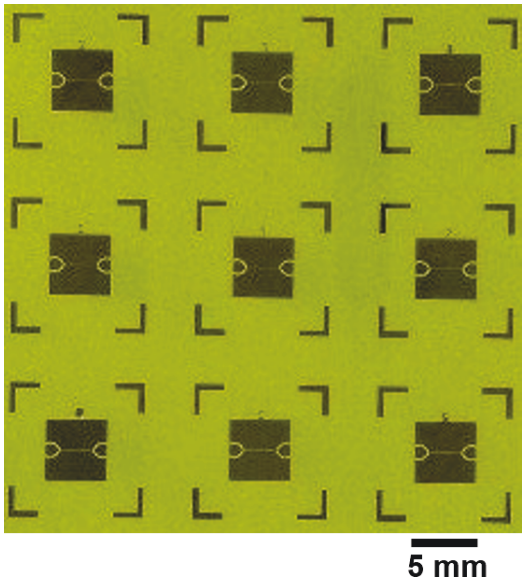

Figure 3.1: A photograph of a glass mask having nine different sample designs

First of all, we produced a glass mask having layouts of our desired sample. It consists of a transparent plate covered with a patterned film of opaque material. This plate is made of fused Quartz which is transparent to deep Ultra

Violet light. In our case, the layouts consist of contact pads along with ground fields around the nanostructure region like a co-planar wave guide, as shown in Fig. 3.1. As the contact pads are far away from the nanostructure and broad in size, the current density is low at a contact point.

Fig. 3.2 shows all steps of the process which are followed during the sample growth. First, we clean the substrate (GaAs) in acetone, isopropanol (IPA) and blow with a Nitrogen gun (see Fig. 3.2a). After that, we dehydrate the substrate on a hot plate or cabinet dryer at 180 °C for 5 minutes.

To introduce so-called undercut for getting good adhesion of metals, high-contrast development and improved lift off processes, a bilayer polymer polymethylmethacrylate (PMMA) can be used where a PMMA with lower molecular weight is more sensitive to electron beam exposure than the PMMA of heavy molecular weight. In this work, the substrate is covered by high electron sensitive resist PMMA/MA 33 % (copolymer e-beam resist AR-P 617.08 diluted with AR 600-07, 1: 1)) by a spin-coating method. This PMMA layer generates a thin film of 150 nm on the top. Then, the second layer of thickness 270 nm of PMMA 950 K (e-beam resist AR-P 679.04) is spin-coated on top of the first layer. Fig. 3.2b displays the bilayer of PMMA spin-coated on the substrate surface (at 4000 rpm). When the bilayer PMMA is exposed to the electron beam as seen in Fig. 3.2c, the primary electrons penetrated in the bilayer and inner structure of PMMA becomes a trapezoid shape (so-called undercut) due to scattered electrons. Next, it is developed in a solution of e-beam developer AR 600-55 in order to remove the exposed resist (see Fig. 3.2d). After that, the substrate is placed in a molecular beam epitaxy (MBE) or sputter deposition system where Cr/$\mathrm{Ni_xFe_{1-x}}$/Au is evaporated or sputtered (see Fig. 3.2e). Cr is used as a sticking layer for the $\mathrm{Ni_xFe_{1-x}}$ and Ta or Au is employed as a capping layer to prevent $\mathrm{Ni_xFe_{1-x}}$ from the oxidation. At the end, a "lift off" is done by heating the substrate in acetone at 55 degrees for one hour to remove the unexposed resist (see Fig. 3.2f).

Next, a thin layer of the negative photo resist is spin coated on the substrate

at 4000 rpm (Fig. 3.2g) and then the glass mask, having a pattern of contact pads along with ground fields, is exposed by photo-lithography (see Fig. 3.2h). After developing in chemical-726 solution (see Fig. 3.2i), we have done the reactive ion beam etching to remove dust material from the surface of a substrate (see Fig. 3.2j) before the final sputtering of Cr/Gold (see Fig. 3.2k). At the end, the final lift off is done (see Fig. 3.2l).

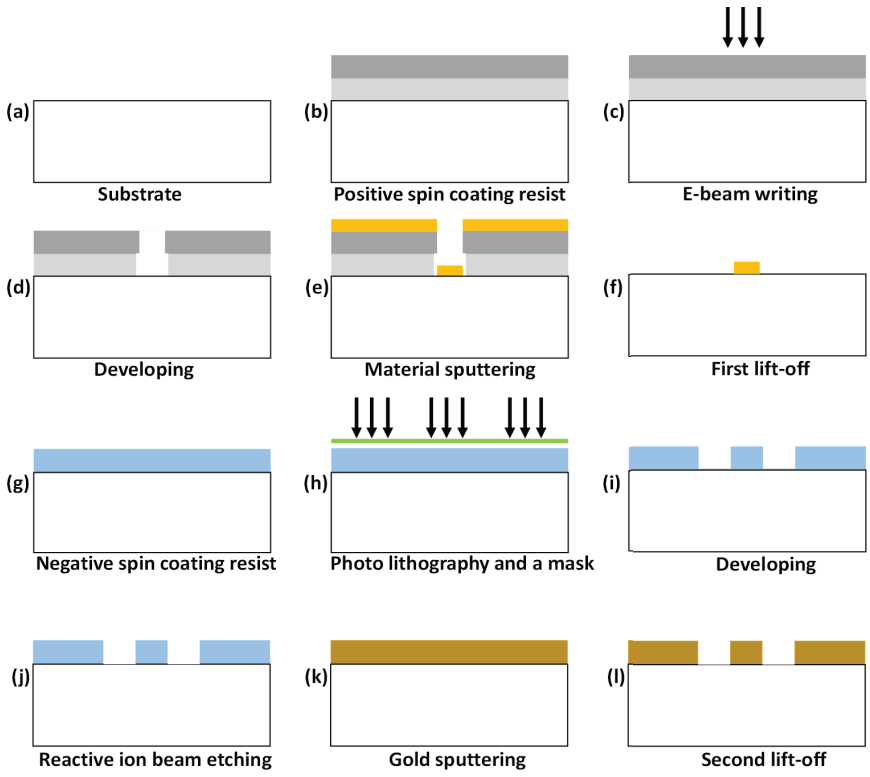

Figure 3.2: Schematic overview of a sample growth using lift-off processes along with electron beam exposure and photo-lithography.

Fig. 3.3 shows the different looks of the sample structure at the end of the fabrication process. Fig. 3.3a represents the camera image of the 5 mm$\times$5 mm GaAs substrate with a written structure. Fig. 3.3b shows the optical microscope

view of a complete sample with contacted pads surrounded by grounded fields and Fig. 3.3c shows also the optical microscope image of a centered V-type nanostructure within a gap of 20 μm. Fig. 3.3d and e display the PEEM and XMCD images of a V-type nanostructure.

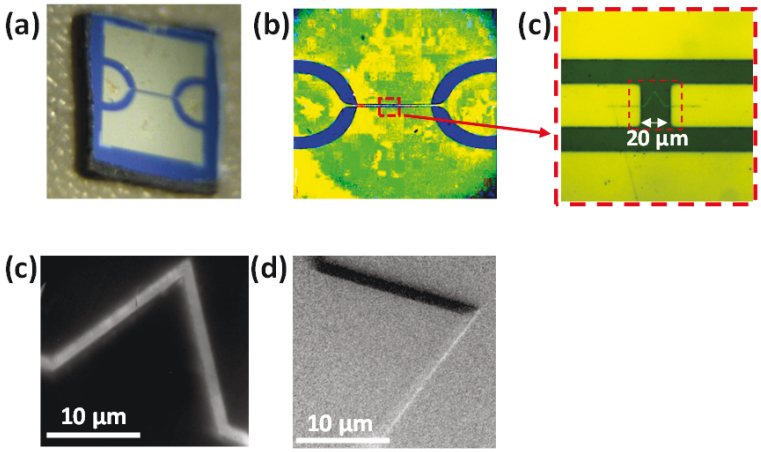

Figure 3.3: Different views of the sample structure at the end of the fabrication process. (a) The 5 mm×5 mm Si substrate with a written structure. A (b) and (c) show optical microscope images of the sample with a centered V-type region of a gap 20 μm. (d) PEEM image of a V-type nanostructure. (e) XMCD image of a V-type nanostructure, showing the magnetization pattern.

3.2 Properties of Different NiFe Alloys

Soft magnetic materials are widely used for a variety of low and high frequency applications, such as transformer cores, flux-guidance at permanent-magnets, microwave applications and storage devices [120]. These materials can be easily magnetized and demagnetized. The main parameter, used as a feature of merit for soft materials, is the intrinsic low coercivity. In soft materials, this is several orders of magnitude smaller than in hard materials. Another property of soft materials is their initial permeability $\mu_r = (dM/dH)_0$, which may exceed 1000 [120]. In the case of high-frequency applications, small coercivities are more

important than a high permeability because these applications require small hysteresis losses [120]. The parameters like electrical resistivity and saturation magnetization are also important features for soft materials.

Soft magnetic materials include a wide variety of NiFe alloys. These alloys are used over a wide range of compositions, from 20% Ni to 80% Ni. The properties vary extremely over this composition range and hence the optimum stoichiometry needs to be selected for a particular application [106]. In this work, we have used NiFe alloys with two different stoichiometries, $\mathrm{Ni_{80}Fe_{20}}$ and $\mathrm{Ni_{20}Fe_{80}}$ for studying the current induced domain wall motion. We used $\mathrm{Ni_{20}Fe_{80}}$ for the static (single pulse) experiments, first because of the availability, later the large magnetic moment (see table 3.1) made it easier to visualize the magnetic texture as the XMCD effect is proportional to the moment. The disadvantage was the largest magnetostriction, which can lead to destruction of the samples. For the dynamics experiment, due to the lower available current density, we used the material with the lowest coercivity, $\mathrm{Ni_{80}Fe_{20}}$.

Table 3.1 shows the comparison of different properties of the $\mathrm{Ni_{80}Fe_{20}}$ and $\mathrm{Ni_{20}Fe_{80}}$ alloys. The $\mathrm{Ni_{80}Fe_{20}}$ alloy has low saturation flux density, coercivity, Curie point, lower resistivity, magnetostriction and magnetic moment per unit formula than the other NiFe alloys, as shown in table 3.1.

Table 3.1: Typical properties for soft magnetic NiFe alloys

Properties	$\mathrm{Ni_{80}Fe_{20}}$	$\mathrm{Ni_{20}Fe_{80}}$	References
Saturation flux density B_s (T)	1.0	2.2	[23], [23]
Easy-axis Coercivity H_c (Oe)	0.2	2.5	[23], [23]
Magnetic moment per formula unit (μ_B)	0.59	2.07	[42], [102]
Resistivity ρ ($\mu\Omega - \mathrm{cm}$)	20	35	[23], [23]
Magnetostriction λ (ppm)	$\sim$0	+25	[66], [23]
Curie Temperature T_c (K)	750	860	[87],[102]
Crystal structure	fcc	bcc	[16], [23]
Lattice parameter (nm)	0.356	0.359	[16], [89]

$Ni_{20}Fe_{80}$ stoichiometry could be used in devices operating at higher temperatures and $Ni_{80}Fe_{20}$ stoichiometry commercially can be used in many applications like sensitive relays, current transformers and magnetic recording heads etc [79]. The references [23, 77] are highly recommended to the interested readers to elucidate the difference between both NiFe alloys.

3.3 XMCD-PEEM as an Imaging Technique

Numerous magnetic imaging techniques are used to investigate and map the elemental, chemical and magnetic properties of complex nanostructures. Each one has its own range of spatial and time resolution. The strength of XMCD-PEEM is its element specificity and its magnetic contrast. We will discuss this mechanism along with some other important features in next subsections.

3.3.1 Storage Rings and Synchrotron Radiation

When oscillating electric charges, for example, electrons, are moving with relativistic speeds are forced by magnetic fields to follow curved paths, as a result, these electrons are emitting light in their motion direction, called synchrotron radiation [91].

Nowadays in radiation sources, like storage rings, this radiation is used in different research fields like physics, chemistry, nanotechnology and material sciences etc [91]. In a storage ring, the electrons are forced to move in a circular trajectory by bending magnets. The Lorenz equation describes the acceleration of those electrons:

$$\frac{d\mathbf{p}}{dt} = e(\mathbf{E} + \frac{\mathbf{v} \times \mathbf{B}}{\mathbf{c}}) \tag{3.1}$$

where $\mathbf{p}$, e and $\mathbf{v}$ are the electron momentum, charge and velocity respectively. $\mathbf{E}$ and $\mathbf{B}$ are the electric and magnetic fields. The radiated power of the relativistic electron ($\beta = \mathbf{v/c} \approx 1$) while moving in a circular path, with a radius of curvature, $\mathbf{R}$, can be approximated as [57]:

$$P = \frac{2\mathbf{c}}{3} \frac{e^2}{\mathbf{R}^2} [\frac{E}{mc^2}]^4 \tag{3.2}$$

where E, $\mathbf{c}$ and mc^2 are the electron energy, velocity, and the rest mass energy respectively. The radiated power from the electron strongly depends on its energy. For relativistic electrons, the distribution of emitted radiation transforms to a narrow cone $(\beta \approx 1)$. The emission angle of synchrotron radiation is $\Theta = \frac{1}{2\gamma}$, where $\gamma = \sqrt{1/(1 - \frac{\mathbf{v}^2}{\mathbf{c}^2})}$. For BESSY, γ is 3320, and Θ= 0.15 mrad $(0.01°)$ [26].

Today, insertion devices, like undulators, are implemented in the storage ring to get high photon brightness and also to modulate the electron trajectories for getting specific polarization selection of the synchrotron radiation. An undulator consists of periodic permanent magnets (see Fig. 3.4). Due to the static magnetic field lines between the opposite magnets, the electrons are forced to follow oscillating paths and as a result, emit radiation. The interference of the radiation of different magnets results in a spectrum with quasi-monochromatic peaks [115]:

$$\lambda_n = \frac{\lambda_U}{2n\gamma^2}[1 + \frac{K^2}{2} + \gamma^2\theta^2] \tag{3.3}$$

where γ is the Lorentz factor depending on electron velocity, λ_U is the periodic wavelength of the alternating magnet pairs and θ presents the observation angle with respect to the undulator axis. K is the deflection parameter, given by:

$$K = \frac{eB\lambda_U}{2\pi mc} \tag{3.4}$$

where K depends on the magnetic field. The magnetic field can be modified by changing the phase shift between opposite arrays of magnets. By this method, the polarization of synchrotron radiation and the wavelengths λ_n of the undulator harmonics can be tuned [41].

Fig. 3.4 shows different possible polarization cases. Fig. 3.4a presents the linear horizontal case where both upper and lower magnet arrays have a zero shift with respect to each other. We can get vertically polarized x-rays by simply shifting the upper right and lower left magnets by a length of $\lambda_U/2$ and right circularly polarized x-rays by a shift of $\lambda_U/4$. Similarly, the left circularly polarized x-rays can be tuned by a shift of $-\lambda_U/4$. For details, see [113, 115] and

[26].

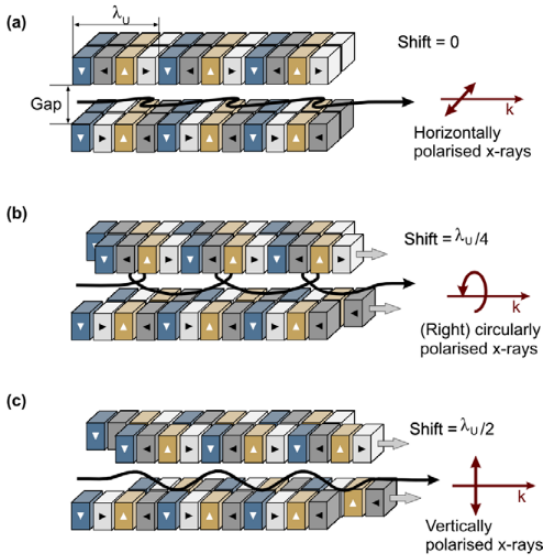

Figure 3.4: Schematic overview of an undulator with three possible cases. (a) Shows horizontally polarized case. (b) Presents right circularly polarized. (c) Displays vertically polarized case. A fourth possible case of left circularly polarized x-ray is not shown here. Taken from [115].

Fig. 3.5 shows the schematic view of a beamline where radiation from the undulator is guided to the sample by the arrangement of different horizontal and vertical mirrors along with the spherical grating unit. Light needs to be monochromatic and well-focused while being used in an experiment. For this, the selection of a single photon energy of incoming beam in the soft x-rays range can be tuned by a grating unit via Bragg's law [41]:

$$\lambda_n = d(cos\theta_i - cos\theta_j) \tag{3.5}$$

where d presents the line spacing of the grating, θ_i and θ_j are the entrance and exit angles of the beam. Spherical gratings are employed to focus one wavelength from the entrance slit onto exit slit. This setup is used in the FZ Jülich soft

X-ray beamline UE56/1-SGM at BESSY-II, Germany. Finally, the refocussing mirrors are used to focus the divergent beam onto the sample [26, 41].

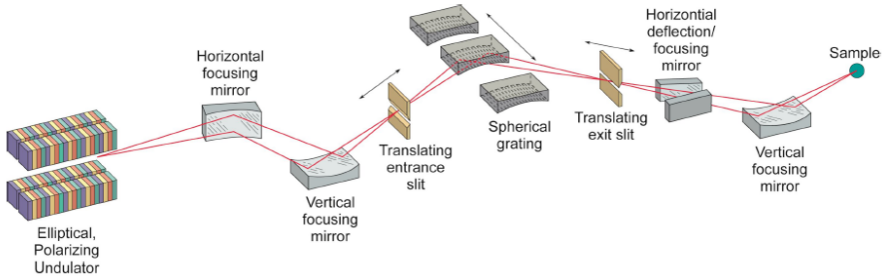

Figure 3.5: Schematic view of an undulator beamline. Taken from [4].

3.3.2 Photoemission Electron Microscopy

Photoemission Electron Microscopy is an imaging technique that is to excite the electrons from the sample surface by incident photons and to create a real-time magnified image of the emitted (secondary-) electrons on the phosphor screen. In 1930, Ernst Brüche and Johannson have tested the PEEM principle first with UV light [13]. After access to a tunable synchrotron radiation, Tonner and Harp successfully had taken PEEM images in 1987 [63, 132]. A few years later (1993) the XMCD effect was introduced in the PEEM technique for exploiting the magnetic contrast of materials [125].

Fig. 3.6 shows the schematic view of the combined LEEM-PEEM (FE-LEEM P90 AC) microscope, fabricated by SPECS, installed in the FZ Jülich beamline UE56/1-SGM at BESSY-II, Germany. The PEEM mode of the microscope is utilized in this thesis to perform the XMCD-PEEM measurements. In its PEEM mode, the incident photons illuminated the sample with an angle of 20° and an image is formed on the phosphor screen by the emitted secondary electrons. In LEEM mode, the electrons are emitted by a cold field emission gun with 15 keV energy. Then the electrons are focused on the entrance plane of first Magnetic Prism Array (MPA1) by the combination of the gun lens (GL) and a Condensor

lens (CL). After that, the beam is deflected with a 90° angle towards the objective lens system in MPA1. The objective lens system consists of a magnetic transfer lens (M1) and the objective lens (OL). The first prism MPA1 works as a separator in LEEM mode, i.e. separating the incoming electron beam from the imaged electrons of the sample. There is 1.5 mm distance between the objective lens and the sample. The diffraction image forms in the back focal plane of the objective lens, which is further transferred to the entrance plane of MPA1 by a lens M1. Finally, the virtual image forms in the center of MPA1 and the real image creates at the diagonal of MPA1 where it is at a distance of 60 mm from the sample [135].

In the next stage, the beam is deflected again by a 90° angle but this time towards the second Magnetic Prism Array (MPA2). The second prism also acts like a separator, deflecting the entering electrons to the aberration correction mirror from the reflected one. There is an electrostatic transfer lens (EL), located between MPA1 and MPA2. This lens transfers the diffraction image from the center of MPA1 to the center of MPA2. MPA2 deflects the electrons over a 90° towards the mirror and transfers the diffraction pattern at the center of a magnetic lens M2. M2 further transfers it to the center of M3, where the magnification factor at the M3 is 8.5×. Next, the M3 transfers the diffraction pattern to the reflection plane of the electron mirror. The virtual image is aberration-corrected by the electron mirror and it then sends the real space image back to the M3. The image goes back to M2 from M3 and M2 transfers it to the center of MPA2 with a magnification factor of 38. Afterward, MPA2 deflects the pattern over a 90° angle towards the projector column and places it at the center of P1. The P1 plane has also a contrast aperture, normally used to select a certain angular range of the electron distribution. The combined setting of lenses, P1 up to P4, displays the aberration corrected image on a phosphor screen. Finally, a CCD camera digitizes the image [135].

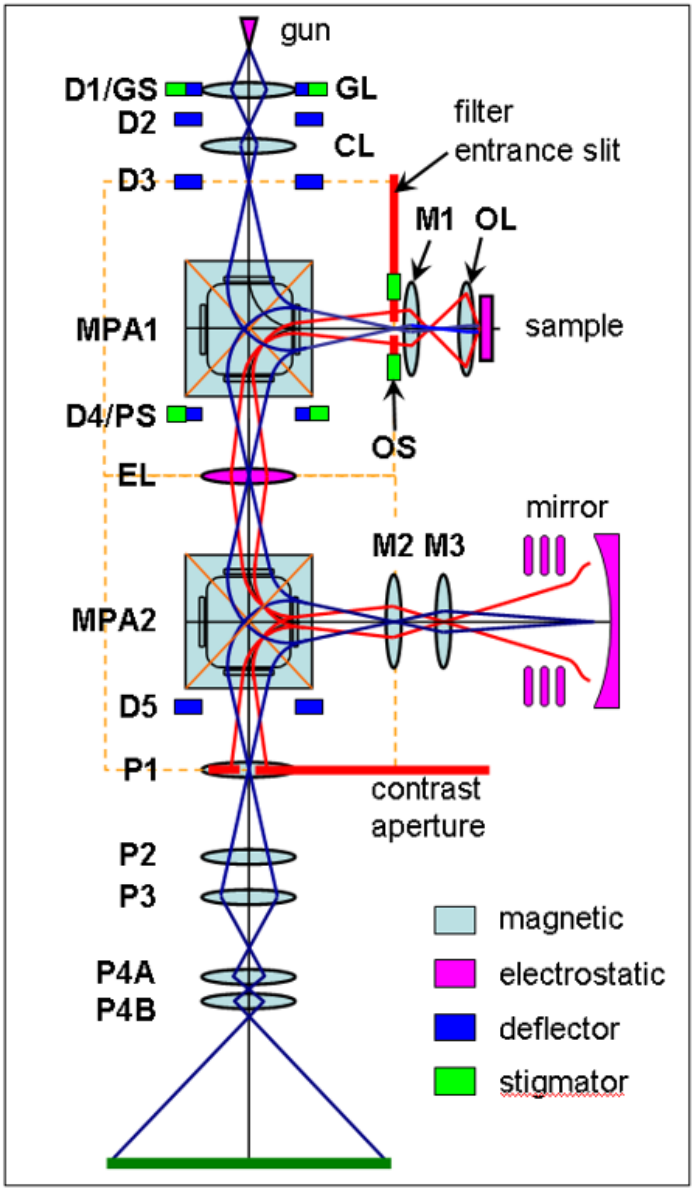

Figure 3.6: Schematic presentation of the aberration corrected PEEM/LEEM microscope. Taken from [136]

Fig. 3.7 shows the energy filter setup, used to obtain images formed only by electrons of a narrow energy band from within the spectrum. The dual-lens objective system contains an objective lens and a transfer lens, for simplicity, is shown by a single objective lens in the given figure [134]. Emitted electrons from the sample pass through the objective lens and generate concentric Ewald spheres for different electron energies in the entrance plane to the prism. A narrow slice out of the 2D angular distribution can be chosen by introducing the entrance slit. Finally, a (k_y, E) spectrum emerges in the exit plane of the prism array. A contrast aperture can be inserted at the desired electron energy for the energy-filtered image [134].

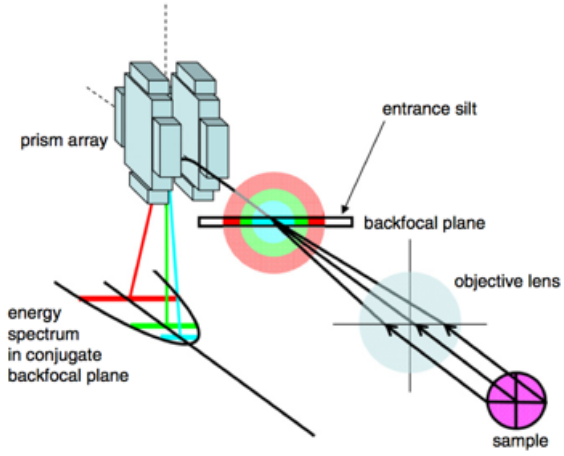

Figure 3.7: A three-dimensional schematic view of the energy filter setup. Taken from [134]

We employ a few **PEEM imaging modes** at the FZ Jülich LEEM/PEEM microscope. All of these modes can be realized through the same optical setup, but they have different contrast mechanism.

3.3.3 Threshold PEEM

Threshold PEEM operates with a low photon energy source like a mercury (Hg)-discharge lamp that gives just enough energy to the electrons to escape from the

sample. The maximum kinetic energy of the escaping electrons can be written by Einstein's equation [29]:

$$E_{kin} = h\upsilon - \phi \tag{3.6}$$

where $h\upsilon$ is the photon energy and ϕ is the work function of the material. Due to such a low photon energy excitation, the escaping electrons have a small energy width, as it is shown by the green color area in Fig. 3.8. An image contrast originates from variations of the work function or structural changes on the surface of the sample.

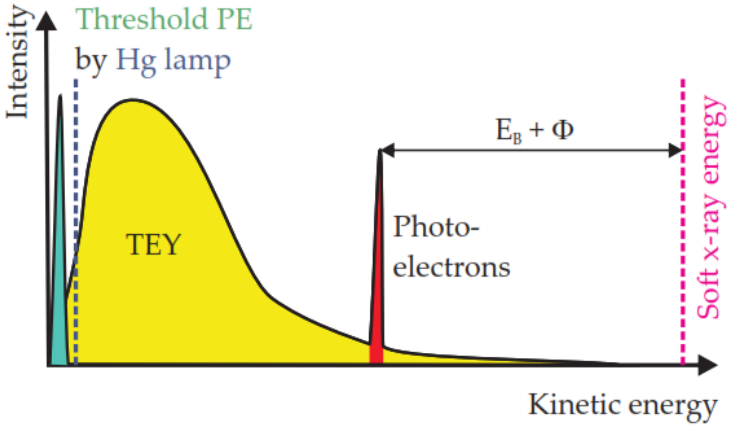

Figure 3.8: A sketch of the photoelectron distributions in three different imaging modes. The dotted lines indicate the photon energies of the incident light and the colored areas present the measured intensities in a PEEM experiment. The blue line denotes the Hg lamp photon energy and the green area is the distribution of kinetic energies from the Hg lamp. The yellow window describes the total electron yield (TEY) area that is detected by soft X-ray PEEM. The red peak is the photoemission line of a core level which can be recorded in an energy filtered experiment. Taken from [63]

3.3.4 X-PEEM and Magnetic Circular Dichroism

In 1895, X-rays are discovered by Röntgen [108]. After that, X-rays were seriously used to explore the magnetic features of the materials by X-ray absorption

techniques [31]. A half century after Röntgen discovery, X-rays based linear dichroism in rare-earths were found by Thole et al. [130]. A year later, Schütz et al. observed the XMCD with circularly polarized light in iron for the first time [119]. XMCD can be used as a contrast mechanism and it is specifically used along with the X-PEEM for this thesis. We will discuss it further in the following paragraphs.

The soft X-ray based PEEM, with selected photon energies and tunable polarizations, can choose the core level resonances to get the elemental contrast, chemical and magnetic features of the materials. The electron kinetic energy distribution range contains primary photon with $E_{kin} = h\upsilon - \phi - E_B$ (where E_B is the binding energy of core electron), plus lower energetic secondary electrons along with Auger electrons [63, 118].

A core-level electron absorbs a photon of the energy $h\upsilon$ and if the photon energy is close to E_B, it is excited to an empty state near the Fermi level. According to Fermi's Golden rule, the transition probability from an initial state i to the final state f is given by:

$$P_{if} = \frac{2\pi}{\hbar} \langle f | I | i \rangle \, \delta \left(E_f - E_i - h\nu \right) \rho \left(E_f \right) \tag{3.7}$$

where $\rho \left(E_f \right)$ is the density of the final states and I presents the interaction operator between electron and photon, i.e. $I = \frac{e}{m} pA$ and A is an electromagnetic potential. Here, $\langle f | I | i \rangle$ is the transition matrix between initial and final states. This matrix is helpful to describe the transition process. So, the following dipole selection rules are applicable between states under Fermi's Golden rule:
$\Delta l = \pm 1$
$\Delta m_l = 0, \pm 1$
where l is the orbital angular momentum quantum number and m_l is the orbital magnetic quantum number.

In the case of $3d$ metals, the dipole selection rules apply to the possible transitions of electrons from the occupied $2p$ core levels to the available $3d$ empty levels, as shown in Fig. 3.9.

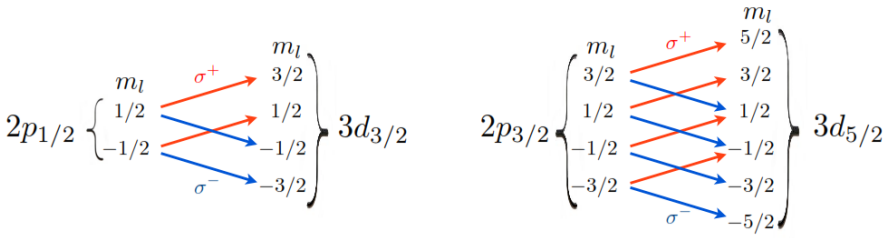

Figure 3.9: Possible transitions of $2p$ core level electron into free $3d$ levels according to selection rules for $\Delta l = +1$, $\Delta m_l = \pm 1$. Taken from [41, 96]

In $3d$ metals, the scheme of transition from $2p$ to $3d$ levels can be illustrated, as shown in Fig. 3.10. When the photon energy is close to E_B of the core levels of the transition metal L-edge, the electrons are excited to empty states above the Fermi level. This process generates a core hole. The core hole decays and in this energy range mainly Auger electrons are emitted. Auger electrons further scatter and produce secondary electrons. So, most of the de-excitation events occur in the form of emitted electrons. This makes it a favorable process to get absorption data. The $2p$ level splits into two $2p_{3/2}$ and $2p_{1/2}$ core levels due to spin-orbit coupling that result into two primary resonances, L_3 and L_2 respectively. There are spin dependent density of states in the final unfilled bands of ferromagnetic materials. Therefore, the absorption coefficients are different at L_3 and L_2 peaks for right circularly polarized σ^+ and left circularly polarized σ^- helicities of the X-rays. The difference in the absorption coefficients is the XMCD effect [20].

The transition probabilities for L_3 and L_2 peaks of $3d$ metal can be calculated by Clebsch-Gordon Coefficients. The circularly left polarized light excites 25% spin $\uparrow$ electrons from the $2p_{1/2}$ level and 62.5% spin $\downarrow$ electrons from the $2p_{3/2}$ levels to the $3d$ empty band and the circularly right polarized light stimulates 75% spin $\uparrow$ electrons from the $2p_{1/2}$ level and 37.5% spin $\downarrow$ electrons from the $2p_{3/2}$ level to the $3d$ empty band [48, 110] (see Fig. 3.10a).

Fig. 3.10b shows the X-ray absorption intensities along with a XMCD image,

measured at left and right circularly polarized light for a permalloy nanostructure at the Fe-edge (709.6 eV). First, the data are recorded for each polarization at the Fe-edge. After that, the difference of both polarizations is divided by the sum of both to separate the magnetic signal, as shown by the equation for the asymmetry A_{XMCD}:

$$A_{XMCD} = \frac{I_{\sigma^+} - I_{\sigma^-}}{I_{\sigma^+} + I_{\sigma^-}} \tag{3.8}$$

where I_{σ^+} and I_{σ^-} present the intensity distribution for right and left polarized light. This magnetic signal is proportional to the projection of the polarization vector $\vec{p}$ on the magnetization vector $\vec{M}$ [63, 118]:

$$A_{\mathrm{XMCD}} \propto \vec{p} \cdot \vec{M} \propto \cos(\angle(\vec{p}, \vec{M})) \tag{3.9}$$

By rotating the sample in a microscope around the surface normal, we can differentiate between in-plane and out-of-plane magnetized regions on the sample by using the Eq. 3.9. In the case of out-of-plane magnetization, the angle between magnetization vector and the photon vector remains constant and hence the XMCD is constant. In the case of in-plane magnetization, the angle between magnetization vector and the photon vector varies and hence the XMCD varies [41]. Fig. 3.10c shows the XMCD asymmetry image of a permalloy structure at the Fe-edge. It has a flux closure Landau-pattern, where the brighter domain is magnetized parallel to the photon polarization vector and the anti-parallel domain is darker. Both gray domains are magnetized perpendicular to the photon polarization vector, contributing nothing to the XMCD signal.

In this thesis, we have used mainly the XMCD-PEEM imaging technique as it is the only suitable and required for our single-pulse and also pump-probe measurements. We performed our experiments with SPECS P90 LEEM AC microscope, installed at Jülich beamline in BESSY II Berlin. The discussion on its LEEM mode is beyond the scope of this thesis. Therefore, we forward the interested readers to find all information on the LEEM measurements in the framework of Spin-reorientation transition in epitaxial Ni_x Pd_{1-x} films on Cu(001): a microscopic analysis by D. Gottlob [41].

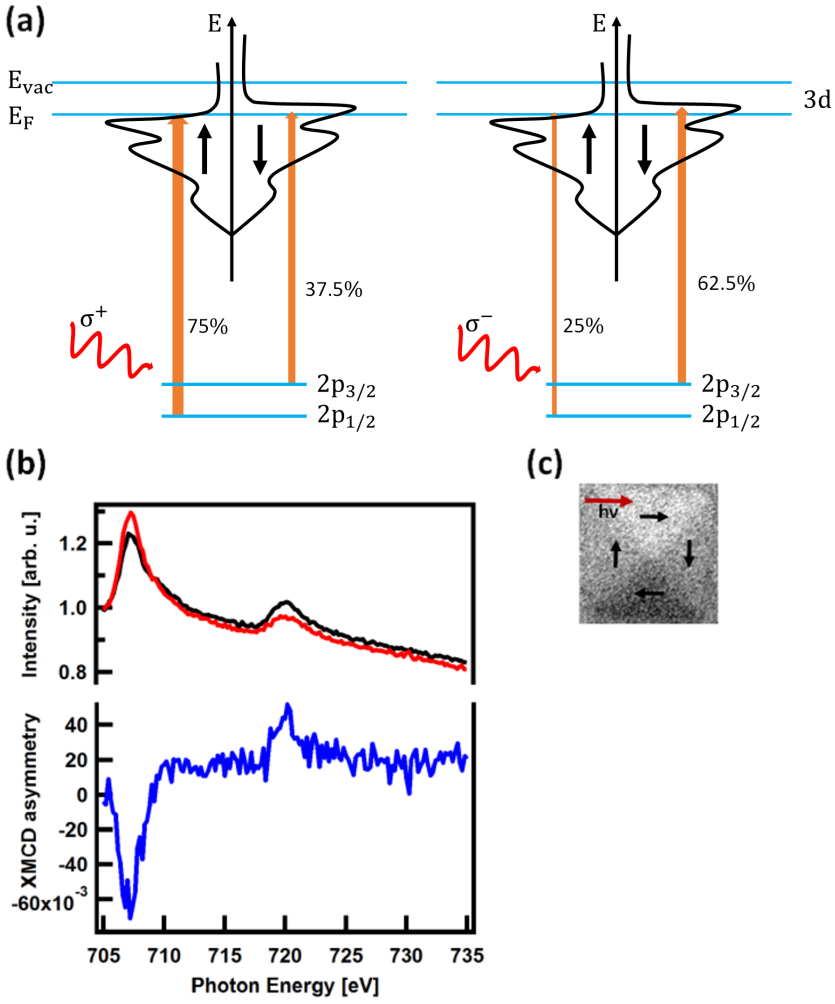

Figure 3.10: (a) Schematic diagram of XMCD effect in a single electron case that shows the transition between $2p$ and $3d$ levels. (b) Shows the X-ray absorption intensities along with XMCD effect. (c) Presents the flux-closure pattern, having bright dark and gray domains.

Chapter 4

Technical Developments for the XMCD-PEEM

In this chapter, we first present the design of the modified sample holder (see subsection 4.1.1), which has been used for executing the single-pulse and pump-probe measurements. The subsection 4.1.2 is devoted to the home-made pulse generator which has been used to study the single pulse induced magnetization changes in the $Ni_{20}Fe_{80}$ nanostructures. In section 4.2, we present the in-vacuum core-less coil technique, which has been used for magnetizing or demagnetizing the sample. The schematics for the single pulse and the pump-probe setups are presented in the section 4.3. Section 4.4 addresses a new negative gating concept, which was developed for the pump-probe setup in the SPECS aberration-corrected FE-LEEM-P90 instrument. F. Nickel et al. [96] had successfully demonstrated the positive deflection gating technique during the BESSY multi-bunch (MB) operation. The disadvantage of this operation was that approximately 80% of the usable electrons were lost at the contrast aperture while operating the positive gating technique. We replaced their concept with a negative gating technique and find only a loss of intensity up to 20%. We dedicate the section 4.4 to negative gating along with the first result of magnetization imaging. At the end, we discuss the challenges that we were confronted with during the project (section 4.5).

4.1 Current Injection System for XMCD-PEEM

In order to study the effect of spin-torque on domain patterns in ferromagnetic nanostructures, we had to integrate an appropriate current pulse injection system into the SPECS PEEM instrument. For this, we modified the SPECS sample holder [40] to make it compatible with the requirements. For the single-pulse experiments, we could switch off the high voltage (HV) of the PEEM each time and connect an external pulse-generator. For the pump probe, we had to integrate the in-situ current injection pulse setup, floating permanently at -6 kV in the XPEEM instrument. In the next subsections, we will discuss all our modifications to the XMCD-PEEM imaging setup.

Figure 4.1: Design of the SPECS sample holder along with the mounted cap. Adapted from [40].

4.1.1 Design of the Modified Sample Holder

Fig. 4.1 shows the design of the SPECS sample holder [40] along with the mounted cap. This sample holder is originally designed with two thermocouple pins for measuring the temperature and two filament pins for heating the sample and one is used for keeping the sample on HV up to -15 kV. Because we need no heating, our modified sample holder needs only two pins in the case of single pulse experiments, one is for keeping the sample on HV and the

second is for applying the pulses to the magnetic nanostructure. In the case of the pump-probe setup, a laser illuminating an avalanche photo-diode (APD) is used for injecting ns current pulses in to the nanostructure (see details in section 4.3.2).

Our modified sample holder along with the new sample chip-carrier is shown in Fig. 4.2. The sample is mounted in a small sample cap on the sample holder. The cap has a planar surface with a 3 mm hole at the center. As shown in Fig. 4.2b, a newly developed chip-carrier has three contact legs, two are made of thin needle pins and the third one is a tiny co-axial cable.

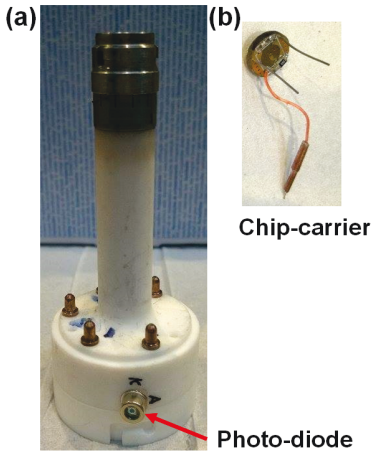

Figure 4.2: Modified sample holder along with new chip-carrier.

We connect the nanostructure in parallel to a SMD resistor (150 Ω), as seen in the electrical design of the modified sample holder in Fig. 4.3. The SMD resistor is used to sure damping of the reflected pulse. A thin Kapton foil is used to insulate between the sample and the cap. An APD (type S103510) is integrated at the back part of the holder. A pulsed laser-diode (635 nm, 100 mW) triggers the APD to generate short ($\sim$ 1 ns) current pulses. There is a buffer capacitor of 47 pF for the bias voltage noise reduction and peak current supply.

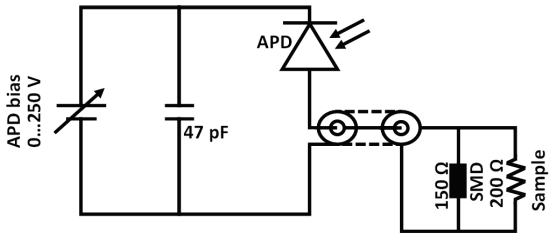

Figure 4.3: Electrical design of the sample holder, having an APD in series with the paralleled arrangement of a nanostructure (200 Ω) and the SMD resistor (150 Ω). A buffer capacitor of 47 pF is parallel to the APD for bias voltage noise reduction and peak current supply.

We glue the sample of size 5 mm $\times$ 5 mm with Carbon tape on top of the chip-carrier and use soldering to make a contact by Gold wire between the contacted pads of the nanostructure and the pins on the chip-carrier. These pins are further connected to the sample-holder pins by chip-carrier contact legs (see Fig.4.2b). The cap mounted on the chip-carrier should shield the wires from the field of the objective lens to avoid discharge inside the microscope. We introduced a screw-lever at the center of the sample holder. With the help of that, we press the chip-carrier with the nanostructure gently against the cap leaving almost no distance between the sample and the cap.

There are few drawbacks with handling and mounting of the sample on the sample-holder. We can mount only one nanostructure at one time because there is only one nanostructure on the sample substrate. Second, the nanostructure can easily break when we press it strongly against the cap via the screw-lever. A small electrostatic discharge can break the sample; therefore, one needs to wear a grounded ribbon while mounting the sample on the sample holder. Even frequent checking of a nanostructure by multimeter can destroy the nanostructure, therefore we restricted ourselves to check the resistance at the start and then after mounting the nanostructure on the sample holder. Moreover, despite all precautions, destruction of a sample frequently happened, so it was necessary to have more than one sample holder during the measurement. If unlucky one sample breaks during imaging then the second mounted sample would be

ready without wasting beam-time. Hence, we always tried to have two sample holders in the vacuum.

4.1.2 Schematic of the Home-made Pulse-generator

A new home-made pulse-generator for single-pulse experiment

For performing single-pulse experiments, H. Pfeifer (Senior Technician, PGI-6 FZJ) build a new pulse generator that allows generating voltage pulses up to a maximum amplitude of 22 V. Fig.4.4 depicts a schematic of the home-made pulse generator. It is triggered with 3 V by an Agilent 33250A pulse generator. This input voltage passes through the pulse forming-network with a 10 Ω resistor and a 850 pF capacitor. This pulse forming-network is used for driving an HF-preamplifier including a high-frequency transistor. This transistor switches a MOSFET-power amplifier. The MOSFET amplifies the output up to 22 V. The output of the MOSFET passes through a 50 Ω resistor in order to have an impedance matching to the outside coaxial cables towards the sample.

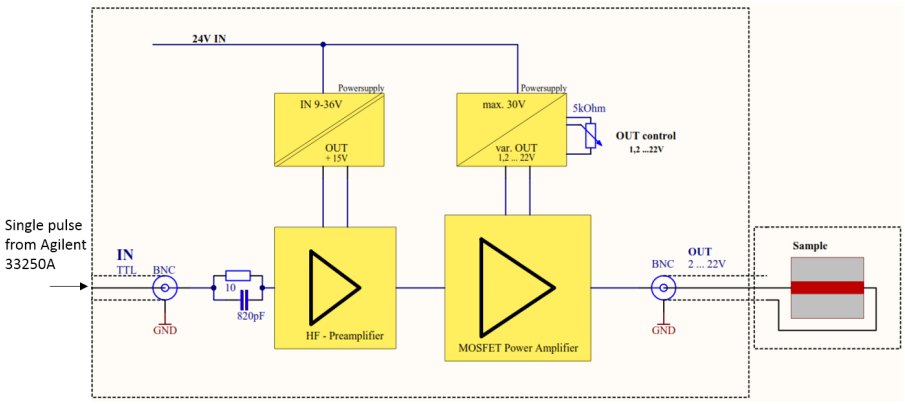

Figure 4.4: Schematic of the home-made pulse generator that gives output up to 22 V. (H. Pfeifer Courtesy)

We have two voltage controllers in the scheme. A fixed voltage-controller is used for the HF-preamplifier. The variable voltage controller is used for controlling the output pulse amplitude of the MOSFET-power amplifier. Further,

an inverter can be put just after the output of MOSFET-Power amplifier to get a negative pulse .i.e. -22V.

The shape of pulses of the home-made pulse generator

As we could not connect the oscilloscope probe inside the vacuum, we simulated the connection by similar wires and connectors outside and recorded pulses on an oscilloscope as shown in Fig. 4.5. For this measurement we had to reduce the amplitude to 40% and set to 9 ns width, resulting in at voltage pulse of 8 V at the output of the amplifier and of 5.15 V at the simulated "sample". Setting the amplifier to 100% we can obtain pulses of 22 V at the output and of 16 V at the sample (These pulses are not shown here). The pulse width can be varied from 9 ns up to 100 ns.

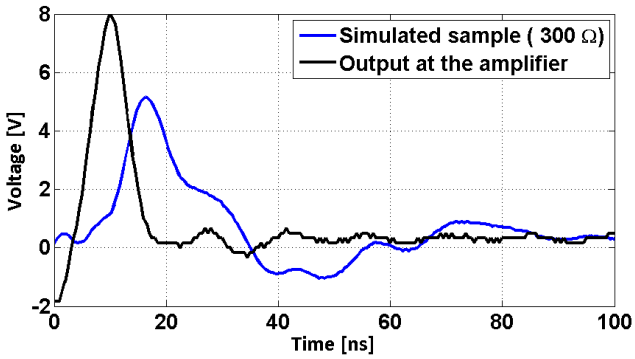

Figure 4.5: Shape of pulses obtained from home-made pulse generator set to 40 % of the maximum amplitude and 9 ns width at the sample, simulating the PEEM sample holder with similar wires/connectors.

4.2 In-Situ Magnetization / Demagnetization Coils Setup

To get a defined domain state, for example, a transverse wall (TW) or vortex wall (VW), we magnetize or demagnetize the sample in non-commercial in-vacuum core-less coils. In the case of demagnetization, a sample is placed inside

the core-less coils and then by decreasing an alternating current, the magnetic field is decreased from 26 mT to zero. As a result, we initialized a transverse wall at the bend of the V-shaped nanostructure and created a vortex wall at the right side of a half ring-shaped nanostructure, as shown in Fig.4.6a and 4.6b respectively.

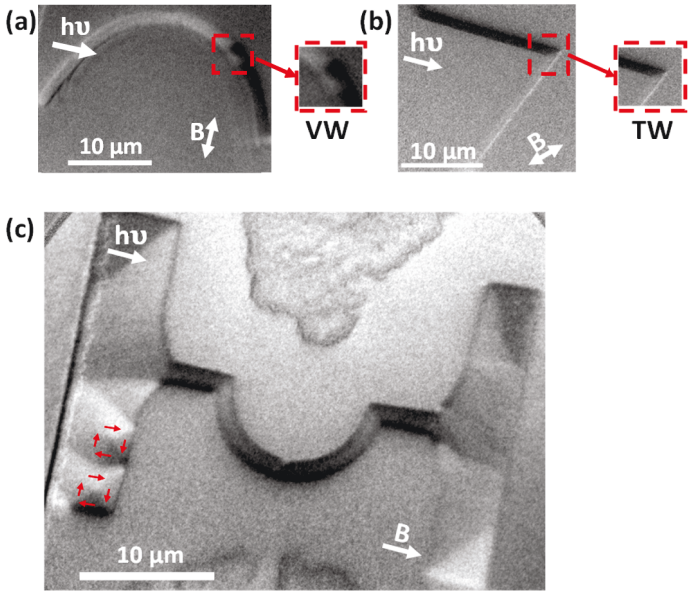

Figure 4.6: The domain images in (a) and (b) present the initialization of a vortex wall in a half-ring shaped and a transverse wall in a V-shaped nanostructure via an alternating magnetic field of 26 mT. (c) Notched half ring-shaped nanostructure which is magnetized by a 20 A DC current ($\sim$ 40 mT) along the longitudinal axis of the sample and initialized two Landau flux closure domain patterns at the left contacted pad of the sample.

In the case of magnetizing the sample, we apply 20 A DC current to the in-vacuum coils resulting in a quasi-static magnetic field up to 40 mT. Fig.4.6c depicts a notched half ring-shaped sample which is magnetized along the longitudinal axis of the sample and additionally formed two Landau flux closure domain patterns at the left contacted pad of the sample.

By comparing the XMCD images after rotating the sample around the surface normal, we can confirm an in-plane magnetization. For these structures, the images of the magnetization pattern change upon exposure to an external magnetic field, demonstrating that the domains in our prepared samples are fixed at the desired places, but are not too stable, so that external stimuli can alter them.

4.3 Setup for Single-pulse and Pump-probe Experiments

4.3.1 Setup for a Single-pulse Experiment

As we do not need to image during the pulse injection in single pulse experiment, we switched off the HV of PEEM each time and connect an external home-made pulse-generator to apply a single pulse to the sample (see Fig. 4.7).

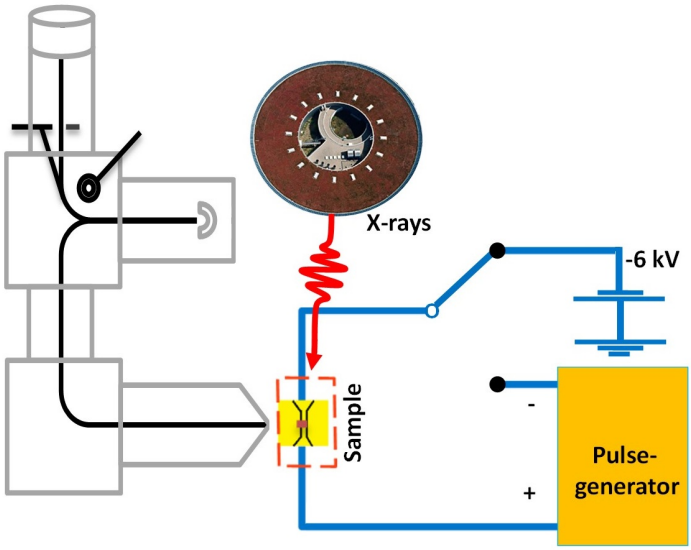

Figure 4.7: Schematic for a single pulse experiment

We were confronted with sparking effects while operating the PEEM at high voltage (HV $>$ -6 kV) which destroys the sample. Hence, we operated the microscope at -6 kV for all measurements.

After each subsequent pulse, we switched on the HV of the microscope and XMCD images were taken to observe magnetization changes. Differently from the pump-probe experiments, here we are only able to observe remanent changes of the magnetization. We present our single-pulse based experimental results in chapter 5.

4.3.2 Setup for a Pump-probe Experiment

The motive of pump-probe experiments is that the time in which a domain wall can be moved in a controlled way by spin transfer torque (STT) and the time in which it falls back (to a pinned state) will be determined presumably on a ns time scale.

In the pump-probe setup, a laser beam hitting the APD from outside the vacuum through a glass window generates ns current pulses up to $\sim$ 1 ns (see Fig. 4.8). An APD is connected to the backside of the sample-holder inside the vacuum chamber. The diode-laser pulse is synchronized with the BESSY bunch clock. The XMCD signal is then probed at different time delays before, during and after the current pulse in a stroboscopic mode with circularly polarized synchrotron radiation in the energy range of the Fe L_3-edge (707 eV).

Depending on the operation mode provided by BESSY II, the measurement is carried out by gating to the camshaft bunch (CB) in hybrid bunch mode or by synchronizing to the single bunch (SB) sequence (both at 1.25 MHz repetition frequency).

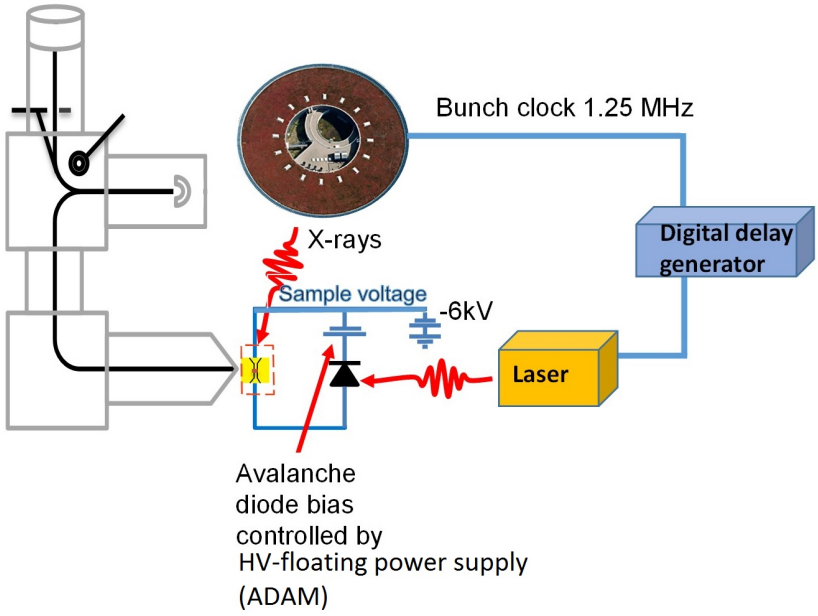

Figure 4.8: Schematic for a pump-probe experiment

4.4 Negative Deflection Gating Concept for a Time-resolving X-PEEM

A pump-probe approach is needed for the study of magnetization dynamics in time-resolved measurements. A single photon pulse emits a small number of photoelectrons which is not enough to visualize an image. Therefore, it is important to integrate the electrons over several seconds for taking a single image [63]. As the magnetic system is frequently excited during that time, it is necessary that the system has sufficient time to relax to the ground state between two subsequent images. The required relaxation time for the magnetic system is usually up to 20 ns which is much larger than the delay between two subsequent photon pulses i.e. 2 ns. Therefore, besides the 500 MHz multi-bunch (MB) mode, synchrotrons worldwide offer a few bunches mode, a single bunch (SB) mode or a camshaft bunch (CB) in the middle of multi-bunch gap as in

the available multi-bunch mode at BESSY II Berlin [62, 63]. Fig.4.9 shows a part of the timing bunch pattern by displaying bunch-current vs time. The total repetition period of the bunch pattern is 800 ns, of which the multi-bunches are repeated during 600 ns with a 2 ns temporal separation, and the camshaft bunch is placed in the middle of a 200 ns gap. The multi-bunches have an integrated current of 250 mA and the current of the available camshaft bunch is 4.5 mA. The single bunch (1 bunch/800 ns) weeks are much more favorable for pump-probe experiments as the single bunch current is 15 mA and there is no need of suppressing the signal of multi-bunches. Because single bunch weeks are rarely available and to make time-resolved experiments possible during a whole year, the deflection gating is introduced by us into the PEEM. Then, the camshaft bunch can be chosen for the pump-probe experiment while the signal of multi-bunches will be suppressed [96].

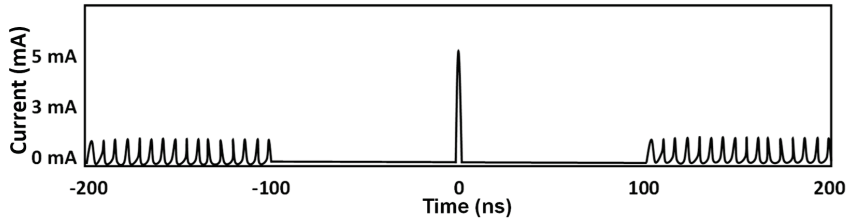

Figure 4.9: The graph shows a part of timing scheme of the bunch pattern by displaying bunch-current vs time. The total repetition period of bunch pattern is 800 ns, of which multi-bunch is repeated during 600 ns with 2 ns distance and there is a camshaft bunch in the middle.

In the previous experiments of our group, F. Nickel et al. had demonstrated the positive deflection gating technique during the MB operation. In that case, the electrons pass through the hole of a contrast aperture in the ON state and are lost at the plate in the OFF state. Please find a detailed study of this approach in the Ph.D. thesis of F. Nickel [97]. The disadvantage of their technique is that approximately 80% of electrons are lost during ON state. To avoid the loss due to the small size of the hole, we introduced the negative deflection gating pulse in a way that the maximum possible flux bypasses the front-edge of the contrast

aperture, losing only up to 20% of it (see Fig.4.10 for the schematic of the negative deflection gating). A contrast aperture is normally used to select a certain energy range of the electron distribution, but here we use it to suppress all electrons for a certain time, when the gating electrode is on a potential (-40 V) (see in Fig.4.10).

We are synchronizing our deflection pulse (see. Fig.4.11) by means of a Highland P400 digital delay generator and the bunch clock (see Fig.4.9) in such a way that the gating is in ON state during the hybrid bunch, i.e. X-rays are arriving at the sample. The correct adjustment of the deflection gating pulse is when it is coinciding with the camshaft bunch. In this case, only camshaft bunch electrons are bypassing the front-edge of the contrast aperture. When the deflection gating delay is largely increased or decreased, the image intensity increases very much due to the multi-bunches. This is how the correct timing can be found.

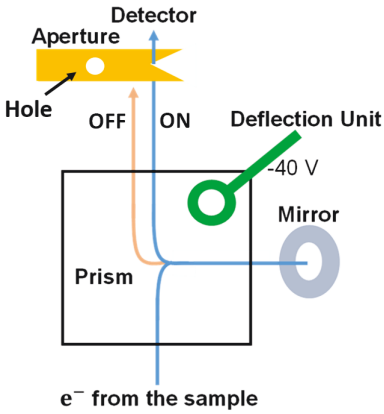

Figure 4.10: Schematic of the negative deflection gating setup, having electron trajectories at a contrast aperture both in the case of ON state (blue arrow) and OFF state (brown arrow). In case of the ON state only photoelectrons are bypassing the front-edge of a contrast aperture.

As shown in Fig.4.10, the gating electrode is placed diagonally into the prism,

without the need of any extra electron optics in the instrument or disturbing the energy filtered and aberration-corrected images [96]. The prism is used as a separator for the in and outgoing electron beams from the mirror for the PEEM. It has four sectors and each sector turns the electron beam path by an angle of 90 degrees. There is a real image in the center and a diffraction plane in the front and after each sector.

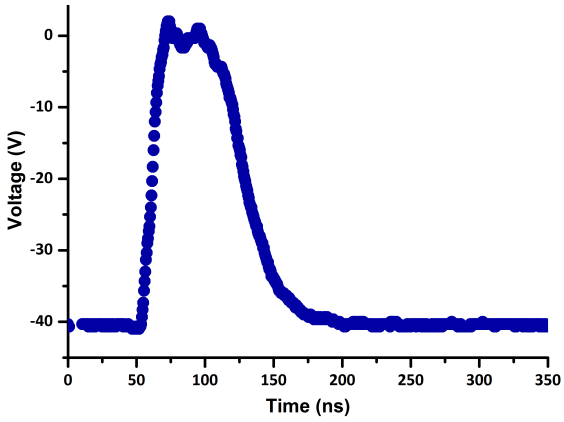

Figure 4.11: The graph of the negative gating pulse applied to the deflection electrode. It has a temporal width of 40-80 ns.

Here, we use a pulse amplitude of V_0=-40 V to achieve spatially separated electron trajectories in the OFF and ON state. This pulse is repeated after every 800 ns. We are observing the deflection of electrons in the diffraction plane at different voltages. In the beginning, we adjust the contrast aperture in such a way that the front edge is close to the e-beam without deflection voltage. When we apply the deflection voltage of V_0=-40 V, the electrons are moved behind the contrast aperture and no electron is available for the imaging. When we switch off the gating pulse, the electrons come back and start contributing to the imaging. In the time of deflection gating process, the deflection angle of electrons can be approximated as [96]:

$$\Delta\alpha \approx \frac{EL^2}{4V_0} \tag{4.1}$$

where α shows the displacement angle of the electrons. E and L present the strength and length of the electrostatic field. As V_0, being the drift energy of electrons in the microscope, is fixed, one can maximize the electron displacement either by enhancing the field strength E or by expanding its length L [27, 96].

Fig.4.12 illustrates the synchrotron bunch scheme along with the pump and gating pulses. The pump laser pulse arrives at the sample with a variable delay Δt with respect to the single-bunch. The multi-bunches (light blue) are suppressed by the gating setup, while only the camshaft bunch is used for the imaging (dark blue).

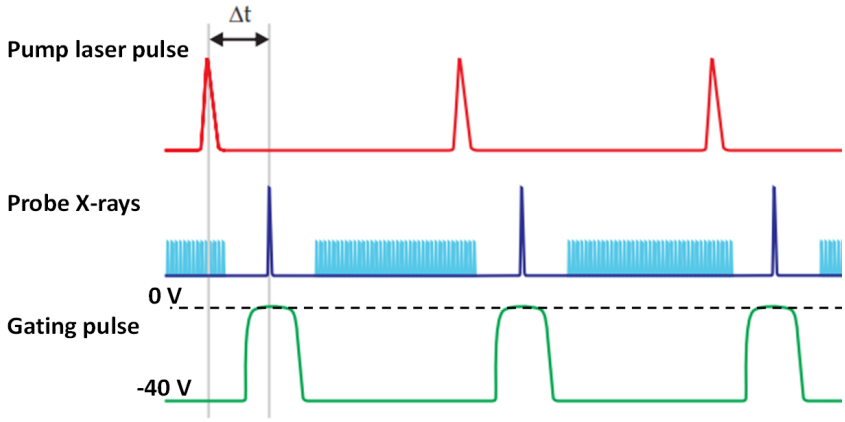

Figure 4.12: Synchrotron bunch scheme along with pump and gating pulses. The pump laser pulse arrives at the sample with a variable delay Δt with respect to the single bunch. The multi-bunches (light blue) were suppressed by the gating setup, while only the camshaft bunch is used for the imaging (dark blue). Adapted from [63]

First result with the negative gating setup

Adjusting the gating time window to the camshaft bunch of the hybrid bunch pattern, pump-probe measurements can be performed in a similar way as operating during the single-bunch mode.

A $Ni_{80}Fe_{20}$ sample of a 1 μm wide, 40 nm thick and 10 μm long half-ring shaped nanostructure was used. First, the magnetization of the nanostructure is initialized by an in-situ in-plane magnetic field. The direction of the applied field is marked by the white arrow in Fig.4.13a. The resulting magnetic structure has a flux-closure pattern, as illustrated by the red arrows in Fig.4.13a.

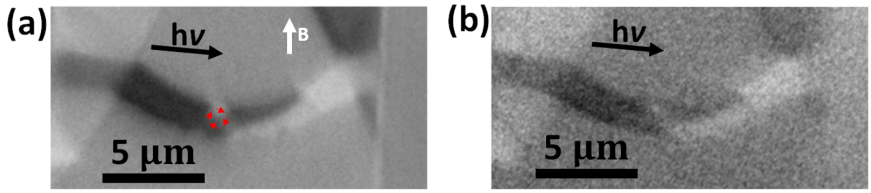

Figure 4.13: XMCD images of the $Ni_{80}Fe_{20}$ nanostructure collected at the Fe L_3-edge using the multi-bunch (acquisition time of 30 minutes) (a), and measuring it at the camshaft bunch of the hybrid bunch pattern with the new gating setup (acquisition time of 90 minutes)(b).

Fig.4.13 depicts the XMCD asymmetry images of the nanostructure. Fig.4.13a shows the XMCD image of the nanostructure while collecting it during the multi-bunch mode. The acquisition time was 30 minutes for this image. Next, the XMCD image is recorded again by gating to the camshaft bunch in the hybrid-bunch mode at 1.25 MHz repetition frequency. This image is collected with the acquisition time of 90 minutes. Both images contain similar information about the magnetic domain patterns even though multi-bunches have an integrated current of 250 mA and the current of camshaft bunch is 4.5 mA. This indicates that our new gating concept works successfully with reasonable intensity.

In summary, we have tested a new negative gating concept for pump-probe setup in the SPECS aberration-corrected FE-LEEM-P90 instrument. We got the larger intensity compared to the previous positive gating setup and fast switching by using the front-edge of the contrast aperture along with the negative pulse to the gating electrode. Because, the available camshaft bunch in the multi-bunch mode at the BESSY II synchrotron is only 4.5 mA, one needs to

measure up to eight hours to get a statistically good XMCD image and comparable with the image taken with multi-bunch in 30 minutes. On the other side, the available bunch current in the single bunch mode at BESSY II synchrotron is 15 mA, which is three times bigger than the camshaft bunch in the multi-bunch mode that makes it even more favorable for performing pump-probe measurement on our nanostructures.

4.5 Challenges During Project

Investigating of current induced domain wall motion into nanostructures is always very challenging. Here, we discuss a few challenges that we were confronted with during this work.

4.5.1 Preparation of the Sample

- Because transport measurements will be performed on the sample, one needs to have a nonconductive substrate. The best selection would be a non-doped GaAs substrate or a Si substrate having an extra SiO_2 layer deposited on top of it.
- Because the increase in temperature of the nanostructure happens while applying current pulses to it, one needs to have a substrate with good thermal conduction and GaAs substrate is a good candidate for this purpose.
- Next, one needs to do lift off twice during the fabrication of samples, one lift off is needed after $Ni_{20}Fe_{80}$ deposition and the second one is required after Gold sputtering. Each time, one makes sure that there are no residues of the resist on the sample. Such residues can cause charging in the PEEM while performing measurements. one.

4.5.2 Technical Problems

- Whenever we don't have a favorable domain structure in the sample, we magnetize the sample in the in-situ vacuum coils for getting favorable domain patterns in the nanostructure. During this process, we produce a

quasi-static magnetic field. Sometimes, this field unexpectedly breaks the sample. A few broken nanostructures due to the static magnetic field are shown in Figs.4.14a and b, where the red dotted lines show the original footprint of the nanostructure along with the contact pads.

- As mentioned earlier, the nanostructure heats up after applying a few pulses. The nanostructure already starts to lift off from the surface of the substrate and eventually breaks. As shown in Figs.4.14c and d, the remainders of the nanostructures left behind after lifting off from the substrates. The red dotted lines show the footprint of the V-type and half ring shaped nanostructures.

- We synchronize the pump with a probe signal in pump-probe mode. For this, the available camshaft bunch in the multi bunch mode at BESSY II synchrotron is much weaker (4.5 mA) so that one needs to measure up to eight hours to get a statistically good image on the samples. As longer measurement time induces higher probabilities of an event like a discharge, this mode seems less favorable than the single bunch mode at BESSY II synchrotron with 15 mA.

4.5.3 Handling of the Sample

- Nanostructures are very sensitive to electrical discharge. To counter this problem, one ought to wear an electrical discharge ribbon while cutting the sample, doing lift off process, mounting the sample on the chip carrier and also it is important during the transfer of the sample from load lock up to the main chamber of the microscope to keep all parts connected to ground and clear from electrostatic charge.

- Next, the sample can easily be damaged by electrostatic discharge that can happen anytime. One reason may be a bad pressure in the chamber in combination with the high voltage (HV) of a microscope. Second, sparking can happen if any dust particles or residuals of the resist on the surface of the sample come in front of the objective lens. Therefore, it is necessary to blow the surface of the sample with a Nitrogen gun after mounting

it on the chip carrier. Note that the contacted wires and silver paste on the mounted nanostructure should not be visible to the high voltage of a microscope, as this can easily lead to a spark while placing the sample in front of the objective lens. In addition, the nanostructure can be damaged due to the stray field of the objective lens if it is at a smaller distance from it. The top of the cap also needs proper cleaning and a flat surface to avoid any discharging (sparking) effect. Figs.4.14e and f depict the samples which are completely blown off by the sparking effect.

- One needs to be very gentle while pushing the cap on the mounted sample. Any irregular force can destroy the nanostructure.

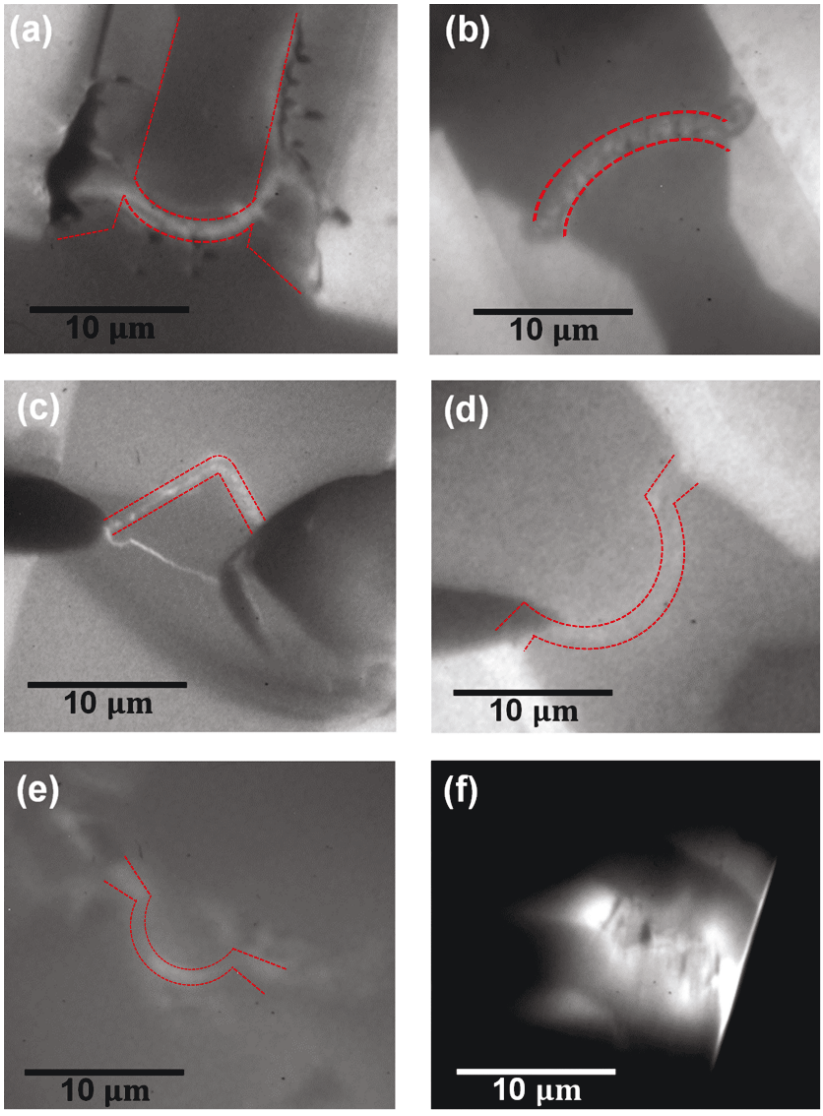

Figure 4.14: Images of broken nanostructures with reasons of the failure. (a)-(b) Samples which were damaged by the static magnetic field. The red dotted lines show the footprint of the nanostructures, the half circle itself is not present any more in b) and d). (c)-(d) Damaged samples due to the current pulse where the remainders of the nanostructures are represented by the red dotted lines. (e)-(f) Broken samples due to the spark discharges between the sample and the objective lens. Like in f), in many cases the spark was so strong that one cannot see where the structure was.

Chapter 5

Single Pulse Induced Magnetization Changes in $Ni_{20}Fe_{80}$ Nanostructures

In this chapter, we present our experimental results on the reaction of magnetic domains and domain walls upon a single current pulse. As it turned out to be difficult to manipulate the magnetic textures at all by a pulse of high current density without thermally destroying the sample, we approached working experimental conditions with three different types of samples: A simple ring-shaped nanostructure of 1 μm width (see section 5.2), a V-shaped structure of 700 nm width containing a transverse wall (TW) at the bend (see section 5.3), and a 1μm half ring-shaped nanostructure with a notch in the middle, possibly acting as a pinning center (see section 5.4). In this chapter, we have used the $Ni_{20}Fe_{80}$ alloy, different in stoichiometry from $Ni_{80}Fe_{20}$ (so-called Permalloy), for studying the domain wall motion (see section 3.2 for comparison between the properties of both NiFe alloys).

In order to obtain a defined initial state with well visible domains and domain walls (DW) to be manipulated by our current pulses, an in-situ static magnetic field was applied perpendicular to the ring-shaped or V-shaped nanostructures. In optimal cases, this resulted in opposite magnetization on the left part and the right part, respectively, and a domain wall in between. Besides the influence of the current pulses on these existing domains, it turned out in all samples that the high current pulses created new multiple domains, like diamond patterns in the half ring-shaped nanostructure and an array of domains

in the V-shaped structure (see subsection5.3.2). This phenomenon we will try to explain as an effect of temperature increase during the applied pulse in combination with the spin transfer torque (STT).

5.1 Determination of Domain Magnetization from XMCD Images Demonstrated at a Simple Flux-Closure Landau-Pattern

In the discussion of the XMCD asymmetry as a contrast mechanism in section 3.3.4, we showed that the asymmetry A_{XMCD} depends on the angle between the light polarization vector $\vec{p}$ and the magnetization vector $\vec{M}$ [63, 118]:

$$A_{\mathrm{XMCD}} \propto \vec{p} \cdot \vec{M} \propto \cos(\angle(\vec{p}, \vec{M})) \tag{5.1}$$

This equation predicts that a maximum dark (bright) XMCD asymmetry will appear in a XMCD image when the magnetization $\vec{M}$ is anti-parallel (parallel) to the polarization direction $\vec{p}$.

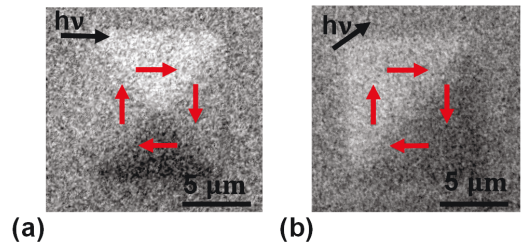

Figure 5.1: (a) XMCD image of a Landau flux-closure pattern, having bright, dark and gray domains. It was measured when the photon vector pointed along one of its sides. (b) XMCD image collected with the photon incidence angle, different by 45° from the angle of (a). The red arrows depict the magnetization direction in the flux closure domain patterns. Both XMCD images were collected at the Fe-edge with a photon energy of 707 eV (the maximum XMCD energy).

As it will be difficult for complex domain patterns to understand the exact

magnetization structure from the XMCD images, we first demonstrate here our method at the well established example of a Landau pattern in a 10×10 μm^2 square-shaped $Ni_{20}Fe_{80}$ structure. Images were taken at two different photon incidence angles, as seen in Fig. 5.1. The XMCD image in Fig. 5.1a was taken when the photon incidence is directed along one of its sides. Here, we define this photon incidence vector as a 0°.

In this configuration, the bright domain is magnetized parallel to the photon polarization vector and the anti-parallel domain is dark. Both gray domains are magnetized perpendicular to the photon polarization vector. The magnetization directions of the latter two domains, being up or down, cannot be unambiguously determined by only this image, without additional information. With our knowledge that the flux closure domain patterns are energetically favorable, we can determine the magnetization direction of the gray domains with only one angle of the XMCD image, but in general, a second image at different photon incidence angle needs to be recorded for understanding a more complicated structure. In this example, we recorded another XMCD image with the photon incidence angle, different by 45° from the angle of Fig.5.1a, as seen in Fig.5.1b. In Fig.5.1b, both left-gray and up-brighter domains of Fig. 5.1a appear as one brighter diagonal stripe at this angle. Similarly, the right-gray and dark domains, in Fig. 5.1a, appear as one darker diagonal stripe. Here, the flux closure domain pattern appears in diagonal stripes of only two colors, although there are 4 domains with different magnetization directions. This, we should remember when interpreting more complicated spin configurations in section 5.2.

5.2 Nucleation, Elongation, Propagation and Transformation of Diamond Patterns in $Ni_{20}Fe_{80}$ Nanostructure by a High Current Pulse

In this single-pulse experiment, we report the interaction of current pulses with the magnetization textures inside a 40 nm thick, 1 μm wide and 12 μm long

$Ni_{20}Fe_{80}$ half-ring shaped nanostructure. It has an Ohmic resistance of 230 Ω. The nanostructure pattern was defined on a GaAs substrate by electron-beam lithography. We introduced Gold contact pads at both ends of the nanostructure via photo-lithography (see section 3.1 for sample design and fabrication steps).

5.2.1 Nucleation of Diamond Pattern by a High Current Pulse

Fig.5.2 depicts initial steps involved in the nucleation of multiple domains in the nanostructure. All injected pulses were of width 100 ns (see subsection 4.1.2). Fig.5.2a shows an XPEEM image of the ground state of a nanostructure, having a long domain texture. This texture is more gray on the left side and less gray on the right side of a half-ring due to the varying angle between magnetization and photon incidence angle. In such a soft material based nanostructure, the shape anisotropy prefers a magnetization along the nanostructure and the exchange energy prefers parallel magnetization in the structure. The magnetization state resulting from both interactions is a mono-domain along the nanostructure. However, this is a high-energy state which can reduce its energy by splitting up the single domain into multiple domains upon external stimuli [64].

Starting from the state shown in Fig.5.2a, the applied high single pulse of 9.7×10^{11} A/m^2 inverted the magnetization in the direction of electron flow, as seen in Fig.5.2b. Next, we injected a single pulse of magnitude 8.7×10^{11} A/m^2 which acts on a single domain of the nanostructure and collapsing it into multiple domains as seen in Fig.5.2c. Splitting up of the single domain into multiple domains occurs when the applied pulse is greater than the threshold current density. The creation of multiple domains due to a high pulse will be explained in detail in subsection 5.2.5.

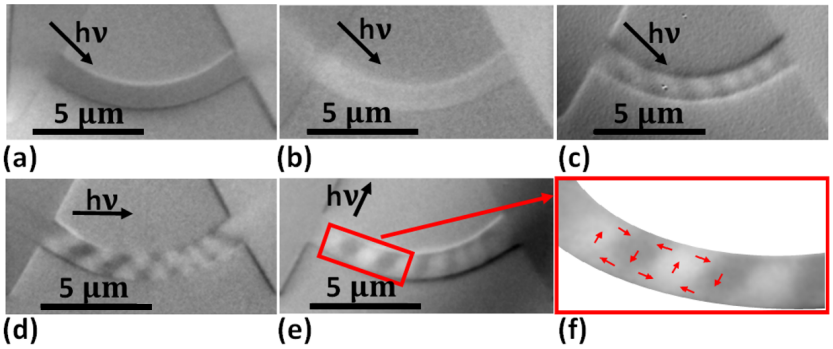

Figure 5.2: (a) Ground state of the nanostructure. (b) XMCD image after single 100 ns long current pulse with a current density of 9.7×10^{11} A/m^2; $\vec{M}$ inverted to the right. (c) Shows diagonal stripes from left-top to the bottom right after second applied pulse with a current density of 8.7×10^{11} A/m^2. The (d) and (e) depict XMCD images, different from Fig.5.2c by 45° and 90°, respectively. The diagonal stripes in Fig.5.2d appear from left-bottom to right-top and more radial to the half-ring shaped nanostructure in Fig.5.2e. (f) Zoom-in of flux closure domain patterns of (e), showing that the two outer flux closure domain patterns have the same sense of clockwise rotation and the middle flux closure pattern has an anti-clockwise. The red arrows indicate the magnetization direction.

In Fig.5.2c, the multiple domains in the nanostructure appear as diagonal stripes from left-top to bottom right. The magnetization direction of the stripe domains cannot be unambiguously interpreted by only one angle of the XMCD image. Therefore, we recorded XMCD images, different by 45° and 90° from Fig.5.2c, as seen in Figs.5.2d and 5.2e respectively. We found that the stripes in Fig.5.2d appear as a diagonal from left-bottom to right-top and seem radial to the half-ring shaped nanostructure in Fig.5.2e.

Here we tentatively interpret that the stripe domains in Figs. 5.2d and 5.2e are Landau-like flux-closure domain patterns, appearing differently in both figures. To determine if the character of these flux-closure patterns are more Landau-like or more vortex-like, we will carry out circle and curved-line scan profiles on them in subsection 5.2.3. In a Landau-like configuration, the magnetization

lies in the plane of a square and rotates out of the plane in the center to generate the vortex core, as shown in Fig.5.1. In a vortex-like state, the magnetization is oriented circumferentially in-plane along with an out-of-plane vortex core at the center [58].

For now, let us assume that the flux-closure domain patterns are Landau-like and each has 4 triangular shaped domains. The flux-closure domain patterns are well-defined on the left-hand side of the nanostructure, but on the right-hand side the distance between the stripes becomes smaller. Differently from the domains on the left side, which look like flux-closure patterns in their ground state, in these right-hand side flux closure domains, the right and left triangular shaped domains become smaller in size than the up and down domains. Moreover, these flux closure domain patterns seem to have a lower contrast, which will be attributed in subsection 5.2.3 to their smaller size, compared to the image resolution.

Zooming into one of the flux-closure domain patterns at the left-hand side of the half ring in Fig.5.2e shows that the right and the left flux closure domain patterns have clockwise sense of rotation and the middle flux closure domain pattern has an anti-clockwise (see Fig.5.2f). Such combination of flux-closure domain patterns defines so-called double diamond states [84].

Our physical interpretation of what happened in Figs. 5.2a-e is as follows. After injecting the first high pulse of magnitude 9.7×10^{11} A/m^2, $\vec{\mathrm{M}}$ inverted to the right in the direction of the electron flow, as seen in Fig.5.2b. This is attributed to the effect of the STT on the magnetization. Here, we have to take into account that in all our samples, we observe large stable domains on the contact pads, as seen in Fig. 4.6c. In this case, there seems to be a bright domain i.e. magnetized from left to right (only visible as a brighter gray on the left side of Fig.5.2a). The applied current becomes spin-polarized due to the spin dependent band structure while passing through this stable domain and makes changes in the magnetization of the nanostructure region. When we applied the second pulse of magnitude 8.7×10^{11} A/m^2 (see Fig.5.2c), the magnetic texture

is divided into multiple domains even though the excitation is smaller than the first pulse. It seems that in this step, besides the STT, temperature could play a larger role for the higher pulse. On the other hand, L. Heyne et al. [46] reported that a single vortex wall split into two parts in $Ni_{80}Fe_{20}$ half ring-shaped structure when the STT acted on it and M. Kläui et al. observed the nucleation and annihilation of magnetic vortices in $Ni_{80}Fe_{20}$ wires due to STT [70], neglecting temperature effects. In contrast, Yamaguchi et al. [146] observed an increase in sample temperature up to the Curie temperature of $Ni_{80}Fe_{20}$ due to a high current pulse into the nanostripes and claimed that a single domain structure splits into multiple domain structures due to temperature increase. In our case, we observe so many domains in the $Ni_{20}Fe_{80}$ (different in composition from $Ni_{80}Fe_{20}$) half-ring shaped nanostructure after the second pulse, that rather than nucleation due to STT, a temperature rise near to or above the Curie temperature ($\sim$ 860 K) seems to be at least the dominant process. There could be several reasons responsible for this unexpected magnetic domain patterns. First, thermal stress on the sample that may result from magnetostriction after temperature rise. This effect would considerably occur for samples made from $Ni_{20}Fe_{80}$, having a larger magnetostriction (see table 3.1). The second reason could be an interfacial strain due to material-substrate mismatch of thermal expansion coefficients and the temperature difference between material and a substrate used [18].

After the absence of any magnetic order in the hot state of a nanostructure, during the cool-down, a reordering occurs like it is in ferromagnets. In this case the magnetization orders into flux closure patterns, on the left side with pretty regular shapes. The fact that the domains on the right side are narrower and look like being compressed, is probably due to the STT being present during this process.

Why didn't the temperature increase in the same way already at the first pulse (see Fig. 5.2b)? The most plausible explanation is that upon the first high pulse, the nanostructure got some structural changes and hence enhanced resistance R and also reduced thermal contact to the substrate could be the result.

This is something observed on all samples after injecting each subsequent pulse. Due to these reasons, the second pulse may increase the temperature more than the first pulse ($P \propto R$).

Our interpretation is in agreement with the previous theoretical literature [148, 149] and experimental findings of references [146, 147] where it turned out that such a high current density pulse increases the temperature of the nano-structure up to the Curie temperature of the soft material used and consequently, a single domain splits into multiple domains. We will try to estimate the increase in temperature of a nanostructure due to a high pulse in detail in subsection 5.2.5.

5.2.2 Propagation and Transformation of Flux-closure Domain (Double Diamond) Patterns

After we observed flux closure domain patterns in the half-ring, several consecutive current pulses were injected (see Fig.5.3). XMCD images that have been taken after each current pulse were compiled in two separate columns, as seen in Fig.5.3. The column of images (a-d) was taken, with photon incidence angle, different by 45° from the column of images (e-h).

After the first pulse of current density 7.6×10^{11} A/m^2, the flux closure domain patterns, on the left-hand side of the half ring, slightly moved in the direction of electron flow, but the flux closure domain patterns on the right-hand side remained unchanged as seen in Figs.5.3b and f. Blue line on Fig.5.3a-d marks the trajectory of the core in flux closure domain patterns. The red arrows depict the magnetization direction in each flux closure domain pattern. They were deduced from the comparison of the two illumination angles, following the scheme explained in section 5.1.

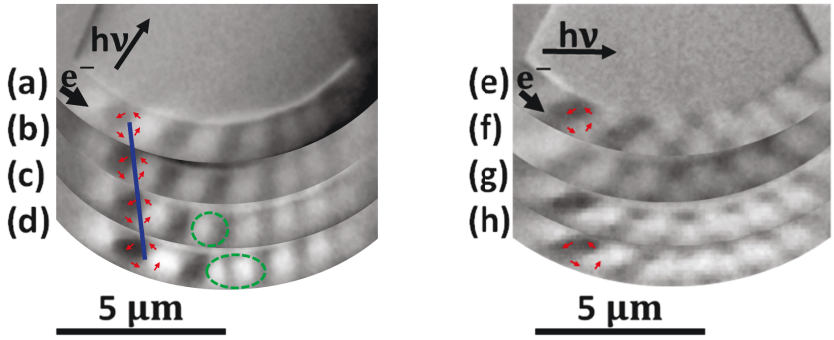

Figure 5.3: XMCD images of the half-ring shaped nanostructure. The column of XMCD images (a-d) collected, with a photon incidence angle, different by 45° from the column of XMCD images (e-h). Blue line on Fig.5.3a-d marks the trajectory of the core in flux closure domain patterns. The green circle in XMCD image (c) marks the central flux closure domain pattern and the green ellipse in (d) depicts the splitting up of this pattern into two parts. The red arrows point the magnetization direction in the flux closure domain pattern.

After the second single pulse of the same magnitude 7.6×10^{11} A/m^2, we again notice a small movement of the flux closure domain patterns in the electron flow direction (see Fig.5.3c and g). After that, we applied two more consecutive pulses of the same magnitude (7.6×10^{11} A/m^2), but the flux closure domain patterns stayed unaltered. This might be due to a pinning effect.

Because of no further movement, we injected a pulse of high current density 9.0×10^{11} A/m^2. The flux closure domain patterns moved and also elongated significantly in the direction of electron flow. We noticed that the first and third flux closure domain patterns moved up to 150 nm and 475 nm, respectively. We will present a schematic plot on this motion of the flux closure domain patterns in subsection 5.2.3.

A closer inspection of one of the flux closure domain patterns in Fig.5.3e (see red arrows on the flux closure pattern) and following the same flux closure domain pattern in 5.3a-d, revealed that the flux closure domain pattern had the

same magnetic contrast, but appearing differently at different angles.

While there is a clear indication of temperature effects on the magnetization texture of the nanostructure at the first pulses in section 5.2.1, here it is important to note that the flux closure domain patterns move due to the STT as the motion happens in the direction of electron flow (see section 2.5), possibly assisted by the increase in temperature.

5.2.3 Information on the Structure of the Flux-closure Patterns

To further study the flux closure domain patterns on the left-hand side of the nanostructure, we carried out a circular path intensity scan around one of them. We executed the circular path intensity scan in Fig.5.4a in such a way that the circular scanning started from the gray domain which was labeled by 1 in the zoom-in Fig.5.4b. The numbers from 1 to 4, if it is a Landau flux closure pattern, would indicate four triangular domains in the flux closure domain pattern. Fig.5.4c depicts the profile of the circular scan where the labels 1 to 4 present the footprint of each domain. The scanned profile appears as trapezoid shaped steps, best seen at labels 2 and 4 in Fig.5.4c. The maximum value at label 2 and a minimum value at label 4 stand for XMCD-intensity of a domain with local magnetization parallel and antiparallel to the photon polarization vector, respectively.

We have made a fit of the scanned intensity profile with a sine function, which would be obtained for vortex structure, as shown in Fig.5.4c. A Landau pattern on the other hand would result in perfect square type profile [94, 117]. Both function do not reproduce our experimental curve. Instead, the positive and negative peak at 90 and 270 degrees respectively, are narrower compared to the sinusoidal function, probably due to the confined boundary conditions in our one-micrometer wide nanostructure. We have constructed a cartoon of the magnetization profile from Fig.5.4c and depicted in Fig.5.4d. This shows that the shape of the closure domain pattern appeared distorted at the labels 1 and 3 domains.

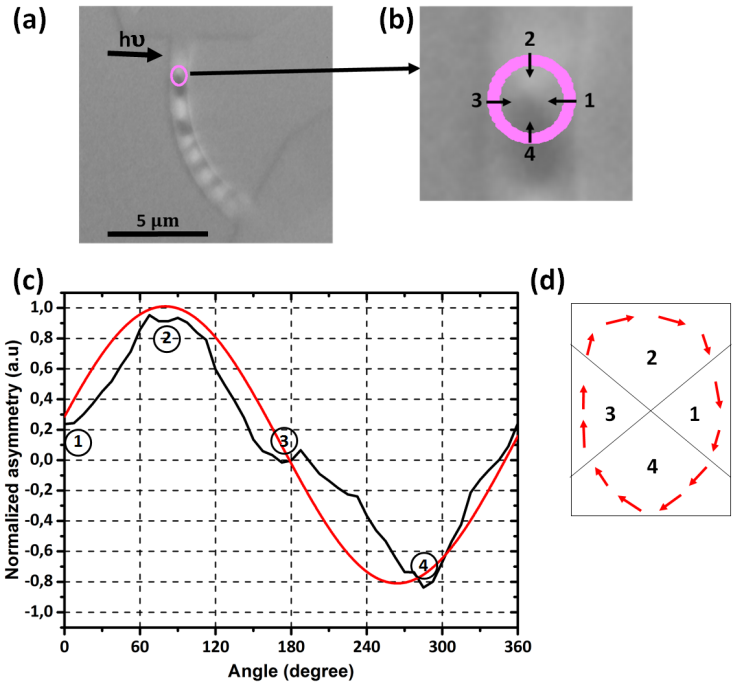

Figure 5.4: (a) XMCD image of the nanostructure where the pink circle shows the circular intensity scan path. (b) Zoom in the circular-scanned flux closure domain pattern with sectors 1-4. (c) Intensity profile of the circular scan. The red curve is a sinusoidal fit to the intensity profile. (d) Magnetization profile constructed from (c).

Next, we are interested to compare the character of the right-hand side flux closure domain patterns with the expanded flux closure domain patterns on the left-hand side of the half ring by executing the circular-line intensity scans through the whole half-ring. The scans revealed information on the motion of left-hand side expanded flux closure domain patterns along with the right-hand side flux closure patterns, as explained in the next paragraphs.

To analyze flux closure domain patterns on the half ring, circular-line scans were carried out on the XMCD images of Figs.5.5a and 5.5c. We marked three

particular flux closure domain patterns in Fig.5.5a by labels A, B, and C. The XMCD image of Fig.5.5c was obtained after passing a few more current pulses through the half ring as discussed in subsection 5.2.2.

Fig.5.5b and Fig.5.5d depict the resulting scan profiles of Figs.5.5a and 5.5c, respectively. A closer inspection of both circular-line scans reveal that the left-hand side flux closure domain patterns had a larger XMCD amplitude than the right-hand side flux closure domain patterns. This difference can be understood because the distance between the flux-closure domain patterns on the right hand-side are smaller and they could not follow the STT as much as the left side flux closure domain patterns, due to a big stable domain acting as a barrier at the right-hand side contact pad of the sample. The limited resolution of the PEEM cannot be the reason of the lower amplitude as it is 120 nm and thus small compared to the size of even the right-hand side domain stripes (see Figs.5.5b and 5.5d).

Second, a significant motion of the right-hand side flux closure domain patterns in the direction of conduction electrons was observed. As an example, the A and B flux closure domain patterns moved up to 150 nm and 475 nm, respectively. The green lines in Figs. 5.5c and 5.5d indicate the motion of flux-closure domain patterns.

Here, we found that a big change in the configuration of a half-ring, namely the splitting of the C flux closure domain pattern into two, appeared. First, the flux closure domain pattern C moved up to 630 nm and divided into two afterwards. This is probably due to pinning site near the flux closure domain pattern C. In the first place, the flux closure domain pattern stretched, which consequently imports an extra domain wall energy into the system. When this increased energy exceeds the energy needed for the core nucleation, the stretched flux closure domain pattern is favorably transformed into two flux closure domain patterns [46]. In addition, we observed that the first part of the split flux closure domain pattern is not fully resolved with the PEEM, probably due to the confined boundary conditions in the nanostructure (see Fig. 5.5c). A splitting

of flux closure domain pattern into two parts was also reported by L. Heyne et al. [46].

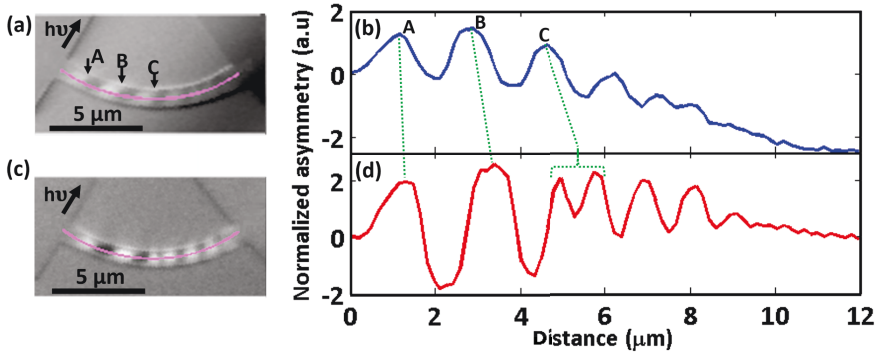

Figure 5.5: (a) XMCD image of the nanostructure having flux-closure patterns on the left-hand side and flux closure patterns on the right-hand side, where the distance between the stripes becomes smaller (from Fig.5.3a). The labels A, B, and C indicate particular flux closure domain patterns on the nanostructure. The pink curved-line along the half ring presents the scanning path. (b) Curved-line scan profile of (a), visualizing the initial positions of the flux closure domain patterns. The downwards trend of the whole curve is an artifact due to a beam-shift. (c) XMCD image of the same nanostructure after a few applied pulses. The pink curved-line along the nanostructure displays the scanning path (from Fig.5.3d). (d) Curved-line scanning profile of (c), visualizing the displacement and the transformation of the flux closure domain patterns. The green lines describe the motion of flux closure domain patterns. The variation from left to right, of the angle between **M** and the photon incidence, was taken into account in the normalization.

5.2.4 The Pulse Profile

At this point, as we saw that both STT and Joule heating affect the magnetic structure, we should try to have a closer look on shape and amplitude of our

electric pulse. First, we have to know the magnitude of a voltage for required current density. Second, this is useful to be able to estimate the energy deposited in the nanostructure by one pulse, and third, because not only the flux density but also the rise time can be important according to the reference [46]. Even the fall time could be important, if the current amplitude falls later then the sample cools down below Curie temperature, so that reordering can still be influenced by the STT.

As mentioned in 4.1.2 we used an in-house built pulse generator with a maximum pulse height of 22 V and an adjustable pulse length of 9 - 100 ns. In the previously shown experiments we used always 100 ns, but here we show the pulse shape with the time set to 9 ns, as we saw that rise time and fall time remain almost unchanged, only the time the potential remains on the peak value changes.

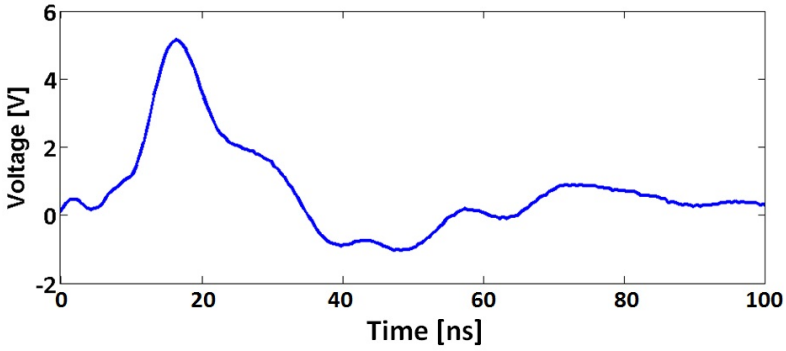

Figure 5.6: Pulse shape of a home-made pulse generator set to 9 ns width, and V_{max}= 5.15 V, recorded on an oscilloscope.

On the way from the pulse generator to the sample, the pulse has to pass a high voltage vacuum feed-through, non-coaxial wires in the vacuum and leads in the ceramic which are also not HF-optimized. Hence we expect damping, reflection and "ringing". Of relevance is of course not what comes out from the pulse generator, but in which shape the pulse arrives at the sample. As we could not connect the oscilloscope probe inside the vacuum, we simulated the

connection by similar wires and connectors outside and the result is shown in Fig.5.6, for a pulse height of 5.15 V adjusted at the pulse generator.

Left and right from the peak value we see rise and fall times of less than 10 ns. Thus, during this peak the deposited power and Joule heat is rather low. But the longer in time the peak value is sustained, the more heating becomes relevant and thus it can happen at specific pulse lengths that the tailing edge falls into the cool down.

5.2.5 Temperature Effect via a High Current Density

Breaking up of the single domain into multiple domains happens when the applied current density becomes greater than the critical current density (in our case; J= 8.7 $\times$ 10^{11} A/m^2 > J^{cric}=7.6 $\times$ 10^{11} A/m^2)[146, 147, 148, 149]. This high pulse increases the temperature of the nanostructure. This temperature assists the STT by decreasing the energy barrier for the domain wall nucleation and consequently splitting the single domain into multiple domains afterwards. In a nanostructure, the magnetization is constantly along the long axis in a single domain case, to decrease the demagnetization field and lower the total energy of a system. However, in the case of a multiple domain, the magnetization at the edges has a tendency to be parallel to the edge to avoid free magnetic poles for minimizing the magnetostatic energy [22].

When the current pulse flows into a structure its temperature increases due to the Joule heating effect. It is important to know how much the temperature of the structure increases. For this, we have followed the analytic model of You et al. [148, 149] which they have provided to approximate the increase in temperature of the heated nanostructure as a function of current density and time t [33]. They made the following assumptions for the model. (i) the substrate thickness is larger than the nanostructure length, (ii) whole nanostructure is at same temperature, (iii) the temperature of both nanostructure and interface are the same, (iv) For the substrate, the heat source is at the interface, (iv) because of the small surface area of the nanostructure, the effect of convection is ignored

in the model, (v) the heat capacity of the nanostructure is neglected because it overestimates the increase in the temperature, (vi) we assume heat dissipation into the substrate only. With above assumptions, they have provided the following equation [33, 80, 148]:

$$\Delta T = \frac{whJ^2}{\pi k\sigma} \operatorname{arc\,sinh}\left(\frac{2\sqrt{tk/\rho C}}{0.5w}\right) \tag{5.2}$$

where w, h and σ are width, height and conductivity of a structure respectively. The J is the current density applied to the structure. The quantities k, ρ, and C are the thermal conductivity, mass density, and specific heat capacity of the substrate used [33]. By using the analytical expression of equation 5.2, our estimated ΔT is 548 K for a pulse length of 100 ns. For this, we used $w = 10^{-6}\mathrm{m}$, $h = 40 \times 10^{-9}\mathrm{m}$ and $\sigma = 2.9 \times 10^{6}(\Omega\mathrm{m})^{-1}$ of our $Ni_{20}Fe_{80}$ structure. Furthermore, we put $J = 9.7 \times 10^{11}\mathrm{A/m^2}$ and t = 100 ns used. The values of k = 45 $\mathrm{W/mK}$, ρ = 5317 $\mathrm{kg/m^3}$, and C = 350 $\mathrm{J/kgK}$ of the GaAs substrate are used. This shows that the actual temperature of a structure may increase up to the Curie temperature of the $Ni_{20}Fe_{80}$ ($\sim$ 860 K). The value of the increase in temperature in this work is comparatively close to the reference [147]. In that reference, Yoon et al. estimated the increase in temperature of 500 K for a current density of 5.5 $\times$ 10^{11} $\mathrm{A/m^2}$ while flowing it through a 600 nm wide $Ni_{80}Fe_{20}$ structure.

5.3 Current Interaction with Transverse Wall in V-shaped $Ni_{20}Fe_{80}$ Nanostructure

Here, we present the interaction of a current pulse with a transverse wall (TW) motion which we obtained in Ni_{20} Fe_{80} V-shaped nanostructure being 25 μm long, 700 nm wide and 40 nm thick. Sample fabrication and the experimental setup is the same like that of the sample in section 5.2. The XMCD images have been recorded before and after each injected 100 ns long single pulse for studying the motion of the transverse wall or any other change in magnetization textures of the nanostructure. Here, the photon incidence angle is tangential to the bend of the V-shaped nanostructure, as seen in Fig.5.7a.

The resistance of the nanostructure was 600 Ω and it was mounted in a parallel arrangement with a SMD resistor of 330 Ω on the chip-carrier (see details on the parallel arrangement of the sample with a SMD resistor in subsection 4.1.1).

5.3.1 Propagation of a Transverse Wall

Because a well-defined magnetic ground state was needed to do the current induced domain wall motion measurement, the magnetization of the nanostructure was initialized by an in-situ in-plane static magnetic field (40 mT). The white arrow in Fig.5.7a shows the direction of applied field. As a consequence, we obtained a transverse wall at the bend of the nanostructure, as seen at site A in Fig.5.7a. Here, a transverse wall separates two domain regions where the spins in each domain, as shown in the zoom-in by the red arrows, are pointing in opposite directions [68].

Results

Starting from the initial state shown in Fig.5.7a, first we injected low amplitude current pulses and then slowly increased the current density. By this approach, we acquired the critical current density of $6.4 \times 10^{11} \mathrm{A/m^2}$ at which the transverse wall started to move.

By applying a 100 ns pulse with current density of $6.4 \times 10^{11} \mathrm{A/m^2}$, the transverse wall moved from the bend to the right-hand side arm up to 2 μm in the electron-flow direction, as shown at the site A in Fig.5.7b. In addition, a small domain also appeared at the site B.

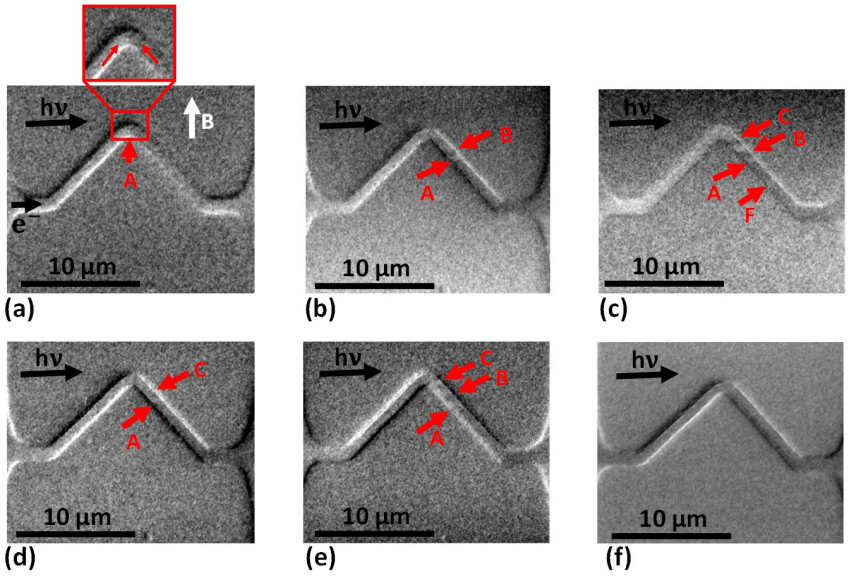

Figure 5.7: (a) Ground state in 700 nm wide and 40 nm thick $Ni_{20}Fe_{80}$ nanostructure. The transverse wall at the bend (site A) was produced by in-situ static magnetic field (40 mT). White arrow shows the direction of applied magnetic field. (b) The transverse wall moved up to site A and another small domain at site B is appeared due to the first pulse of magnitude ($6.4 \times 10^{11}\mathrm{A/m^2}$). (c) The second pulse ($6.4 \times 10^{11}\mathrm{A/m^2}$) generated domain patterns at site C and F, respectively. (d) Due to the third pulse ($7.1 \times 10^{11}\mathrm{A/m^2}$), domain at the site F disappeared and the site B domain accumulated with site A domain. (e) The site B domain appeared again after the fourth pulse ($7.8 \times 10^{11}\mathrm{A/m^2}$). (f) Whole magnetic texture destroyed after the fifth pulse of magnitude ($8.5 \times 10^{11}\mathrm{A/m^2}$).

Fig.5.7c depicts the result of the second pulse having the same magnitude like the first pulse. This pulse created two additional domains at sites C and F respectively, however, the site A transverse wall remained unchanged. There is probably a local pinning center, which traps the domain at the site A .

Because the site A domain didn't change with the current density of $6.4 \times 10^{11}\mathrm{A/m^2}$, we decided to increase the current density up to $7.1 \times 10^{11}\mathrm{A/m^2}$. After

injecting this pulse, we observed that site B domain joined with site A domain and the site F domain disappeared, as seen in Fig.5.7d.

Next, we injected a pulse of the same magnitude like the third one, but the domain patterns remained unaltered (not shown here). Therefore, we decided to inject the fourth pulse of a current density up to $7.8 \times 10^{11} \mathrm{A/m^2}$. Due to this pulse, the site B domain appeared again as seen in Fig.5.7e.

Because we didn't find any change after applying the fifth pulse of $7.8 \times 10^{11} \mathrm{A/m^2}$, therefore we injected the sixth pulse of a current density $8.5 \times 10^{11} \mathrm{A/m^2}$. This pulse destroyed whole magnetic textures and we have lost the previous history of magnetization in the nanostructure, as seen in Fig.5.7f.

Discussion

In the literature [68, 69, 72, 137], a critical current density in the range of 10^{11}-$10^{12} \mathrm{A/m^2}$ is reported for a domain wall motion in ferromagnetic structures. Here, we acquired a critical current density of $6.4 \times 10^{11} \mathrm{A/m^2}$ for the transverse wall motion which is in that range.

The traveling of the domain wall scales with respect to the width of a pulse. An approximate speed can be obtained by dividing the total distance the domain wall covered during the applied pulse length. Here it is assumed that the domain wall moves during the whole time the STT acts, i.e. the pulse length, and afterwards does not move very long in a ballistic manner. A similar calculation was done in references [133, 138]. We observed different transverse wall displacements in the right arm of a V-shaped nanostructure at different places under different current densities. This observation strongly indicates the existence of pinning sites, as by increasing the current density, the movement of the transverse wall doesn't happen or occurs for a small distance. We obtain an approximate maximum transverse wall speed of 33 m/s for a current density of $6.4 \times 10^{11} \mathrm{A/m^2}$ and smaller speed of 1 m/s at a high current density of $7.8 \times 10^{11} \mathrm{A/m^2}$, obviously after reaching a pinning site. Fig.5.8a shows the

average velocity versus the current density for a transverse wall in our nanostructure. Our obtained speed values are in the range of known domain wall velocities in the literature [46, 55, 68, 71, 72, 138].

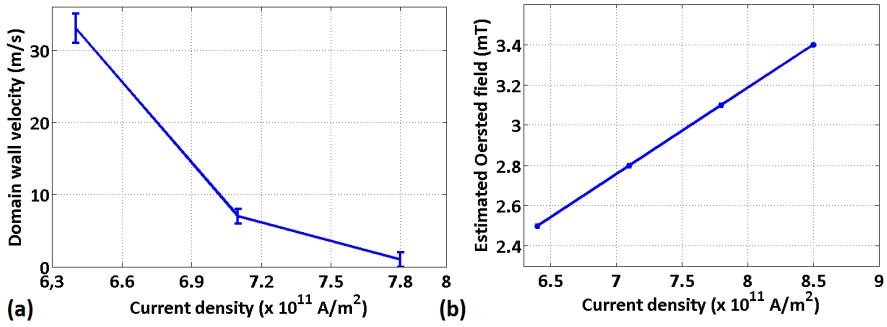

Figure 5.8: (a) Average velocity of three subsequent 100 ns current pulses with increasing current density. (b) Oersted field as a function of current density.

An Oersted field could change the magnetization textures inside the structure. It can be calculated according to Ampere's law:

$$\mathbf{B}(\mathbf{z}) = \frac{\mu_0 \mathbf{J}\mathbf{z}}{2\pi} \tag{5.3}$$

where **J** is the current density and **z** is the distance measured from the center of the nanostructure. For different current densities, we have estimated the Oersted field, as shown in Fig.5.8b. The maximum estimated Oersted field is 3.4 mT for the current density of $8.5 \times 10^{11} \mathrm{A/m^2}$. The transverse wall moved in the direction of electron flow is in agreement with the theory of L. Berger [9] and this motion is attributed to the STT like in references [46, 55], while it would not be in the direction of electron flow due to an Oersted field, as the Oersted field does not favor the domain wall motion along the nanostructure. As in [55, 139], where the Oersted field was even up to 7.4 mT and 9±1 mT respectively, our 3.4 mT is too small to affect the magnetic texture.

As discussed in subsection 5.2.5, when a current pulse flows into a nanostructure, its temperature increases due to Joule heating effect [33, 146, 147, 149].

This effect can decrease the magnetic moment or spin torque needed to move the domain wall inside the structure [152]. From another point of view, this effect could reduce the energy barrier for a pinned domain wall and promote the depinning [55, 105]. But in this measurement, the observed domains seem to be often pinned strictly at their positions and in some cases, after moving a larger step with the first pulses, they proceed only by small distances upon further pulses with increased current density.

Because the new magnetic state after the fifth pulse, as shown in Fig.5.7f, was not useful to continue the measurement, we applied an in-situ in-plane static magnetic field again to repeat the experiment on this nanostructure. We will discuss its detail in next subsection 5.3.2.

5.3.2 Propagation of a Transverse Wall and Creation of Multiple Domains in a $Ni_{20}Fe_{80}$ V-shaped Nanostructure

To repeat the experiment, the magnetic textures in the nanostructure are initialized by the in-situ in-plane static magnetic field (40 mT). As a result, the transverse wall is again initialized at the bend of the V-shaped nanostructure, as seen at the site A in Fig.5.9a. This is nucleated at the same location as in the previous subsection 5.3.1. The direction of the applied field is shown by the white arrow in Fig.5.9a. The zoom-in of the bend region shows a transverse wall along with the red arrows to help visualization of the magnetization direction of the domains.

This time, we have positioned the photon incidence angle parallel to the left arm of the nanostructure to be more sensitive to the magnetization in the left and the right arm.

Results and Discussion

We injected the first single pulse of same current density 6.4×10^{11} A/m^2 at which we have observed the motion of the transverse wall in the last subsec-

tion. Here, we again noticed that the transverse wall moved up to 500 nm in the direction of the electron flow, as shown at the site A in Fig.5.9b. In the zoom-in of the transverse wall at the site A, the red arrows help to visualize the magnetization direction of the domains. The central red arrow depicts the brighter region which is the transverse wall boundary between the upper gray and the lower dark domains.

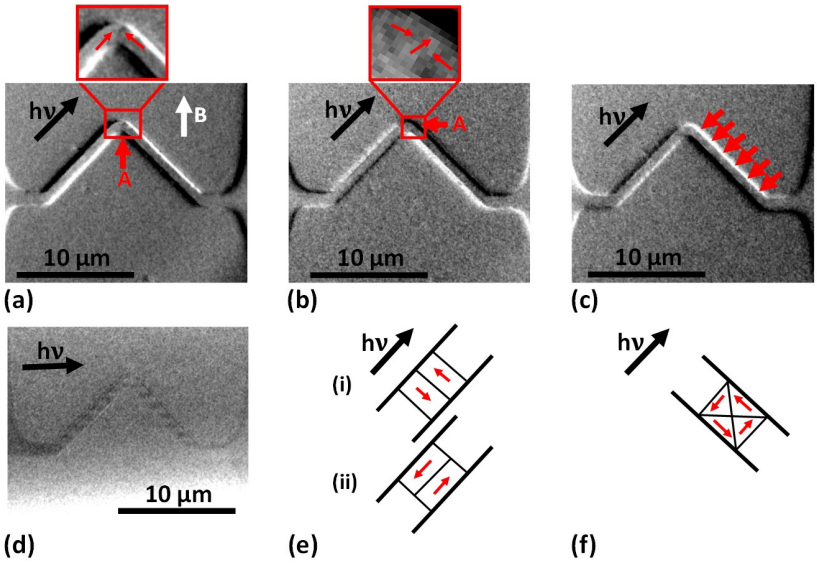

Figure 5.9: (a) Again, the transverse wall was produced at the bend (site A) by applying the in-situ static magnetic field (40 mT) in the same location as in the previous subsection 5.3.1. (b) The transverse wall motion at the site A via first pulse (6.4×10^{11} A/m^2). (c) Multiple domains on the right arm of the nanostructure after applying an additional high pulse of current density 9.1×10^{11} A/m^2. (d) Multiple domains on both arms after applying a high pulse 9.3×10^{11} A/m^2 and recording the XMCD image with an incidence angle different by 45° from the XMCD image of (c). The (e) and (f) show the sketches of the spin arrangements in textures.

Next, we injected the second pulse of same current density 6.4×10^{11} A/m^2,

but the transverse wall didn't move (not shown here). After that, we consecutively applied the current density of 7.5 $\times$ 10^{11} A/m^2 and 8.5 $\times$ 10^{11} A/m^2 respectively, however, the transverse wall stayed unaltered (Images are not shown here). This is probably due to a pinning center at the site of A (see details on different pinning potentials in section 2.7).

Because even after applying the high current pulse of 8.5 $\times$ 10^{11} A/m^2, the transverse wall didn't move, therefore we speculated that there was probably an increased pinning potential at the used sample which did not allow the transverse wall motion (not shown here).

So we applied a larger current density of 9.1 $\times$ 10^{11} A/m^2. This pulse split only the single dark-gray domain pattern on the right arm into multiple domains, but we haven't seen multiple domains on the left arm (see in Fig.5.9c). Let's assume that the left arm has domains. What can be their spin structure as they are invisible? Further, assume that they are stripe-like domains, anti-parallel to each other and lie either along the width direction of the nanostructure or lie along the length direction of its arms, as seen in sketches of Fig.5.9e(i) and e(ii). Are these probable arrangements of spin configurations in such nanostructure? The answer is definitely no because nature wants them to be arranged in flux closure patterns. When the incidence photon angle is parallel to the left arm, at least both parallel and anti-parallel domains to the incidence photon angle must be visible, but we even didn't observe them. This means that there is still a single domain on the left arm after applying the larger current density of 9.1 $\times$ 10^{11} A/m^2, as seen in Fig.5.9c. By the same reason, domains on the right arm must be flux-closure patterns, as sketched in Fig.5.9f. Here, each flux-closure domain pattern appeared in stripes of only two colors, although there are probably 4 domains with the magnetization in 4 directions.

Next, we applied a higher pulse of 9.3 $\times$ 10^{11} A/m^2 and then recorded the XMCD image with an incidence angle different by 45° from the angle of XMCD image of Fig.5.9c. As a consequence, multiple domains appeared on both arms of the nanostructure, as seen in Fig.5.9d. On the basis of above paragraph dis-

cussion, we conclude that both arms contain flux closure domain patterns but appearing in stripes of only two colors.

We have observed some different results in this subsection while measuring the same V-shaped nanostructure which was measured in the previous subsection 5.3.1. For example, multiple domains were generated after applying a high current pulse. Second, the pinning effect is larger than the previous subsection 5.3.1. This time, the large pinning effect could be an indication that the repeated applied pulses had deteriorated the sites or surface of the nanostructure and generated a strong pinning potential for the transverse wall motion. Using the analytical equation 5.2 of references[33, 148, 149] as described in subsection 5.2.5, we get ΔT up to 500 K for this $Ni_{20}Fe_{80}$ nanostructure.

Conclusion

Here, we have experienced a different strength of pinning effects for the transverse wall while applying the same current density to the same sample as in the subsection 5.3.1. Second, we have observed an increased temperature effect on the spin textures due to which the single domain split into multiple domains. Third, the approximate speed of a transverse wall, in this case, is 7.5 m/s. This speed value is smaller than the known domain wall speed from the literature [46, 55, 68, 71, 72, 138], possibly due to the fact that we integrate over the time when the transverse wall really moves and the time when it already stuck at the pinning center.

5.4 Current Induced DW Motion in $Ni_{20}Fe_{80}$ Notched Half-ring Shaped Nanostructure

In the section 5.2, we presented experimental results on 12 μm long, 40 nm thick and 1μm wide Ni_{20} Fe_{80} half-ring shaped sample. We used a pulse of 100 ns for that sample. Here, we present a 20 μm long, 40 nm thick and 1μm wide Ni_{20} Fe_{80} geometrically notched half-ring-shaped nanostructure, having an Ohmic resistance of 560 Ω. In the previous experiment of section 5.2, we

found the temperature influence on the magnetization textures by using 100 ns wide pulse. This is because a long pulse delivers a considerable energy to the nanostructure which affects the magnetization inside. Therefore, here we decided to use 20 ns wide pulses. Another improvement here is to introduce the notch in the nanostructure in order to see the motion of magnetic texture at a defined pinning center.

The sample fabrication and the experimental setup was the same like for the samples in the previous sections.

5.4.1 Propagation and Transformation from Vortex-like Flux Closure Domain Pattern to Transverse Wall

First, we need a favorable domain pattern in the structure for doing current induced domain wall motion measurements. For this, the magnetization of the nanostructure is initialized by an in-situ in-plane magnetic field. We chose the direction of applied field with the intention that the domain wall was generated at the middle of the notched half-ring nanostructure. The direction of the applied field is marked by the white arrow in the Fig.5.10a. The resulting magnetic domain pattern along with the domain wall is shown in Fig.5.10a.

Results and discussion

A closer inspection of the domain wall at site X in Fig.5.10a reveals that there is a vortex-like flux closure domain pattern situated near to the left side of the notch, which is identifiable by bright-dark contrast: in this configuration, the brighter domain must be magnetized parallel to the photon polarization vector and the darker region must be anti-parallel and the magnetization is curling around its own center, so-called vortex core, where the magnetization points out-of-plane [48]. The vortex-like flux closure is indicated by a red rectangle in Fig.5.10a which is further zoomed-in and shown by red arrows in Fig.5.10p. The XMCD image in Fig.5.10a was recorded with the photon incidence angle nearly along its arms (see black arrow). We define this angle as a 0°. Here

the magnetic texture can not be unambiguously determined by an XMCD image at only one photon incidence angle, therefore we illuminated the sample at two other angles different by 22° and 45° from the photon incidence angle in Fig.5.10a, respectively, as shown in Figs.5.10f and k. In Fig.5.10k, the contrast of the vortex-like flux closure domain pattern appears slightly more bright on the left side after 45° angle of rotation.

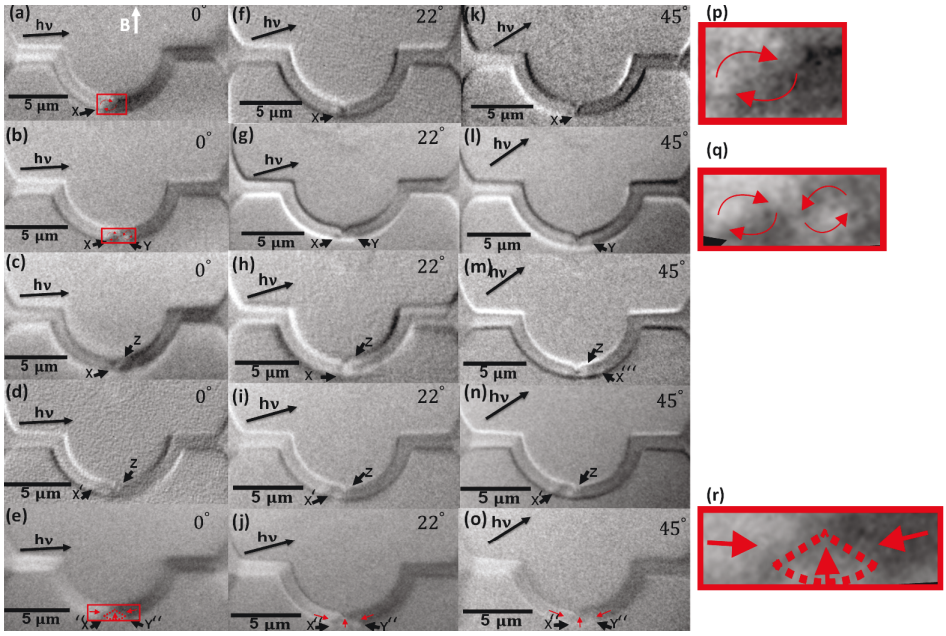

Figure 5.10: XMCD-PEEM images, at three different photon incidence angles, of a Ni_{20} Fe_{80} half-ring-shaped, 20 μm long, 40 nm thick and 1μm wide nanostructure. The (a-e) Images are collected with photon incidence angle along the arm of half ring. This angle is defined as a 0° . The (f-j) images and (k-o) images were taken at the photon incidence angles of 22° and 45°, respectively. The column of images (p-r) depicts the zoom-in of the magnetic textures of the left columns. Subsequent pulses with a current density of $8.7 \times 10^{11}\mathrm{A/m^2}$ were injected from b) to e).

After observing a vortex-like flux closure domain pattern, we injected consecutive current pulses of same magnitude $8.7\times10^{11}\mathrm{A/m^2}$ into it. XMCD images

that have been recorded after each current pulse were compiled in three separate columns in Fig.5.10. The column of images (a-e) was recorded with the photon incidence angle at 0°. The columns of XMCD images (f-j) and XMCD images (k-o) were recorded with different angles 22° and 45°, respectively. The fourth column of images (p-r) depicts the zoom-in of magnetic textures which were found in the columns to the left.

In the beginning of the measurement, we slowly increased the current density and achieved the critical current density of magnitude $8.7\times10^{11}\mathrm{A/m^2}$ where the magnetic textures start varying.

After applying the first pulse of magnitude $8.7\times10^{11}\mathrm{A/m^2}$, we observed that the vortex-like flux closure domain pattern moved by 230 nm in the direction of electron flow with a speed of 11.5 m/s, and a second vortex-like flux closure domain pattern, with anti-clockwise sense of rotation, appeared at the right side of the notch as sited by Y (see zoom-in in Fig.5.10q).

Applying the pulse of the same magnitude $8.7\times10^{11}\mathrm{A/m^2}$ again, we observed that both vortex-like flux closures at the site X and Y disappeared and a new bright spot at the site Z appeared as seen in Fig.5.10c. The reason for this new magnetic texture could be a temperature rise: after the absence of any magnetic order in the hot state of a nanostructure, during the cool-down, a reordering occurs.

After applying the third current pulse of the same magnitude $8.7\times10^{11}\mathrm{A/m^2}$, we unexpectedly observed that the boundary of magnetic textures has changed from right- to the left-hand side of the notch, as sited by $X^{'}$ in Figs.5.10d, i and n.

Here, we have some observations which are different from our previous current induced domain wall motion measurements. In the literature it was never reported that a domain wall by STT moved opposite to the electron flow direction. If it is then this could be due to some other effects like Joule heating or

Oersted field [49, 55, 150]. We have estimated the maximum Oersted field to 3 mT by using the equation 5.3, which is smaller than the reported Oersted field in the literature [55, 124]. Hence, this magnitude is probably too small to affect the magnetic texture. Here it is important to mention that the temperature is proportional to a current density, as it is expressed by mathematical equation 5.2 of ΔT in subsection 5.2.5. By following the analytical expression from the references [33, 148, 149], we estimate a ΔT of 523 K for a 20 ns single pulse. This means that our nanostructure temperature may reach up to the Curie temperature of a $Ni_{20}Fe_{80}$ material used ($\sim$ 860 K). Hence, in this structure, changes in the magnetic texture is attributed to the STT assisted by a temperature rise.

When we injected the fourth pulse of same current density $8.7 \times 10^{11} \mathrm{A/m^2}$, the magnetic texture has moved back again from left- to the right-hand side in the direction of electron flow, as marked the new position of the texture by X'' in Fig.5.10e. By combining this with the information from the angles 22° and 45°, we observed the triangular shape of a transverse wall in the vicinity of the notch (see in Figs.5.10e, j and o). It is indicated by the red triangle along with the red arrows on the opposite domains, as shown in the zoom-in image in Fig.5.10r. Different from the vortex-like flux closure domain pattern, the transverse wall occurs in a thin and narrow geometry. Hence, the narrow region, below the notch, favors the transverse wall.

After applying the fifth pulse the nanostructure was disrupted and not conducting any more. Again here we conclude that the (thermal) contact to the substrate and may be also the crystalline structure was altered by each subsequent pulse so that in the end a pulse of the same current heated the sample more than the previous ones.

Conclusion

The magnetic texture of this notched, 1 μm wide structure responded in different ways on the subsequent $8.7 \times 10^{11} \mathrm{A/m^2}$ pulses: Although the notch could act as a pinning center, it was possible to move the domain wall with this

relatively low first pulse. Later on, at the 3rd pulse of the same current, new magnetic structures appeared in the opposite arm, originally mono-domained. Here, the Joule heating could lead to a local destruction of the ferromagnetic order and as a result, the magnetic texture is destructed and then re-nucleated again in a different magnetic configuration. Thus, as in the previous samples, we are in the current regime where both STT and heat-up towards vicinity of the Curie temperature are coexisting. Different from the other samples here we observed the conversion from a vortex-like flux closure domain into a transverse wall.

5.5 Conclusion

In this chapter, the reaction of magnetic domains and domain walls upon individual current pulses in the $Ni_{20}Fe_{80}$ (different in composition from the permalloy, $Ni_{80}Fe_{20}$) nanostructures were studied.

We performed single pulse experiments in $Ni_{20}Fe_{80}$ for the first time and it was found that this alloy is an interesting candidate for studying the fundamental understanding of the spin transfer torque phenomenon in single layer systems. Its larger magnetic moment compared to $Ni_{80}Fe_{20}$ made it easier to visualize the magnetic texture, as the XMCD effect is proportional to the magnetic moment. Secondly, measurements carried out indicate that different from $Ni_{80}Fe_{20}$, this alloy is favorable for the occurrence of multi-magnetic domain patterns in the nanostructure. This could be due to a thermal-stress on the sample that may result from a larger magnetostriction after temperature rise. However, the disadvantage of the larger magnetostriction could be the destruction of the samples.

In $Ni_{20}Fe_{80}$ nanostructure, both vortex-like closure patterns and transverse walls are found. They were either moved or transformed to another shape by a high current density. Such a high current density causes a temperature rise up to Curie temperature in the nanostructure. The measurements carried out suggest that this temperature rise prevents the observation of STT at room tem-

perature. Rather than creation of domains in the nanostructure by the STT, Joule heating was found to be strong. To the best of our knowledge, in our measurements, for the first time, multiple flux closure domain patterns (i.e. Diamond patterns) were observed. We observed the small motion of these patterns which indicates that the speed could be strongly influenced by a number of magnetic patterns. Moreover, we observed the splitting of a flux closure domain pattern into two, however splitting of a vortex wall into two was already observed in [46]. In addition, the set of measurements, domain wall motion in a notched half ring-shaped nanostructure, allowed us to observe the vortex-like flux closure conversion into a transverse wall during the application of 20 ns current pulses. We found this conversion in a 1 μm notched half-ring shaped, where the vortex-like flux closure was created next to the notch and it transformed into a transverse wall below the notch where the width of a nanostructure is smaller. This result indicates that the wall creation in a magnetic texture depends on the nanostructure geometry. This conversion in the magnetic contrast is attributed to the STT assisted by a temperature rise. We could not ignore the temperature rise here as it is directly proportional to the applied current density (see equation 5.2). As a consequence, as the goal in future current induced domain wall motion experiments as well in memory devices, in order to have a controlled motion of domain walls by STT, must be to avoid Joule heating and hence to use a short current pulse up to $\sim$1 ns, as longer current pulses add more energy to a domain texture.

We have witnessed natural pinning sites in $Ni_{20}Fe_{80}$ nanostructures, which strongly affected the velocity of a domain wall motion. When injecting 100 ns long pulses, a maximum domain wall velocity up to 33 m/s and a minimum of 7 m/s observed and for a 20 ns pulse, a velocity of $\sim$11 m/s was estimated. Though our velocities are in a range of the literature, but we found inconsistency in a data relevant to the speed. For example, you can find a maximum speed of 700 m/s and a smaller down to 1 m/s. This inconsistency can be attributed to the material imperfections, for example, edge roughness, surface damages etc. Now the question is: how do these structural damages happen ? The answer could be a high current density due to which structural changes

already started after the first pulse. In our case, in spite of the fact that we could not estimate the strength of pinning locations, our experiments highlight the importance and effects of these sites on a domain wall motion.

Chapter 6

Time Evolution of Magnetization in $Ni_{80}Fe_{20}$ Nanostructure

In chapter 5, we have studied the magnetization changes in $Ni_{20}Fe_{80}$ nanostructures after several subsequent pulses of 20 ns or 100 ns length in the single pulse experiments. The magnetization dynamics was not and cannot be addressed in these experiments, e.g. the question if these changes happened during the rise of the pulse or during the whole time duration. The sum of X-ray magnetic circular dichroism (XMCD) images of many billions of X-ray flashes are needed to visualize domains or domain walls (DW), but in a ns, there would be only 1 X-ray pulse available from the synchrotron. The study of dynamics requires a setup with following elements:
(1) A reversible process in the sample, returning always back to the initial state so that the next X-ray flash probes the same (time dependent) state.
(2) Synchronization between the excitation (pump) and the X-ray pulse (probe) used for imaging, so that billions ($\sim 10^9$) XMCD images can be recorded and added, showing the same time status of the excitation.
(3) Tunable time delay between pump and probe to study the evolution of magnetization at different times after the excitation.
As explained in chapter 4, the repetition time of 2 ns during the multibunch (MB) operation is incompatible with the ns-time resolution needed here, so that for pump-probe experiments either at best single bunch (SB) operation is used or as second best option is the negative deflection gating (see section 4.4) during MB operation. The time-resolved XMCD images shown in this chapter were

recorded during SB time with repetition rate of 1.25 MHz.

As a first step, we have to characterize the exciting current pulse itself. This is done first with an oscilloscope (see subsection 6.1.1) and then realized on the sample by means of the photoemission electron microscope (PEEM) with X-rays (see subsection 6.1.2). The dynamical effect of the current pulse on domains in a $Ni_{80}Fe_{20}$ half-ring shaped nanostructure is presented in section6.2. Note that the NiFe alloy, $Ni_{80}Fe_{20}$, used here is different from $Ni_{20}Fe_{80}$, used in chapter 5 (see section 3.2 for comparison between the properties of both NiFe alloys).

6.1 Characterization of the Applied Voltage Pulse at the Sample

Because we want to study the magnetization dynamics in a nanostructure at nanosecond scale, the required current pulse needs to be short enough ($\sim$ 1 ns) with sufficiently high amplitude. Both properties were monitored first by an oscilloscope (see subsection 6.1.1) and then by the effect of the electric potential changes on the PEEM images (see subsection 6.1.2). The latter gives the most realistic pulse shape at each individual sample, including the damping and distortion effect of cables of non-matched impedance.

The fabrication process for our sample is the same as described in section 3.1.

6.1.1 Ex-situ Test of the Pulse Shape

In Fig.6.1, we show a PEEM image of 180 Ω, 10 μm long, 1000 nm wide and 40 nm thick notched $Ni_{80}Fe_{20}$ half-ring shaped sample along with the wiring scheme. The sample floats on the potential of -6 kV throughout the measurement. An avalanche photo-diode (APD) is triggered by a diode-laser from outside the vacuum through a window. The APD bias is controlled by the HV-floating supply of the microscope (ADAM).

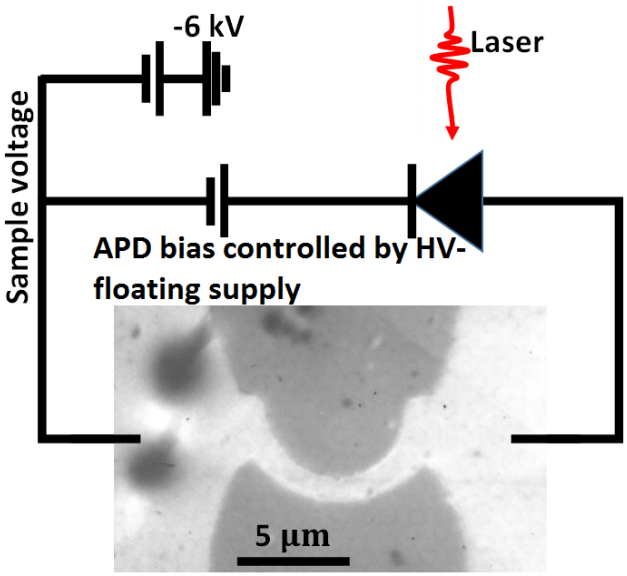

Figure 6.1: PEEM image of the sample along with schematic on the setup. Sample floats on the potential of -6 kV. Avalanche photo-diode (APD) is triggered by laser. The APD bias voltage is controlled by a HV-floating power supply (ADAM).

Because it is difficult to measure the current pulse on the sample by oscilloscope due to technical limitation once it is inside the X-PEEM microscope, we recorded it outside the X-PEEM instrument on an oscilloscope while the photoswitch is triggered by a diode-laser (635 nm, 100 mW). A 1000 Ω resistor as a dummy sample was mounted in parallel to the SMD resistor of 330 Ω on the sample holder. The recorded pulse, as shown in Fig. 6.2, has a width of $\sim$ 1 ns at an amplitude of 5.2 V. Besides the regular pulse, there is also a negative reflected peak due to imperfect impedance adaption with the 1000 Ω resistor. The photodiode is operating in the visible red regime. For this test, the diode-laser had 5 MHz repetition rate and was triggered from a delay generator.

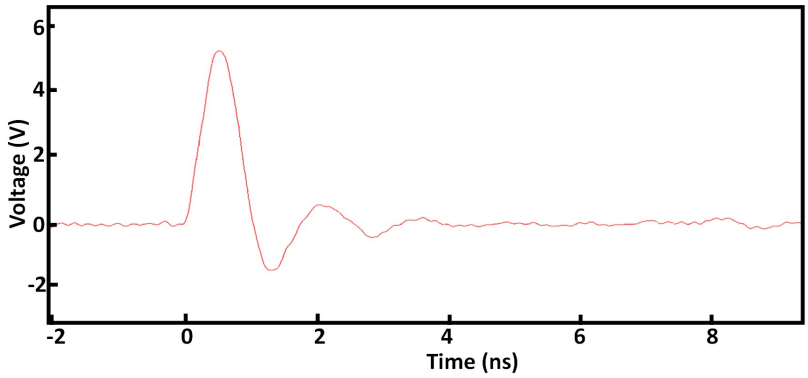

Figure 6.2: Pulse of $\sim$ 1 ns wide with 5.2 V amplitude recorded on an oscilloscope after the laser pulse hitting an avalanche photodiode integrated at the end of sample holder. The resistance of the dummy sample was 1000 Ω and it was mounted in parallel to the SMD resistor of 330 Ω on the sample holder.

6.1.2 Measurement of the Voltage Pulse at the Sample Inside the X-PEEM Instrument

We applied a method to measure the voltage pulse on the sample while operating the setup in the ***single-bunch mode***. We employed the time-resolved secondary electron spectroscopy to get precise information about the voltage pulse on the sample.

Start energy variation technique

By varying the start energy, a displacement of the electrons is visible in the diffraction plane and that movement can be calibrated. For this, we took two reference images in the diffraction plane with a start voltage at 0 V and 4 V respectively. The parabolic shape of the spot, seen in Fig. 6.3, represents the (θ_x, E) distribution of the electrons, where θ_x is their (horizontal) momentum component perpendicular to the dispersion plane. Both images are depicted in Fig. 6.3. The displacement for 4 V is marked by an arrow between the parabolic distribution of electrons in both images. This difference will be taken as a reference

for the voltage pulse calibration at the sample.

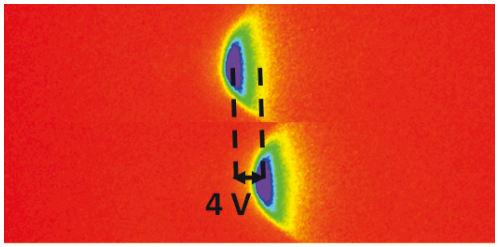

Figure 6.3: (a) Parabolic distribution of electrons in the diffraction plane taken at two different start voltages, having a start energy difference of 4 V.

Placement of the field aperture at the pulsed region of the sample for the pulse determination

In the second step, our motive is to see electrons of only the pulsed region of the sample in the diffraction plane. Because the pulse is fed into the lower pad, this pad experiences a change of its potential, but the remaining regions, for example substrate or surrounding grounded fields, stay almost unchanged at the onset of the pulse. Hence, the energy spectrum of the emitted photoelectrons is shifted in the diffraction plane by the local time-dependent start energy. This effect cannot be readily seen in the diffraction plane images, even when the pulse is synchronized to a particular X-ray flash, because the electrons from all sample areas are mixed in the diffraction plane, most of them not undergoing a varied start potential. Therefore, we placed the field aperture in such a way that emitted photo-electrons only from the lower pad arrive at the detector. The dotted red circle in the Fig. 6.4b presents the position of the field aperture on the sample.

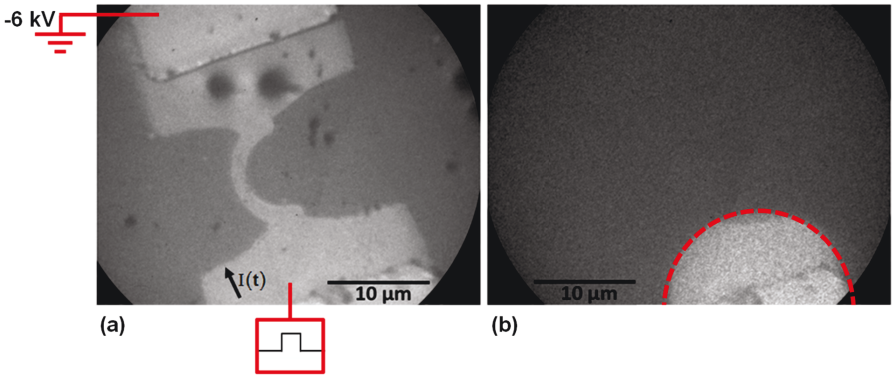

Figure 6.4: PEEM images showing the use of the field aperture for the determination of the pulse voltage arriving at the sample: a) without aperture, b) the field aperture positioned such that only the contact pad, into which the electric pulse is injected, is visible. The red dotted line depicts the boundary of the field aperture.

A time series of the (θ, E) spectrum

In the third step, first we synchronized the pump (current) pulse with the probe (x-ray) single-bunch. After that, we recorded the shift of the (θ, E) parabola in the dispersion plane upon changing the delay from 0 ns up to 4 ns in steps of 100 ps. This time series of the spectrum as seen in Fig. 6.5a shows the shape of the pump pulse that arrived at the sample. Fig. 6.5b shows a spline fitting on the time behavior of the pump pulse.

For measuring the peak value of the arriving pulse at the sample, we compared the two images corresponding to the emitted photoelectron distributions which were recorded in the dispersion plane at 0 ns and 0.9 ns delays between the pump and probe, as seen in Fig. 6.5c. The zero of the time scale was defined as the moment just before the first displacement and the 0.9 ns image displays a maximum amplitude of the pump pulse arrived. By using the start energy variation technique as a reference, we estimated a difference of 6.4 V between

the 0 ns delay image and a maximum amplitude image (recorded at the delay of 0.9 ns) of the parabolic distribution.

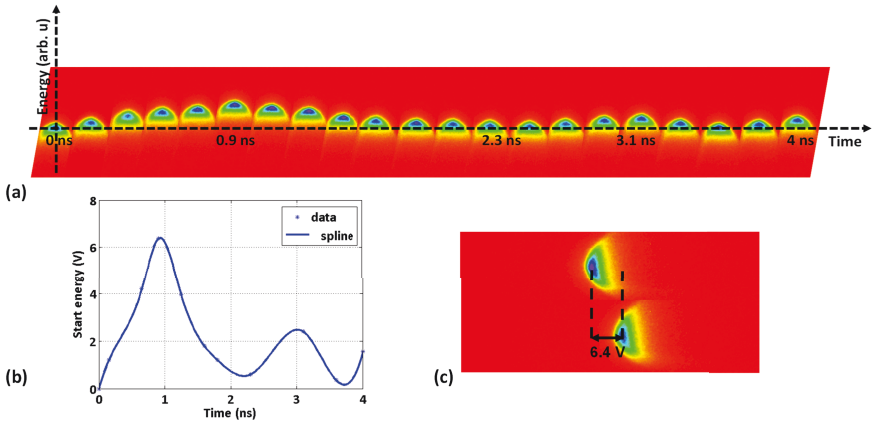

Figure 6.5: (a) Shift of electron distribution in the diffraction plane as a function of time delay between current pulse and X-ray probe. (b) A spline fitting on the spectrum illustrating the oscillatory shape of a pump pulse. This pulse has no negative journey as it has strong damping and the reflection is much controllable. (c) Difference between the parabolic distribution of emitted electrons of two images which were recorded at 0 ns and 0.9 ns delay between the pump and a probe.

Similarly, we have placed the field aperture on the grounded pad of the sample (a time series is not shown here) and found a maximal potential change of only 0.5 V on it. This method characterized that the magnitude of the arriving voltage pulse at the sample is 5.9 V. As this pulse was measured on the sample (see Fig. 6.5b), it has strong damping and the reflection is much better under control than the dummy sample pulse of Fig. 6.2. Here, we have never observed a negative amplitude of the pulse. This might be due to the damping. With R_{sample}=180 Ω and $width \times thickness$= 1000 nm$\times$40 nm, we obtain a peak current density of 4.9 $\times$ 10^{11} A/m^2, that acts on the nanostructure.

With these pulses, we performed a dynamic mapping of the magnetization

in the sample by synchronizing current pulses with the BESSY bunch clock while operating the system in the single-bunch mode. The results are shown in the section 6.2.

6.2 Magnetization Dynamics in a Notched $Ni_{80}Fe_{20}$ Nanostructure via Pump-Probe Technique

Here, we present a dynamic mapping of a domain wall in a notched $Ni_{80}Fe_{20}$ half-ring shaped nanostructure by synchronizing the current pulses to the bunches in single-bunch mode of synchrotron radiation. The reversible motion of a domain wall in a controlled way was determined on a nanosecond time scale, using the APD pulses characterized above. We used the same sample as already described in the section 6.1.

Because the stroboscopic measurement requires a stable and well-defined magnetic ground state, the magnetization of the nanostructure is initialized by an in-situ in-plane magnetic field. To create a domain wall (DW) in the middle of a notched half-ring nanostructure, we applied an in-plane magnetic field perpendicular to the nanostructure. A white arrow in Fig. 6.6a shows the direction of the applied field. As a result, we generated a triangular-shaped domain and the domain wall between two domain textures was not pinned to the notch, as seen in Fig. 6.6a. Obviously, there was a natural pinning center on the right side from the notch. The maximum current density of 4.9×10^{11} A/m^2 is applied during the pump-probe measurement.

After establishing the zero time of the pump-probe delay as described in Fig. 6.5, we recorded the XMCD images at different delays and observed the time evolution of the magnetization. We display all XMCD images (a-e) in a column in Fig. 6.6. A guide to the eye for the triangular-shaped domain pattern along with the domain wall in each XMCD image is given by the dashed yellow lines. The inset shows the oscillatory shape of the pump (current) pulse.

Results

In the first step, we measured the XMCD at a delay of 1.5 ns i.e. a time between first peak and first valley and observed changes in the domain wall. Besides the peak current, the integral of the current and hence of the deposited energy might be relevant, which is largest at ∼1.5 ns. Therefore, this delay has been selected. As a result, the domain wall changed its shape from a so-called straight line to a shape like the inverted letter "S" and the triangular-shaped domain next to the notch remains unchanged, as seen in Fig. 6.6b. This is probably due to the notch acting as pinning location there.

Next, the XMCD image was recorded at the first peak of the pulse (0.9 ns). As a result, the domain wall changed its inverted S-shape to a S-shape under the action of the current, as seen in Fig. 6.6c. The triangular-shaped domain is not even changed by the influence of the first peak.

In the third step, we have measured the XMCD image at 3.3 ns .i.e. a time between second peak and second valley. Under the influence of this delay, the S-shape of the domain wall changed back to the inverted S-shape (Fig. 6.6d), though much less pronounced.

Because the domain wall has changed its shape back to the inverted S-shape, we measured again at the first peak to reconfirm the reversible changes in the domain wall. As a consequence, the domain wall fell back to S-shape from the inverted S-shape, as seen in Fig. 6.6e. This sequence of events confirms that the changes in the domain wall are reversible. It is worthy to note that the triangular-shaped domain remains unchanged at each and every delay measurement.

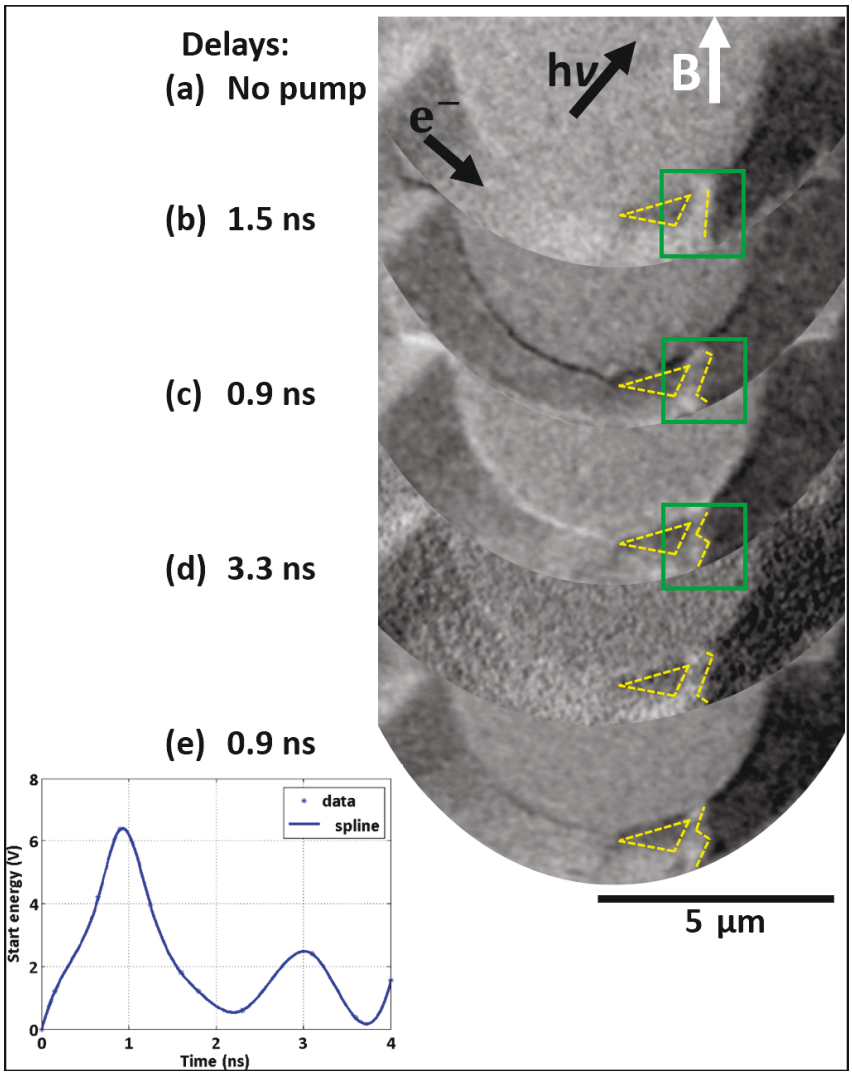

Figure 6.6: (a) Ground state XMCD image of the nanostructure, having a triangular-shaped domain next to the notch and a domain wall right of that. (b) XMCD image at the delay of 1.5 ns (a time between first peak and first valley). (c) XMCD image at the first peak, showing the domain wall in S-shape. (d) XMCD image at the delay of 3.3 ns (a time between second peak and second valley).(e) XMCD image of the nanostructure at the first peak again. The inset shows the oscillatory behavior of the pump (current) pulse. A guide to the eye for the triangular-shaped domain pattern along with the domain wall in each XMCD image is given by the dashed yellow lines. The green square frames in (a), (b), and (c) are referred to in Fig.6.7, Fig.6.8. A maximum current density of 4.9×10^{11} A/m^2 was used in the measurements.

Discussion:

Fig.6.7 shows the unpumped ground state of a nanostructure, where a triangular-shaped domain is fixed next to the notch and the domain wall between two domain textures appeared right of the triangular-shaped domain. A guide to the eye for the triangular-shaped domain pattern is given by the dashed yellow lines and the red arrows show the direction of the magnetization in the domain wall. Here this wall separates two domain regions where spins in each domain, as shown by red arrows, are pointing in opposite directions, a so-called transverse wall. As mentioned in the result segment, the bright/dark border of the transverse wall deformed towards an "S"-shape (at 0.9 ns delay) or inverted "S"-shape (at 1.5 ns). This means either that the transverse wall is really deformed to a S-/inverted S-shape or that the transverse wall is converted into a more complicated structure which makes only the bright/dark border appearing in a S-like shape. For example, the conversion of a transverse wall into a vortex wall could be also lead to such a shape. Such a conversion was described in micromagnetic simulations by many researchers and can be found in literature [14]. This was also experimentally reported by L. Heyne in his PhD thesis [48].

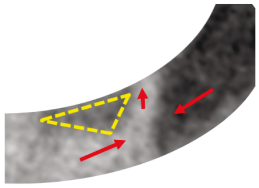

Figure 6.7: The unpumped ground state of the nanostructure.

Because of the limited available data, namely the poor statistics of images and especially the missing possibility in the pump-probe experiment to vary the azimuthal angle for the unique determination of the magnetization direction at all sites, it is impossible to unambiguously confirm the exact magnetization structure. Nevertheless, in the following subsection, we compare our experimental findings with the model of a string like oscillation of the transverse wall to examine if it is compatible with the experimental results and allow to deduce the approximate physical properties from the temporal behavior of the magnetization.

A string like oscillation of the transverse wall:

One possible interpretation could be the oscillation of the transverse wall like a string under the action of current pulses at different delays.

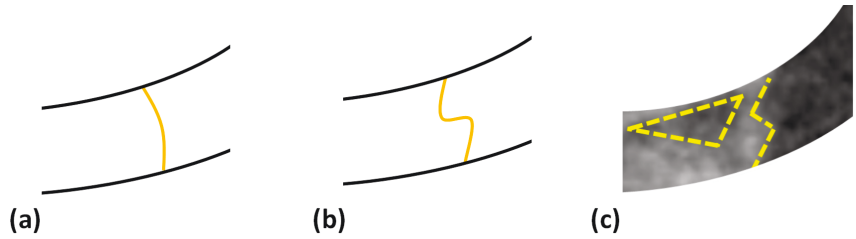

Figure 6.8: First harmonic (a), and the second harmonic (b) oscillations of the transverse wall (dark yellow). (c) An oscillation of transverse wall observed experimentally at the delay of 0.9 ns. A guide to the eye for the triangular-shaped domain pattern and the S-shape are given by the dashed yellow lines.

As the black/white border never moves at the boundaries of the nanostructure, the transverse wall seems to be pinned at the top and bottom. In between, after the excitation it looks like an oscillation of a string in second harmonics (see Fig.6.8). Now the question is: Can a transverse wall be described as oscillating like a string? To answer this question, we look at the formula for the oscillation frequency of a string:

$$f = \frac{1}{2L}\sqrt{\frac{T}{\mu}} \tag{6.1}$$

where L indicates the length of a string, T presents the tension and μ shows the mass per unit length (linear mass density) [56]. Similarly, a tension T can be associated to a transverse wall, being the energy needed for its elongation $T = \frac{dE}{dl}$, and an effective mass was commonly proposed to be inversely proportional to the square of the domain wall width t, i.e. $m \propto \frac{1}{t^2}$ [25, 107].

In this picture, the elongation of a transverse wall results in a change of its internal energy, ΔE, comparable with the string case where the amount of

elastic potential energy ΔE_{st} stored in a string is proportional to the elongation of its length:

$$\Delta E_{st} \propto Q\frac{\Delta l^2}{2L} \tag{6.2}$$

where Δl is the extension of the length due to excitation of a string, L is the natural length of the string and Q is the young's modulus [2].

In our case, when the spin-polarized current reaches the pinned dark triangle domain, the spin-transfer torque is partially blocked and hence is larger below the pinned dark triangle. After passing by it, the spin polarized current is creating an excentric excitation to the transverse wall. Such an excentric excitation for a string is known to excite more higher harmonics rather than the fundamental.

The strength of the current excitation depends on the selection of the delay. For example, the current excitation is higher at the delay of 0.9 ns which corresponds to the first peak of the pump pulse. Consequently this excitation of the transverse wall is strong. The current excitation is lower at the delay of 1.5 ns which could let the transverse wall flip back from the 0.9 ns state, into the opposite, inverted S-shape.

To obtain an approximation for the domain wall's oscillation frequency f, one can derive the frequency from the expression of the domain wall energy per area E_w [15]:

$$E_w = \pi\sqrt{AK_1} \tag{6.3}$$

where A=2J/a is the so-called exchange stiffness, where J presents the exchange integral and a is the lattice constant. The above equation 6.3 is valid for domain walls in the bulk of a crystal. K_1 is the magnetocrystalline anisotropy constant, which is zero in polycrystalline $Ni_{80}Fe_{20}$. For a thin film, K_1 must be rewritten with an additional term of $M_s^2/2$ for the shape anisotropy energy per unit area (see section 2.2.1). Hence the domain wall energy per area E_w can be

expressed as[15]:

$$E_w = \pi\sqrt{A(K_1 + M_s^2/2)} \tag{6.4}$$

where M_s is a saturation magnetization. Now the energy E of our domain wall can be written as:

$$E = E_w \times t \times l \tag{6.5}$$

where t and l are the thickness and length of the domain wall respectively. Now the domain wall energy per length is:

$$\frac{dE}{dl} = t \times \pi\sqrt{A(K_1 + M_s^2/2)} \tag{6.6}$$

Here, with the domain wall thickness t= 40 nm and the length l= 10^{-6} m, we derive $\frac{dE}{dl}$ = 2.75 $\times 10^{-13}$ J/m with the $Ni_{80}Fe_{20}$ saturation magnetization M_s = 800 kA/m, an exchange stiffness A= 13 $\times 10^{-12}$ J/m [114].

Next, we use the equation 6.1 for deriving the frequency of the domain wall. For this, we have checked several references for the effective domain wall mass. We found different values for the effective mass, for example in reference [112], the authors estimated the mass of (6.55$\pm$0.06) $\times 10^{-23}$ kg for a domain wall of cross sectional area 45 nm $\times$ 70 nm in a $Ni_{81}Fe_{19}$ semicircle nanowire. Nevertheless, we have taken the effective mass per unit length from the reference [107] where a mass of 1.3 $\times 10^{-24}$ kg for the domain wall of cross sectional area 20 nm $\times$ 2μm in a $Ni_{81}Fe_{19}$ half-ring nanowire was obtained, which has the same area as in our case. With a length of 1μm of our domain wall, we get the effective mass per unit length of 1.3 $\times 10^{-24}$ kg/m. By using this effective mass per unit length and $\frac{dE}{dl}$ = 2.75 $\times 10^{-13}$ J/m into the equation 6.1, we obtain the frequency of f_1=0.23 GHz for the fundamental excitation. The second harmonic is f_2=0.46 GHz.

Our second harmonic frequency has the same order of magnitude as in other publications [25, 59, 107, 112], for example, J. Rhensius et al. [107] estimated the oscillation frequency to (1.3 $\pm$0.6) GHz for the domain wall of equal area as in our case. Eiji Saitoh et al. [112] have determined the frequency to even 25 MHz, but their domain wall had the diameter of 50μm. Hence, it seems that the string

model can approximately describe the oscillations of the domain wall. Our obtained frequency ~ 0.46 GHz corresponds to a period of 2.17 ns. As seen in the inset of Fig. 6.6, 0.9 ns is the moment of our excitation pulse peak, where we get an "S"-Shape of the transverse wall. We assign this time of the strongest displacement to the first maximum of the sinusoidal oscillation. Accordingly, we adjusted the time in a generated sinusoidal function as shown in Fig. 6.9. Here, the 1.5 ns state falls into the negative half period of the sinus, though close to zero, compatible with the inverted displacement, i.e. a flip from "S"-Shape to the inverted "S"-Shape. For the 3.3 ns state, we also get the inverted "S"-Shape. This is not expected if we attribute the shape transitions to a sinusoidal oscillation, as at 3.3 ns it has a positive amplitude. We do not judge this contradiction with the oscillation model to be a major one, because i) the inverted "S"-Shape here is much less clear compared to 1.5 ns, ii) we are already in the second oscillation period, have neglected damping and moreover we have to consider the uncertainty of our frequency estimate: with only a 20% higher frequency the 3.3 ns point would fall already into the negative amplitude range.

Overall, the oscillating model with the estimated frequency can approximately describe the mechanism behind our experimental data, although it cannot be exactly confirmed due to both, the limited number of experimental time stamps, and uncertainties of parameters put into the model:

- Additional pinning, for example, at the surface or interface could immediately increase the frequency.
- The effective mass was transformed from another sample of reference [107].
- We assumed a harmonic, but the domain wall deformation oscillation may be an aperiodic case and to which no distinct frequency can be assigned.

The fact that the current pulse's temporal width, due to technical reasons, accidentally is similar to the expected oscillation half period, has an interesting aspect for future experiments: By exciting with currents of variable frequency, the resonance frequency of a domain wall could be probed and hence properties

like the effective mass m and energy of wall E may be determined via imaging of the resonating domain wall in a PEEM.

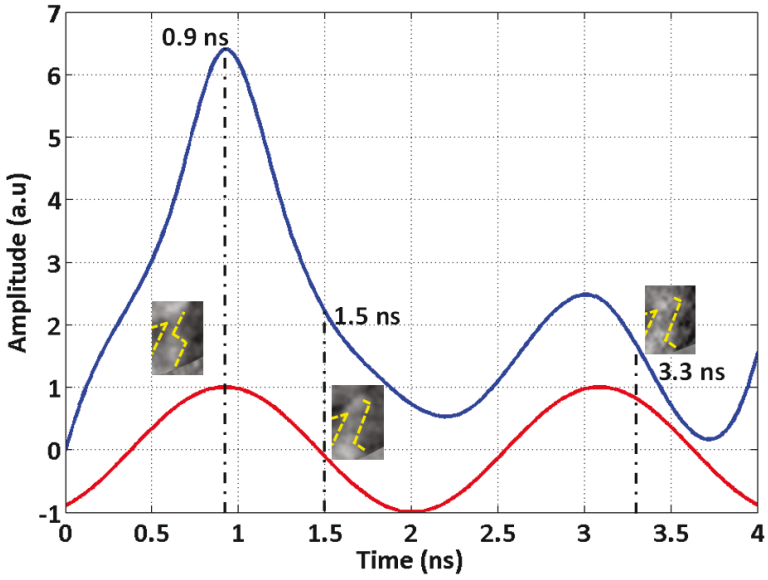

Figure 6.9: Plot of a sinusoidal function (red) simulating the oscillation of the domain wall with a frequency of 0.46 GHz. The time-scale was adjusted so that the first maximum is at 0.9 ns, the time of the strongest excitation in the experimental data. Insets: XMCD-images of the domain wall at three pump-probe delays. Blue curve: measured current pulse.

Chapter 7

Summary and Outlook

Summary

In this thesis, we studied the interaction of a spin-polarized current with domain walls (DWs) in NiFe nanostructures. The single-pulse and time-resolved experiments were performed by using the UE56/1 Juelich time-resolved XMCD-PEEM microscope at BESSY II Berlin, Germany.

In the single-pulse experiments, we observed that the current induced domain wall motion (CIDWM) in the $Ni_{20}Fe_{80}$ nanostructure needed a relatively high current density ($\sim 10^{12}$). It was concluded that the huge current density increased the temperature of the system above the Curie temperature of the material used. As a result, the spin configuration of the system completely changed or even the single domain structure split into multiple domains. Splitting of single domain into multiple domains via high current density was also observed by Yamaguchi et. al. [146]. The increase in temperature of the system reduced the STT effect. Our observation on the temperature increase due to the applied current density testified the theoretical reports of Chun-Yeol You et al. [149], Chun-Yeol You and Seung-Seok Ha [148] and Hans Fangohr et al. [33] and experimental findings of J. Yoon et al. [147].

We succeeded in performing the pump-probe experiments on $Ni_{80}Fe_{20}$ nanostructures. The short ($\sim$ 1.5 ns) current pulses were generated by a laser pulse

hitting an avalanche photo-diode. The laser pulses were synchronized to the BESSY bunch clock via a delay generator. The time resolved experiments were carried out by gating the imaging column to the camshaft bunch in the hybrid multi-bunch mode and also simply by synchronizing to the single-bunch in single-bunch mode (both at 1.25 MHz repetition frequency).

Specifically, we used half-ring shaped, notched half-ring-shaped or V-type nanostructures. The optimization of the sample layout makes it compatible with the PEEM and is a big achievement of this project. Different from other researchers [46, 68, 71, 72], we introduced the contacted pads to the nanostructure along with ground fields by following the definition of co-planar wave-guide.

Outlook

However, we optimized the procedure of sample preparation but we still have to pay the closer attention to the preparation procedure of the sample in the future. For this, we envision to improve the transparency of the contacted pads and ground fields from the residual resists around the nanostructure via introducing standardized etching techniques.

The present racetrack memory consists of a permalloy nanowire which is used to store digital data. It needs a high current density (10^{12} A/m^2) to move the domain walls via spin-transfer torque technique. The issue of using high current is that it generates higher Oersted field that affects the domain patterns, increasing the local heating and consuming a high power [44, 131]. Therefore, one needs to determine the lower current density for the domain wall motion. In this work, we reached a threshold current density of as low as to 7.5 $\times 10^{11}$ A/m^2. By further optimization of the material, its quality, the geometric layout and the lithographic techniques, the current density should be drastically reduced in order to ensure STT as the dominant process compared to temperature and Oersted field effects.

Though Permalloy single-layer nanowire is a useful system to study the STT mechanism for future applications, it is recommended to use other geometries, for example pillar geometry containing ferromagnetic/insulator/ferromagnetic layers. This geometry has rapidly attracted a tremendous interest of experimentalists, as it is not only favorable for the STT mechanism even at low current densities [24, 90] but also such geometry controls the current direction [19]. In addition, it can also be recommended to use other materials, like half-metallic materials, having higher spin polarization and lower saturation magnetization. Furthermore, recently a new writing method was suggested which could be based on spin transfer torque (STT) with spin reorientation, for low current writing perpendicular magnetic random memory with high thermal stability [123]. For this, stacks with Co/Ni and with Co/Pt multilayers were proposed.

As an alternative to the STT, recently a new torque mechanism, spin-orbit torque, has been recognized in structures such as heavy metal/ferromagnetic layer/insulating layer. This mechanism is based on angular momentum transfer from the crystal lattice to the magnetization via in-plane current injection, leading to a wide range of changes in a magnetic configuration. The spin-orbit torque based magnetic random access memory (SOT-MRAM) has drawn great attention as it eliminates some flaws of STT-MRAM. For example, since the current is injected in the plane of a layer rather than passing through the tunnel barrier, this technique does not damage the MTJ even by injecting high current density [19]. This torque could originate from the bulk of a heavy metal via spin Hall effect or from the interface of heavy metal and ferromagnetic layers by Rashba effect. So far, many efforts have been done by the spintronics community for the improvement of this mechanism. Recently, S. Woo et al. [143] demonstrated this mechanism in Pt/Co/Ta heterostructures and concluded that the interface between ferromagnet and heavy metals may improve spin transport by partial alloying [143]. C. K. Safeer et al. [111] successfully used Pt/Co/AlO_x trilayers system in which authors reported a generic approach to control magnetization reversal via SOT mechanism.

Concerning the pump probe setup, we developed the negative deflection

gating, which suppresses the signal of all "unpumped" bunches in the multi-bunch mode of the synchrotron and thus makes pump-probe studies possible during the whole year instead of 2 single bunch weeks. Different from the previously used positive gating deflection, here the usable electrons are by-passing the V-shaped front edge of the contrast aperture with almost no losses. This advantage was demonstrated but should be fully exploited in the future.

The amplitude of the available current pulse is presently limited up to 8 V. We have a solution to increase the pulse amplitude up to 18 V by introducing an avalanche transistor to the avalanche photo-diode. This will double the available current density and will keep the same time structure for the pump-probe experiments.

Bibliography

[1] http://micromagnetics.org/micromagnetism/. Accessed on 20.09.2017.

[2] Welcome to String Wizard, submitted by Paul Dooley, 21 March, 2013 Paul Dooley. http://www.wirestrungharp.com/material/strings/elastic_potential_energy.html. Accessed on 12.11.2017.

[3] Claas Willem Abert. *Discrete Mathematical Concepts in Micromagnetic Computations*. PhD thesis, University of Hamburg, 2013.

[4] D. Attwood. *Soft X-Rays and Extreme Ultraviolet Radiation: Principles and Applications*. Cambridge University Press, 2007.

[5] M. N. Baibich, J. M. Broto, A. Fert, F. Nguyen Van Dau, F. Petroff, P. Etienne, G. Creuzet, A. Friederich, and J. Chazelas. Giant magnetoresistance of (001)Fe/(001)Cr magnetic superlattices. *Phys. Rev. Lett.*, 61:2472, 1988.

[6] S. E. Barnes and S. Maekawa. Current-spin coupling for ferromagnetic domain walls in fine wires. *Phys. Rev. Lett.*, 95:107204, 2005.

[7] Ya. B. Bazaliy, B. A. Jones, and S. Zhang. Modification of the Landau-Lifshitz equation in the presence of a spin-polarized current in colossal- and giantmagnetoresistive materials. *Phys. Rev. B*, 57:R3213, 1998.

[8] Behtash Behin-Aein, Deepanjan Datta, Sayeef Salahuddin, and Supriyo Datta. Proposal for an all-spin logic device with built-in memory. *Nat. Nanotechnol.*, 5:266–270, 2010.

[9] L. Berger. Exchange interaction between ferromagnetic domain wall and electric current in very thin metallic films. *J. Appl. Phys.*, 55:1954, 1984.

[10] L. Berger. Emission of spin waves by a magnetic multilayer traversed by a current. *Phys. Rev. B*, 54(13):9353, 1996.

[11] G. Binasch, P. Grünberg, F. Saurenbach, and W. Zinn. Enhanced magnetoresistance in layered magnetic structures with antiferromagnetic interlayer exchange. *Phys. Rev. B*, 39:4828, 1989.

[12] Stephen Blundell. *Magnetism in Condensed Matter*. Oxford Master Series in Physics, 2001.

[13] E. Brüche and H. Johannson. Elektronenoptik und elektronenmikroskop. *Die Naturwissenschaften*, 20:353, 1932.

[14] M. T. Bryan, S. Bance, J. Dean, T. Schrefl, and D. A. Allwood. Transverse and vortex domain wall structure in magnetic nanowires with uniaxial in-plane anisotropy. *J. Phys. Condens. Matter*, 24:024205, 2011.

[15] D. Bürgler. *Magnetism and Spin-Polarized Transport*. Memristive Phenomena From Fundamental Physics to Neuromorphic Computing 47th IFF Spring School 2016 22 February 4 March 2016 in Jlich, Germany, 2016.

[16] K. H. J. Buschow. *Handbook of Magnetic Materials, Volume 17*. Elsevier, 2007.

[17] C. Chappert, A. Fert, and F. N. van Dau. The emergence of spin electronics in data storage. *Nat. Mater.*, 6:813, 2007.

[18] Jean-Yves Chauleau, Benjamin McMorran, Rachid Belkhou, Nicolas Bergeard, Tevfik Mentes, Miguel Nino, Andrea Locatelli, John Unguris, Stanislas Rohart, Jacques Miltat, and Andre Thiaville. Magnetization textures in NiPd nanostructures. *Phys. Rev. B*, 84:094416, 2011.

[19] Safeer Chenattukuzhiyil. *Study of domain wall dynamics in the presence of large spin-orbit coupling: chiral damping and magnetic origami*. PhD thesis, Universite Grenoble Alpes, 2015.

[20] X. M. Cheng and D. J. Keavney. Studies of nanomagnetism using synchrotron-based x-ray photoemission electron microscopy (x-peem). *Rep. Prog. Phys.*, 75:026501, 2012.

[21] A. Chernyshov, M. Overby, X. Liu, J. K. Furdyna, Y. Lyanda-Geller, and L. P. Rokhinson. Evidence for reversible control of magnetization in a ferromagnetic material via spin-orbit magnetic field. *Nat. Phys.*, 5:656, 2009.

[22] S. Y. Chou. Patterned magnetic nanostructures and quantized magnetic disks. *Proc. IEEE*, 85:652 – 671, 1997.

[23] E. I. Cooper, C. Bonhote, J. Heidmann, Y. Hsu, P. Kern, J. W. Lam, M. Ramasubramanian, N. Robertson, L. T. Romanki, and H. Xu. Recent developments in high-moment electroplated materials for recording heads. *IBM Journal of Research and Development*, 49:103 – 126, 2005.

[24] J. D. Costa, S. Serrano-Guisan, B. Lacoste, A. S. Jenkins, T. Boehnert, M. Tarequzzaman, J. Borme, F. L. Deepak, E. Paz, J. Ventura, R. Ferreira, and P. P. Freitas. High power and low critical current density spin transfer torque nano-oscillators using MgO barriers with intermediate thickness. *Sci. Rep.*, 7:7237, 2017.

[25] R. Cowburn. Data storage device and method. U.S. Patent No. WO/2007/132174.

[26] S. Cramm. *Synchrotron Radiation Sources and Beamlines: Overview*. Probing the Nanoworld, 38th IFF Spring School, Forschungszentrum Juelich, 2007.

[27] W. Demtröder. *Experimentalphysik 2-Elektrizität und Optik*. Springer Berlin, 1995.

[28] Philipp Eib. *Magnetic domain wall motion in the presence of defects: Experiments and simulations*. PhD thesis, ETH Zurich, 2015.

[29] A. Einstein. *Ann. Phys.*, 17:132, 1905.

[30] M. Eltschka, M. Wötzel, J. Rhensius, S. Krzyk, U. Nowak, M. Kläui, T. Kasama, R. E. Dunin-Borkowski, L. J. Heyderman, H. J. van Driel, and R. A. Duine. Nonadiabatic spin torque investigated using thermally activated magnetic domain wall dynamics. *Phys. Rev. Lett.*, 105:056601, 2010.

[31] D. J. Nagel et al. Proceedings of the international symposium on x-ray spectra and electronic structure of matter, Munich, edited by A. Saessler and G. Wiech. 2:51, 1972.

[32] Y. Fan, P. Upadhyaya, X. Kou, M. Lang, S. Takei, Z. Wang, J. Tang, L. He, L. T. Chang, M. Montazeri, G. Yu, W. Jiang, T. Nie, R. N. Schwartz, Y. Tserkovnyak, and K. L. Wang. Magnetization switching through giant spin-orbit torque in a magnetically doped topological insulator heterostructure. *Nat. Mater.*, 13:699–704, 2014.

[33] Hans Fangohr, Dmitri S. Chernyshenko, Matteo Franchin, Thomas Fischbacher, and Guido Meier. Joule heating in nanowires. *Phys. Rev. B*, 84:054437, 2011.

[34] Pietro Gambardella and Ioan Mihai Miron. Current-induced spin-orbit torques. *Phil. Trans. R. Soc. A*, 369:3175–3197, 2011.

[35] I. Garate, K. Gilmore, M. D. Stiles, and A. H. MacDonald. Nonadiabatic spin-transfer torque in real materials. *Phys. Rev. B*, 79:054428, 2006.

[36] Kevin Garello, Ioan Mihai Miron, Can Onur Avci, Frank Freimuth, Yuriy Mokrousov, Stefan Blügel, Stephane Auffret, Olivier Boulle, Gilles Gaudin, and Pietro Gambardella. Symmetry and magnitude of spinorbit torques in ferromagnetic heterostructures. *Nature Nanotechnology*, 8:587593, 2013.

[37] Theo Gerhardt. *Micromagnetic Simulations of Ferromagnetic Domain Walls in Nanowires*. PhD thesis, Universität Hamburg, 2014.

[38] T. L. Gilbert. A lagrangian formulation of the gyromagnetic equation of the magnetic field. *Phys. Rev.*, 100:1243, 1955.

[39] T. L. Gilbert. A phenomenological theory of damping in ferromagnetic materials. *IEEE Trans. Mag.*, 40:3443, 2004.

[40] SPECS GmbH. `http://www.specs.de/cms/upload/bilder/LEEM/SPECS-Brochure_LEEM.pdf`. Accessed on 20.11.2017.

[41] D. M. Gottlob. *Spin-reorientation transition in epitaxial Ni_xPd_{1-x} fims on Cu(001): a microscopic analysis*. PhD thesis, Duisburg-Essen University, 2015.

[42] Rachana Gupta, Mukul Gupta, and Thomas Gutberlet. Magnetization in permalloy thin films. *Pramana*, 71:11231127, 2008.

[43] Jun Hayakawa, Shoji Ikeda, Young Min Lee, Ryutaro Sasaki, Toshiyasu Meguro, Fumihiro Matsukura, Hiromasa Takahashi, and Hideo Ohno. Current-induced magnetization switching in mgo barrier based magnetic tunnel junctions with CoFeB/Ru/CoFeB synthetic ferrimagnetic free layer. *Jpn. J. Appl. Phys.*, 45:L1057L1060, 2006.

[44] J. Heinen, O. Boulle, K. Rousseau, G. Malinowski, M. Kläui, H. J. M. Swagten, B. Koopmans, C. Ulysse, and G. Faini. Current-induced domain wall motion in Co/Pt nanowires: Separating spin torque and Oersted-field effects. *Appl. Phys. Lett.*, 96(20):202510, 2010.

[45] R. Hertel. Thickness dependence of magnetization structures in thin permalloy rectangles. *Zeitschrift für Metallkunde*, 93:957–962, 2002.

[46] L. Heyne, J. Rhensius, A. Bisig, S. Krzyk, P. Punke, M. Kläui, L. J. Heyderman, L. Le Guyader, , and F. Nolting. Direct observation of high velocity current induced domain wall motion. *Appl. Phys. Lett.*, 96:032504, 2010.

[47] L. Heyne, J. Rhensius, D. Ilgaz, A. Bisig, U. Rüdiger, M. Kläui, L. Joly, F. Nolting, L. J. Heyderman, J. U. Thiele, , and F. Kronast. Direct determination of large spin-torque nonadiabaticity in vortex core dynamics. *PRL*, 105:187203, 2010.

[48] Lutz Heyne. *Manipulation of Magnetic Domain Walls and Vortices by Current Injection*. PhD thesis, Universität Konstanz, 2010.

[49] D. Hinzke and U. Nowak. Domain wall motion by the magnonic spin seebeck effect. *Phys. Rev. Lett.*, 107:027205, 2011.

[50] Atsufumi Hirohata and Koki Takanashi. Future perspectives for spintronic devices. *J. Phys. D: Appl. Phys.*, 47:193001, 2014.

[51] M. Hosomi, H. Yamagishi, T. Yamamoto, K. Bessho, Y. Higo, K. Yamane, H. Yamada, M. Shoji, H. Hachino, C. Fukumoto, H. Nagao, and H. Kan. Novel nonvolatile memory with spin torque transfer magnetization switching: spin-ram. *International Electron Devices Meeting (IEDM)*, page 459, 2005.

[52] Y. Huai, F. Albert, P. Nguyen, M. Pakala, and T. Valet. Observation of spin-transfer switching in deep submicron-sized and low-resistance magnetic tunnel junctions. *Appl. Phys. Lett.*, 84:31183120, 2004.

[53] A. Hubert and R. Schäfer. *Magnetic Domains-The Analysis of Magnetic Microstructures*. Berlin, New York, Heidelberg: Springer, 1998.

[54] S. Ikeda, J. Hayakawa, Y. Ashizawa, Y. M. Lee, K. Miura, H. Hasegawa, M. Tsunoda, F. Matsukura, and H. Ohno. Tunnel magnetoresistance of 604 % at 300 K by suppression of Ta diffusion in CoFeB/Mgo/CoFeB pseudo-spin-valves annealed at high temperature. *Appl. Phys. Lett.*, 93:082508, 2008.

[55] Muhammad Zahid Ishaque. *Effects of structural asymmetry on current-induced domain wall motion*. PhD thesis, Universit*é* de Grenoble, 2013.

[56] Keisuke Ito. String for musical instrument, EP0593762 A1, PCT/JP1991/000911. 1991.

[57] J. D. Jackson. *Classical Electrodynamics*. Wiley New York, 1962.

[58] Shikha Jain, Valentyn Novosad, Frank Y. Fradin, John E. Pearson, Vasil Tiberkevich, Andrei N. Slavin, and Samuel D. Bader. Control and manipulation of the dynamic response of interacting spin vortices. *IEEE Trans. Magn.*, 49(7):3081–3088, 2013.

[59] Mahdi Jamali, Kyung-Jin Lee, and Hyunsoo Yang. Effect of nonadiabatic spin transfer torque on domain wall resonance frequency and mass. *Appl. Phys. Lett.*, 98:092501, 2011.

[60] M. Julliere. Tunneling between ferromagnetic films. *Phys. Lett.*, 54A:225–226, 1975.

[61] Hyunsung Jung, Young-Sang Yu, Ki-Suk Lee, Mi-Young Im, Peter Fischer, Lars Bocklage, Andreas Vogel, Markus Bolte, Guido Meier, and Sang-Koog Kim. Observation of coupled vortex gyrations by 70 ps-time and 20 nm-space-resolved full-field magnetic transmission soft x-ray microscopy. *Appl. Phys. Lett.*, 97, 2010.

[62] A. M. Kaiser, C. Wiemann, S. Cramm, and C. M. Schneider. Influence of magnetocrystalline anisotropy on the magnetization dynamics of magnetic microstructures. *J.Phys.: Condens. Matter*, 21:314008, 2009.

[63] Alexander Kaiser. *Magnetization Dynamics in Magnetically Coupled Heterostructures*. PhD thesis, Duisburg-Essen University, 2009.

[64] Attila Kakay. *Numerical investigations of micromagnetic structures*. PhD thesis, Research Institute for Solid State Physics and Optics, Hungarian Academy of Sciences, 2005.

[65] R. Kikuchi. On the minimum of magnetization reversal time. *J. Appl. Phys.*, 27:13521357, 1956.

[66] Y. K. Kim and T. J. Silva. Magnetostriction characteristics of ultrathin permalloy films. *Appl. Phys. Lett.*, 68:2885, 1996.

[67] K. J. Kirk, J. N. Chapmanand, and C. D. W. Wilkinson. Lorentz microscopy of small magnetic structures (invited). *J. Appl. Phys.*, 85:5237, 1999.

[68] M. Kläui. Head-to-head domain walls in magnetic nanostructures (invited). *J. Phys.: Condens. Matter*, 20:313001, 2008.

[69] M. Kläui, H. Ehrke, U. Rüdiger, T. Kasama, R. E. Dunin-Borkowski, D. Backes, L. J. Heyderman, C. A. F. Vaz, J. A. C. Bland, G. Faini, E. Cambril, and W. Wernsdorfer. Direct observation of domain-wall pinning at nanoscale constrictions. *Appl. Phys. Lett.*, 87:102509, 2005.

[70] M. Kläui, M. Laufenberg, L. Heyne, D. Backesb, and U. Rüdiger. Current-induced vortex nucleation and annihilation in vortex domain walls. *Appl. Phys. Lett.*, 88:232507, 2006.

[71] M. Kläui, C. A. F. Vaz, J. Rothman, J. A. C. Bland, W. Wernsdorfer, G. Faini, and E. Cambril. Domain wall pinning in narrow ferromagnetic ring structures probed by magnetoresistance measurements. *Phys. Rev. Lett.*, 90:097202, 2003.

[72] M. Kläui, C. A. F. Vaz, W. Wernsdorfer, E. Bauer, S. Cherifi, S. Heun, A. Locatelli, G. Faini, E. Cambril, L. J. Heyderman, and J. A. C. Bland. Domain wall behaviour at constrictions in ferromagnetic ring structures. *Physica B*, 343:343–349, 2004.

[73] H. Kohno, G. Tatara, J. Shibata, and Y. Suzuki. Microscopic calculation of spin torques and forces. *J. Magn. Magn. Mater.*, 0:0, 2006.

[74] H. Kronmüller and R. Hertel. Computational micromagnetism of magnetic structures and magnetisation processes in small particles. *J. Magn. Magn. Mater.*, 12:215–216, 2000.

[75] M. Lakshmanan. The fascinating world of the landaulifshitzgilbert equation: an overview. *International Conference " Mixed Design of Integrated Circuits and Systems"*, 369:1280–1300, 2011.

[76] L. Landau and E. Lifshitz. On the theory of dispersion of magnetic permeability in ferromagnetic bodies. *Phys. Z. Sowjet.*, 8:153, 1935.

[77] Jeffrey Lang. *Multi-Wafer Rotating MEMS Machines: Turbines, Generators, and Engines*. Springer Science and Business Media, 2009.

[78] Markus Laufenberg. *Interactions Between Current and Domain Wall Spin Structures*. PhD thesis, Universität Konstanz, 2006.

[79] M. A. Laughton and D.F. Warne. *Electrical Engineer's Reference Book: Edition 164*. Newnes, 2002.

[80] Serban Lepadatu. Interaction of magnetization and heat dynamics for pulsed domain wall movement with joule heating. *J. Appl. Phys.*, 120:163908, 2016.

[81] Z. Li and S. Zhang. Domain-wall dynamics and spin-wave excitations with spintransfer torques. *Phys. Rev. Lett.*, 92:207203, 2004.

[82] Z. Li and S. Zhang. Domain-wall dynamics driven by adiabatic spintransfer torques. *Phys. Rev. B*, 70:024417, 2004.

[83] T. Liu, D. Lacour, F. Montaigne, S. Le Galla, M. Hehn, and T. Hauet. Extraordinary hall effect based magnetic logic applications. *Appl. Phys. Lett.*, 106:052406, 2015.

[84] A. Locatelli and E. Bauer. Recent advances in chemical and magnetic imaging of surfaces and interfaces by xpeem. *J. Phys. Condens. Matter*, 20, 2008.

[85] N. Locatelli, V. Cros, and J. Grollier. Spin-torque building blocks. *Nat. Mater.*, 13, 2014.

[86] Hiwa Mahmoudi, Thomas Windbacher, Viktor Sverdlov, and Siegfried Selberherr. Design and applications of magnetic tunnel junction based logic circuits. *Proceedings of the 2013 9th Conference on Ph.D. Research in Microelectronics and Electronics (PRIME)*, 24-27 June 2013.

[87] Yann Le Maho, Joo-Von Kim, and Gen Tatara. Spin-wave contributions to current-induced domain wall dynamics. *Phy. Rev. B*, 97, 2009.

[88] J. Mallinson. On damped gyromagnetic precession. *IEEE Trans. Magn.*, 23:2003, 1987.

[89] K. L. McNerny, Y. Kim, D. E. Laughlin, and M. E. McHenry. Chemical synthesis of monodisperse γ-FeNi magnetic nanoparticles with tunable Curie temperatures for self-regulated hyperthermia. *J. Appl. Phys.*, 107:09A312, 2010.

[90] H. Meng, R. Sbiaa, S. Y. H. Lua, C. C. Wang, M. A. K. Akhtar, S. K. Wong, P. Luo, C. J. P. Carlberg, and K. S. A. Ang. Low current density induced spin transfer torque switching in CoFeB-MgO magnetic tunnel junctions with perpindicular anisotropy. *J. Phys. D: Appl. Phys.*, 44:405001, 2011.

[91] S. Mobilio, F. Boscherini, and C. Meneghini. *Synchrotron Radiation: Basics, Methods and Applications*. Springer-Verlag Berlin Heidelberg, 2015.

[92] J. S. Moodera and R. H. Meservey. Spin-polarized tunnelling magnetoelectronics. *ed M Johnson (Amsterdam: Elsevier)*, page 163, 2004.

[93] Bruce M. Moskowitz. Hitchhiker's Guide to Magnetism. `http://www.irm.umn.edu/hg2m/hg2m_b/hg2m_b.html`. Accessed on 12.09.2017.

[94] D. Neeb, A. Krasyuk, A. Oelsner, S. A. Nepijko, H. J. Elmers, A. Kuksov, C. M. Schneider, and G. Schönhense. Sub-nanosecond resolution x-ray magnetic circular dichroism photoemission electron microscopy of magnetization processes in a permalloy ring. *J. Phys.: Matter*, 17:1381, 2005.

[95] Duc-The Ngo and N. H. Duc. *Advanced Magnetism and Magnetic Materilas - Volume 2: Aspects of magneto-electrostrictive materials and applications, Chapter: 3*. Vietnam National University Press, 2015.

[96] F. Nickel, D. M. Gottlob, I. P. Krug, H. Doganay, S. Cramm, A. M. Kaiser, G. Lin, D. Makarov, O. G. Schmidt, and C. M. Schneider. Time-resolved magnetic imaging in an aberration-corrected, energy-filtered photoemission electron microscope. *Ultramicroscopy*, 54:130, 2013.

[97] Florian Nickel. *Aberrationskorrigierte Photoemissionsmikroskopie an magnetischen Systemen: Von statischer Charakterisierung zu zeitaufgeloester Abbildung*. PhD thesis, Duisburg-Essen University, 2013.

[98] Fabian Oboril, Rajendra Bishnoi, Mojtaba Ebrahimi, and Mehdi B. Tahoori. Evaluation of Hybrid Memory Technologies using SOT-MRAM for On-Chip Cache Hierarchy. *IEEE Transactions on Computer-Aided Design of Integrated Circuits and Systems*, 34:367–380, 2015.

[99] T. Ono, H. Miyajima, K. Shigeto, K. Mibu, N. Hosoito, and T. Shinjo. Propagation of a magnetic domain wall in a submicrometer magnetic wire. *Science*, 284:468, 1999.

[100] S. S. P. Parkin. Spintronic materials and devices: Past, present and future. *Electron Devices Meeting, 2004. IEDM Technical Digest. IEEE International*, 2004.

[101] S.S.P. Parkin. Shiftable magnetic shift register and method of using the same. *United States Patent No.6*, 834:005B1, December 21, 2004.

[102] M. Pekala, D.Oleszak, E. Jartych, and J. K. Zurawicz. Structural and magnetic study of crystalline $Fe_{80}Ni_{20}$ alloys with nanometer-sized grains. *J. Non-Cryst. Solids*, 250-252:757–761, 1999.

[103] D. Ralph and R. Buhrman. *Concepts in Spin Electronics, S. Maekawa (Ed.)*. Oxford Univ. Press, 2006.

[104] W. Rave and A. Hubert. Magnetic ground state of a thin-film element. *IEEE Trans. Magn.*, 36:3886, 2000.

[105] D. Ravelosona, D. Lacour, J. A. Katine, B. D. Terris, and C. Chappert. Nanometer scale observation of high effciency thermally assisted current-driven domain wall depinning. *Phys. Rev. Lett.*, 95:117203, 2005.

[106] Rees D. Rawlings. *Materials Science and Engineering-Volume II*. EOLSS Publications, 2009.

[107] J. Rhensius, L. Heyne, D. Backes, S. Krzyk, L. J. Heyderman, L. Joly, F. Nolting, and M. Kläui. Imaging of domain wall inertia in permalloy half-ring nanowires by time-resolved photoemission electron microscopy. *Phys. Rev. Lett.*, 104:067201, 2010.

[108] W. C. Röntgen. On a new kind of ray. *Nature*, 53:274, 1896.

[109] Margaret Rouse. MRAM (magnetoresistive random access memory by Margaret Rouse. `http://searchstorage.techtarget.com/definition/{MRAM}`. Accessed on 20.09.2017.

[110] M. Sacchi and J. Vogel. *Dichroism in X-ray Absorption in Magnetism and Synchrotron Radiation*. Springer, 2001.

[111] C. K. Safeer, Emilie Jue, Alexandre Lopez, Liliana Buda-Prejbeanu, Stephane Auffret, Stefania Pizzini, Olivier Boulle, Ioan Mihai Miron, and Gilles Gaudin. Spinorbit torque magnetization switching controlled by geometry. *Nat. Nanotechnol.*, 11:143146, 2016.

[112] Eiji Saitoh, Hideki Miyajima, Takehiro Yamaoka, and Gen Tatara. Current-induced resonance and mass determination of a single magnetic domain wall. *Nature*, 432:203, 2004.

[113] Shigemi Sasaki, Kazunori Kakuno, Takeo Takada, Taihei Shimada, Ken ichi Yanagida, and Yoshikazu Miyahara. Design of a new type of planar undulator for generating variably polarized radiation. *Nucl. Instr. Meth. Phys. Res. A: Accelerators, Spectrometers, Detectors and Associated Equipment*, 331:763, 1993.

[114] Klaus D. Sattler. *Handbook of Nanophysics: Nanoparticles and Quantum Dots*. CRC Press, 19.04.2016.

[115] C. Schmitz-Antoniak. X-ray absorption spectroscopy on magnetic nanoscale systems for modern applications. *Rep. Prog. Phys*, 78:062501, 2015.

[116] C. Schneider and J. Kirschner. *Handbook of Surface Science, Chapter 9 magnetism at surfaces and in ultrathin films, in Electronic Structure, edited by K. Horn and M. Scheffler*. North-Holland, 2000.

[117] C. M. Schneider, , A. Kuksov, A. Krasyuk, A. Oelsner, D. Neeb, S. A. Nepijko, G. Schönhense, I. Mönch, R. Kaltofen, J. Morais, C. de Nadaï, and N. B. Brookes. Incoherent magnetization rotation observed in subnanosecond time-resolving x-ray photoemission electron microscopy. *Appl. Phys. Lett.*, 85:2562, 2004.

[118] C. M. Schneider and Schönhense. Investigating surface magnetism by means of photoexcitation electron emission microscopy. *Rep. Progr. Phys.*, 65:1785, 2002.

[119] G. Schütz, W. Wagner, W. Wilhelm, P. Kienle, R. Zeller, R. Frahm, and G. Materlik. Absorption of circularly polarized x-rays in iron. *Phys. Rev. Lett.*, 58:737, 1987.

[120] D.J. Sellmyer and Ralph Skomski. *Advanced Magnetic Nanostructures*. Springer Science and Business Media, 2006.

[121] A. A. Serga, A. V. Chumak, and B. Hillebrands. YIG magnonics. *J. Phys. D: Appl. Phys.*, 43:264002, 2010.

[122] J. C. Slonczewski. Current-driven excitation of magnetic multilayers. *J. Magn. Magn. Mater.*, Volume 159(Issues 1-2):L1–L7, 1996.

[123] Min Song, Yan Xu, Jun OuYang, Yue Zhang, Dongsheng Liu, Xiaofei Yang, Xuecheng Zou, and Long You. Low current writing perpendicular magnetic random access memory with high thermal stability. *Mater. Des.*, 92:1046, 2016.

[124] Falk-Ulrich Stein, Lars Bocklage, Markus Weigand, and Guido Meier. Time-resolved imaging of nonlinear magnetic domain-wall dynamics in ferromagnetic nanowires. *Sci. Rep.*, 3:1737, 2013.

[125] J. Stöhr, Y. Wu, B. D. Hermsmeier, M. G. Samant, G. R. Harp, S. Koranda, D. Dunham, and B. P. Tonner. Element-specific magnetic microscopy with circularly polarized x-rays. *Science*, 259:658, 1993.

[126] Li Su, Youguang Zhang, Jacques-Olivier Klein, Yue Zhang, Arnaud Bournel, Albert Fert, and Weisheng Zhao. Current-limiting challenges for all-spin logic devices. *Sci. Rep.*, 5:14905, 2015.

[127] Viktor Sverdlov, Hiwa Mahmoudi, Alexander Makarov, and Siegfried Selberherr. Magnetic tunnel junction for future memory and logic-in-memory applications. *International Conference " Mixed Design of Integrated Circuits and Systems"*, 19-21 June 2014, Poland.

[128] T. Taniguchi, J. Sato, and H. Imamura. Theory of spin accumulation and spin-transfer torque in a magnetic domain wall. *Phys. Rev. B*, 79:212410, 2009.

[129] A. Thiaville, Y. Nakatani, J. Miltat, and Y. Suzuki. Micromagnetic understanding of current driven domain wall motion in patterned nanowires. *EPL*, 69:990, 2005.

[130] B.T. Thole, G. van der Laan, and G.A. Swatazky. Strong magnetic dichroism predicted in the $M_{4,5}$ x-ray absorption spectra of magnetic rare-earth materials. *Phys. Rev. Lett.*, 55:2086, 1985.

[131] Luc Thomas, Rai Moriya, Charles Rettner, and Stuart S.P. Parkin. Dynamics of magnetic domain walls under their own inertia. *Science*, 330:1810–1813, 2010.

[132] B. P. Tonner and G. R. Harp. Photoelectron microscopy with synchrotron radiation. *Rev. Sc. Instr.*, 59:853, 1988.

[133] Jacob Torrejon, Eduardo Martinez, and Masamitsu Hayash. Tunable inertia of chiral magnetic domain walls. *Nat. Commun.*, 7:13533, 2016.

[134] R. M. Tromp, Y. Fujikawa, J. B. Hannon, A. W. Ellis, A. Berghaus, and O. Schaff. A simple energy filter for low energy electron mi-

croscopy/photoelectron emission microscopy instruments. *J. Phys. Condens. Matter*, 21:314007, 2009.

[135] R. M. Tromp, J. B. Hannon, W. Wan, and O. Schaff. A new aberration-corrected, energy-filtered leem/peem instrument II. operation and results. *Ultramicroscopy*, 127:25–39, 2013.

[136] R. M. Tromp, W. Wan, and S. M. Schramm. Aberrations of the cathode objective lens up to fifth order. *Ultramicroscopy*, 119:33–39, 2012.

[137] M. Tsoi, R. E. Fontana, and S. S. P. Parkin. Magnetic domain wall motion triggered by an electric current. *Appl. Phys. Lett.*, 83:2617, 2003.

[138] Vojtěch Uhlič. *Current-Induced Magnetization Dynamics in Nanostructures*. PhD thesis, Joseph-Fourier University, Grenoble, 2010.

[139] Vojtech Uhlir, Stefania Pizzini, Nicolas Rougemaille, Vincent Cros, Erika Jimenez, Laurent Ranno, Olivier Fruchart, Michal Urbanek, Gilles Gaudin, Julio Camarero, Carsten Tieg, Fausto Sirotti, Edouard Wagner, and Jan Vogel. Direct observation of Oersted-field-induced magnetization dynamics in magnetic nanostripes. *Phys. Rev. B*, 83:020406, 2011.

[140] A. Vanhaverbeke and M. Viret. Simple model of current-induced spin torque in domain walls. *Phys. Rev. B*, 75:024411, 2007.

[141] K. L. Wang, J. G. Alzate, and P. Khalili Amiri. Low-power non-volatile spintronic memory: STT-RAM and beyond. *J. Phys. D: Appl. Phys.*, 46:7, 2013.

[142] Dan Wei. *Micromagnetics and Recording Materials*. Springer Science and Business Media, 2012.

[143] S. Woo, M. Mann, A. J. Tan, L. Caretta, and G. S. D. Beach. Enhanced spin-orbit torques in Pt/Co/Ta heterostructures. *Appl. Phys. Lett.*, 105:212404, 2014.

[144] Seonghoon Woo. *Manipulation of Spin Textures by Unconventional Spin Torques*. PhD thesis, Massachusetts Institute of Technology, 2015.

[145] J. Xiao, A. Zangwill, and M. D. Stiles. Spin-transfer torque for continuously variable magnetization. *Phys. Rev. B*, 73:104416, 2009.

[146] A. Yamaguchi, S. Nasu, H. Tanigawa, T. Ono, K. Miyake, Ko Mibu, and T. Shinjo. Effect of joule heating in current-driven domain wall motion. *Appl. Phys. Lett.*, 1:012511, 2005.

[147] Jungbum Yoon, Jae-Chul Lee, Chun-Yeol You, Sug-Bong Choe, Kyung-Ho Shin, and Myung-Hwa Jung. Current- and field-driven domain wall motion in L-and C-shaped permalloy nanowires with different wire widths. *IEEE Trans. Magn.*, 44:2527, 2008.

[148] Chun-Yeol You and Seung-Seok Ha. Temperature increment in a current-heated nanowire for current-induced domain wall motion with finite thickness insulator layer. *Appl. Phys. Lett.*, 91:022507, 2007.

[149] Chun-Yeol You, In Mo Sung, and Byung-Kyu Joe. Analytic expression for the temperature of the current-heated nanowire for the current-induced domain wall motion. *Appl. Phys. Lett.*, 89:222513, 2006.

[150] Z. Yuan, S. Wang, and K. Xia. Thermal spin-transfer torques on magnetic domain walls. *Solid State Commun.*, 150:548–551, 2010.

[151] S. Zhang and Z. Li. Roles of nonequilibrium conduction electrons on the magnetization dynamics of ferromagnets. *Phys. Rev. Lett.*, 93:127204, 2004.

[152] M. Zhu, C. L. Dennis, and R. D. McMichael. Temperature dependence of magneti- zation drift velocity and current polarization in Py by spin-wave doppler measurements. *Phys.Rev. B*, 81:140407, 2010.

Acknowledgments

In the beginning, I would like to express my thanks to all those people who have involved in this Ph.D. project to make it successful.

I am deeply thankful first and for most to my supervisor **Prof. Dr. Claus M. Schneider** for giving me an opportunity to work in his institute. This thesis would not be possible without his guidance and continuous support.

I would like to thank **Prof. Dr. Carsten Westphal** for accepting the task of second referee for this thesis.

I am grateful to **Dr. Stefan Cramm**, for discussions, inspiration and continuous support by personal appearance during beamtimes. I am especially indebted to him for his careful readings of many drafts of this thesis.

My gratitude and thanks go to my fellow Ph.D. student **Johanna Hackl** for helping me during the beamtime. Special gratitude goes to my ex. Ph.D. senior fellows **Hatice Doganay** and **Dr. Daniel Gottlob** for sharing their experience of operating and understanding the complexity of the microscope.

A special thanks go to **Dr. Slavomir Nemsak** for countless help, guidance, and support throughout this project.

I am thankful to **Dr. Daniel Bürgler** for giving me right suggestion at right time for reaching my destination. He is such a nice person that whenever I visit his office for discussion, he met so kindly and politely.

Another gratitude goes to **Dr. Roman Adam**. I appreciate his sincere guidance to achieve this goal.

The help of **Dr. Stefan Trellenkamp** (PGI-8, FZJ) with e-beam writing for nanostructures, **Rene Borowski** (PGI-7, FZJ) for doing ion-beam etching on the samples, and **Mona Nonn** (PGI-8, FZJ) for preparing a glass mask is greatly acknowledged. I am grateful to the whole staff of PGI-7 cleanroom for their help.

Many thanks go to **Thomas Jansen** for doing the material deposition on the samples. It was a pleasure working with you.

Umut Parlak. Apart from helping with the evaporation of Permalloy material on the sample, you have become a friend. I will always remember your politeness and kindness.

This project could not be possible without the electronic support of **Heinz Pfeiffer**. He has done a great job by constructing the home-made pulse generator for the single pulse experiments and negative gating setup for pump-probe measurements. The support of **Jürgen Lauer** and **Norbert Schnitzler** for improving the beamline software is highly appreciated.

I am grateful to the staff of **HZB** and **BESSY II** for providing user-support with electronics, UHV support throughout this project.

I am also thankful to all staff, Ph.D. students at the **Peter-Grünberg-Institut 6, Forschungszentrum Jülich** for their nice chat and friendly responses at different occasions.

At the end, I would like to express my deepest thanks to my parents for their spiritual and financial support throughout my life. I am much grateful to my wife, **Zanjabeela Khattak** and kids **Manno Salwa Khattak**, **Ansharah Khattak** and **Fayakun Khattak** for their patience and continuous support.

List of Own Publications

J. Schaab, I. P. Krug, H. Doğanay, J. Hackl, D. M. Gottlob, **M. I. Khan**, S. Nemšak, L. Maurel, E. Langenberg, P. A. Algarabel, J. A. Pardo, C. M. Schneider, and D. Meier,
Contact-Free Mapping of Electronic Transport Phenomena of Polar Domains in $SrMnO_3$ Films, Physical Review Applied **5**, 054009 (2016)

Christoph Baeumer, Christoph Schmitz, Astrid Marchewka, David N. Mueller, Richard Valenta, Johanna Hackl, Nicolas Raab, Steven P. Rogers, **M. Imtiaz Khan**, Slavomír Nemšák, Moonsub Shim, Stephan Menzel, Claus Michael Schneider, Rainer Waser and Regina Dittmann,
Quantifying redox-induced Schottky barrier variations in memristive devices via in operando spectromicroscopy with graphene electrodes, Nature Communications **7**, 12398 (2016)
DOI:10.1038/ncomms12398

Johanna Hackl, Tomáš Duchoň, David N. Mueller, Jolla Kullgren, Dou Du, Caroline Mouls, Daniel M. Gottlob, **Muhammad I. Khan**, Stefan Cramm, Kateřina Veltruská, Vladimir Matolin, Slavomir Nemšák, Claus M. Schneider,
Reduction properties of model ceria (111) and (100) nanoislands, submitted to Nature Materials

Conference contributions

J. Hackl, **M. I. Khan**, H. Doğanay, D. Gottlob, F. Nickel, I. Krug, A. Kaiser, S. Nemšák, and C. M. Schneider, *Time-Resolved Magnetic Imaging in an Energy-*

Filtered, Aberration-Corrected Photoemission Electron Microscope, FEMTOMAG: Magnetism from Fundamentals to Ultrafast Nanoscale Dynamics, Radboud Summer School course, Radboud University, Nijmegen, the Netherlands, 15 August 2014

Khan M. I., Hackl J., Nemšák S., Parlak U., Doğanay H., Gottlob G., Cramm S., Bürgler D., Schneider C. M., *Magnetization Dynamics in Ferromagnetic Layers Produced by Spin-polarized Current*, BESSY User Meeting, Berlin, Germany, 9.-10. December 2015

Schaab J., Hackl J., **Khan I.**, Doğanay H., Gottlob D., Nemšák S., Krug I. P., Schneider C. M., and Meier D., *Investigating electronic transport properties of ferroelectric domains and domain walls by LEEM and X-PEEM*, BESSY User Meeting, Berlin, Germany, 9.-10. December 2015

Mueller D. N., Hackl J., **Khan M. I.**, Nemšák S., Machala M. L., Bluhm H., Chueh W. C., Schneider C. M., *Surface defect chemistry of lanthanum ferrite perovskites*, BESSY User Meeting, Berlin, Germany, 9.-10. December 2015

Baeumer, C. ; Schmitz, C. ; Marchewka, A. ; Mueller, D. ; Valenta, R. ; Hackl, J. ; Raab, N. ; Rogers, S. P. ; **Khan, M. I.** ; Nemsak, S. ; Shim, M. ; Menzel, S. ; Schneider, C. M. ; Waser, R. ; Dittmann, R. *Photoelectron-transparent graphene top electrodes for in-operando spectromicroscopic characterization of memristive devices*, European Materials Research Meeting, Lille, France, 2 May 2016 - 6 May 2016

J. Hackl, T. Duchon, D.M. Gottlob, C. Mouls, **I. Khan**, S. Cramm, S. Nemsak and C.M. Schneider, *On the reduction behavior of CeO_2 (100) and (111) surfaces*, LEEMPEEM 10, Monterey, California, 11. September - 15. September 2016

C. Mouls, J. Hackl, H. Doganay, **I. Khan**, S. Cramm, J. C. Cezar, S. Nemsak, C.M. Schneider, *Study of magnetoelectric coupling of a thin layer of Fe deposited on a $BaTiO_3$ single crystal surface* , LEEMPEEM 10, Monterey, California, 11. September - 15. September 2016

Khan M. I., Cramm S., Nemšák S., Parlak U., Hackl J., Doğanay H., Gottlob G., Bürgler D., Schneider C. M., *Spin-polarized Current Induced Changes in* $Ni_{80}Fe_{20}$ *Half Ring Nanostructures*, BESSY User Meeting, Berlin, Germany, 7.-9. December 2016

Hackl, Duchon, Mueller, Mouls, Gottlob, **Khan**, Cramm, Nemšák, Schneider, *On the reduction behavior of* CeO_2*(100) and (111) surfaces*, BESSY User Meeting, Berlin, Germany, 7.-9. December 2016

Mouls C., Hackl J., Doğanay H., **Khan I.**, Cramm S., Cezar J. C., Nemšák S., Schneider C. M., *Study of magnetoelectric coupling of a thin layer of Fe deposited on a* $BaTiO_3$ *single crystal surface*, BESSY User Meeting, Berlin, Germany, 7.-9. December 2016

Band / Volume 154
Gate-All-Around Silicon Nanowire Tunnel FETs for Low Power Applications
G. V. Luong (2017), ii, 136 pp
ISBN: 978-3-95806-259-7

Band / Volume 155
Graphene Devices for Extracellular Measurements
D. Kireev (2017), ix, 169 pp
ISBN: 978-3-95806-265-8

Band / Volume 156
Nanoscale 3D structures towards improved cell-chip coupling on microelectrode arrays
S. D. Weidlich (2017), II, 154 pp
ISBN: 978-3-95806-278-8

Band / Volume 157
Interface phenomena in $La_{1/3}Sr_{2/3}FeO_3$ / $La_{2/3}Sr_{1/3}MnO_3$ heterostructures and a quest for p-electron magnetism
M. Waschk (2017), ix, 205 pp
ISBN: 978-3-95806-281-8

Band / Volume 158
Physics of Life
Lecture Notes of the 49th IFF Spring School 2018
26 February – 09 March 2018, Jülich, Germany
ed. by G. Gompper, J. Dhont, J. Elgeti, C. Fahlke, D. Fedosov, S. Förster, P. Lettinga, A. Offenhäusser (2018), ca 1000 pp
ISBN: 978-3-95806-286-3

Band / Volume 159
Identifizierung von Bindungsdeterminanten von Tat-Vorläuferproteinen an den TatBCRezeptorkomplex während der Tat-abhängigen Proteintranslokation in *Escherichia coli*
A. Ulfig (2018), 186 pp
ISBN: 978-3-95806-290-0

Band / Volume 160
***Corynebacterium glutamicum* – a novel platform for the production of plant polyphenols**
N. Kallscheuer (2018), X, 98 pp
ISBN: 978-3-95806-291-7

Band / Volume 161
Neurons on 3D polymer nanostructures
A. Belu (2018), vii, 135 pp
ISBN: 978-3-95806-296-2

Band / Volume 162
Tailoring and Characterisation of Bioelectronic Interfaces
A. Markov (2018), 75 pp
ISBN: 978-3-95806-298-6

Band / Volume 163
Epitaxy of group IV Si-Ge-Sn alloys for advanced heterostructure light emitters
N. von den Driesch (2018), viii, 149 pp
ISBN: 978-3-95806-300-6

Band / Volume 164
Impact and Regulatory Control of the CGP3 Prophage in *Corynebacterium glutamicum*
E. Pfeifer (2018), IV, 206 pp
ISBN: 978-3-95806-301-3

Band / Volume 165
Establishment of Bacterial Microcompartments in the Industrial Production Strain *Corynebacterium glutamicum*
I. Huber (2018), X, 114, XI-XXXIV pp
ISBN: 978-3-95806-302-0

Band / Volume 166
Current-Induced Magnetization Dynamics in Ferromagnetic Nanowires
M. I. Khan (2018), vi, 138 pp
ISBN: 978-3-95806-308-2

Weitere ***Schriften des Verlags im Forschungszentrum Jülich*** unter
http://wwwzb1.fz-juelich.de/verlagextern1/index.asp

Schlüsseltechnologien / Key Technologies
Band / Volume 166
ISBN 978-3-95806-308-2

Mitglied der Helmholtz-Gemeinschaft

JÜLICH
Forschungszentrum